Development of Coupled Thermal-Hydraulic-Mechanical-Chemical Models for Predicting Rock Permeability Change

2019

SHO OGATA

Abstract

When considering the long-term performance of geological disposal systems of high-level radioactive waste, it is essential to predict the long-term evolution of the hydraulic property of the rock surrounding the radioactive waste under coupled Thermal-Hydraulic-Mechanical-Chemical (THMC) conditions. In the prediction of the long-term evolution of the hydraulic property of the target rock, the mineral reactions within the rock comprise the most important issue. The objective of this thesis is to develop coupled THMC numerical models that can accurately predict the long-term changes in rock permeability due to mineral reactions such as pressure dissolution. Additionally, by utilizing the developed models, predictions are made of the long-term evolution of the permeability of the rock near high-level radioactive waste within a geological disposal system.

Firstly, a new coupled THMC numerical model is developed that incorporates the pressure dissolution at the grain contacts for estimating the changes in permeability within the matrix of porous rock, and the validity of the model is confirmed by replicating the experimental measurements obtained from quartz-sand compaction experiments. Then, the verified model is applied to predict the long-term evolution of the permeability in porous rock under the expected stress and temperature conditions where high-level radioactive waste is disposed. The predictions confirm that the process of pressure dissolution decreases the rock permeability, especially close to the excavated cavity, to one order of magnitude smaller than the initial value.

Secondly, a coupled THMC numerical model is proposed that includes the pressure dissolution at the contacting asperities of rock fractures for predicting the changes in permeability of the rock fractures, and the validity of the proposed model is examined by simulating the experimental measurements obtained from flow-through experiments using granite and mudstone samples with single fractures. The model predictions are found to be capable of following the experimental data for the evolution of the hydraulic aperture and the effluent solute concentrations without adopting any fitting parameters, which is often a necessary step in other simulations using coupled THMC models. Thus, the simulation results indicate that the proposed model should be valid for predicting the evolution of the fluid flow and the mass transport behavior within rock fractures due to the geochemical effect.

Subsequently, by upgrading the two previously proposed models, a new coupled THMC numerical model is developed by accounting for the pressure dissolution occurring at both the grain contacts and the fracture contacts. The model enables the determination of the changes in permeability within both the rock matrix and the rock fractures. Long-term predictions of the permeability in the fractured rock near high-level radioactive waste are made with the developed model, and the effects of the pressure dissolution within the rock matrix and the rock fractures are examined separately. The predicted results show that the rock permeability of the Excavation Damaged Zone (EDZ) eventually decreases to that of the intact rock after disposing the radioactive waste due to pressure dissolution within the rock fractures. Thus, the pressure dissolution within rock fractures should have a critical influence on the permeability evolution in the fractured media of the EDZ.

Finally, a coupled THMC numerical model, including the fracture initiation/propagation process, is newly developed by incorporating the damage theory and the mineral dissolution/precipitation process (i.e., pressure dissolution and free-face dissolution/precipitation) within the generated fractures. The model is applied to long-term coupled THMC simulations, including an excavation analysis for a disposal cavity. The predictions confirm that, during the excavation, several fractures are generated near the disposal cavity and the permeability increases in the damaged zone, and that, after the excavation, the permeability of almost the entire damaged zone decreases to that of the intact rock zone due to pressure dissolution at the contacting asperities within the fractures. Overall, these results should provide confidence for using the developed model to

evaluate the long-term performance of rock near radioactive waste contained within geological repositories for delaying the transport of radioactive nuclides.

Acknowledgements

The work of this dissertation could not have been achieved without the great support and assistance from advisors, friends, and family. I would like to extend my sincere gratitude to them.

First and foremost, I would like to express my profound gratitude and appreciation to my supervisor, Professor Kiyoshi Kishida, for the warmhearted and enthusiastic advice he gave me throughout my studies. His suggestions, based on his deep insight and vast knowledge, greatly assisted me in making this work successful. Furthermore, he always talked with me in a friendly manner; this made my university life so joyful. I am very grateful to Professor Kishida for giving me an opportunity to study in his laboratory and I am very proud to have been a member of his team.

I would next like to express my great appreciation to the members of the dissertation committee, Professor Makoto Kimura and Professor Katsuaki Koike, for their invaluable comments and suggestions as well as for the time and effort they spent in reviewing my dissertation.

I would also like to express my special respect and gratitude to Professor Hideaki Yasuhara of Ehime University. He was my original supervisor and I thank him for his continuous support and constructive guidance throughout my studies. His insightful and precise advice, based on his erudite knowledge and considerable creativity in research, gave me significant ideas that helped me succeed in my studies. I have always been impressed by his noble character and his great enthusiasm toward scientific research. I am proud to have studied under his supervision.

I am also deeply indebted to Associate Professor Naoki Kinoshita of Ehime University, who was also one of my original supervisors. His suggestions, based on his deep knowledge and experiences with experimental research, gave me significant insight into rock mechanics. Furthermore, I have been encouraged by his warm words of kindness. I could not have completed my studies without his support. I am proud to have studied under his supervision.

I would next like to express my appreciation to Associate Professor Yasuo Sawamura. He gave me a lot of precious advice and kind attention. Thanks to his support, I was able to push forward with my research and enjoy my university life.

I would like to offer my gratitude to Professor Tadashi Yamada. He has cared for and encouraged me continuously. His support helped to enhance my studies.

I also wish to express my appreciation to Associate Professor Shinichiro Nakashima of Yamaguchi University, Associate Professor Mamoru Kikumoto of Yokohama National University, Assistant Professor Ryota Hashimoto of Hiroshima University, and Dr. Michihito Shimo of Fukada Geological Institute. They all offered me great advice and support. The discussions we had during the progress of my studies were immensely helpful to me.

I gratefully acknowledge the support of Dr. Masanori Hashiguchi of Keisoku Engineering System for assisting me in performing the numerical analyses with the commercial multi-physics simulation software COMCOL MULTIPHYSICS for this dissertation.

I would next like to offer my gratitude to Mr. Gen Hayashi, a doctoral student, and Assistant Professors Yusuke Miyazaki and Ryunosuke Kido. As my seniors, they taught me the fundamental

attitude of a doctoral student and gave me invaluable advice whenever I was worried about various issues.

I would like to express my appreciation to my friends in the doctoral course, Mr. Keita Uemura, Mr. Yuma Shimizu, and Ms. Nana Kamiya. They made my university life so joyful and helped me maintain my motivation for this research.

Special acknowledgement is extended to the members of the Urban Management Systems Laboratory. Particularly, I am deeply indebted to Mr. Ryota Kashima, Mr. Kyohei Ambai, Mr. Kyosuke Iseki, and Mr. Den Choka, who are master course students, Ms. Chenlu Song, a doctoral student, and Mr. Atushi Otani, a former student who is now working for the Ministry of Land, Infrastructure, Transport and Tourism. They have been my irreplaceable colleagues since I entered Kyoto University and have helped me with my laboratory life. I also wish to express my appreciation to Mr. Tanawat Tangjarudritaratorm and Mr. Jintong Zhang, who are doctoral students, and to Mr. Shogo Izawa, Mr. Shunsuke Koshityama, and Mr. Kaixuan Yuan, who are master course students, for their warm support. I would also like to acknowledge all past and present members of this laboratory.

This research has been supported by the Japan Society for the Promotion of Science (JSPS) Grant-in-Aid for JSPS Fellows [Subject No. 18J12549]. I am deeply grateful for their financial support.

Finally, I offer my most heartfelt appreciation to my family - my parents, Toshiro and Manami, my sisters, Kaede, Ai, and Yume, and my grandparents, Hanako, Nobutaka, and Miyako. They have

believed in me and patiently encouraged me throughout my years of study. The completion of this dissertation would have never been possible without their immense support.

Table of Contents

Abstract .... **III**

Acknowledgements .... **VI**

List of Tables and Figures .... **XIII**

Chapter 1 Introduction **1**
- 1.1 Background 1
- 1.2 Objective 3
- References 5

Chapter 2 Literature Review **7**
- 2.1 Technical development for geological disposal of high-level radioactive waste 7
- 2.2 Evolution of hydraulic property of rock 9
  - 2.2.1 Evolution of hydraulic property of rock due to fracture evolution 9
  - 2.2.2 Evolution of hydraulic property of rock due to mineral reactions 10
- 2.3 Coupled multi-physics numerical simulations 17
- 2.4 Scope and structure 20
- References 22

Chapter 3 Coupled Thermal-Hydraulic-Mechanical-Chemical Modeling by Incorporating Pressure Dissolution for Estimating Permeability Change within Matrix of Porous Rock **27**
- 3.1 Overview 27
- 3.2 Model description 28
  - 3.2.1 Governing equations 30
  - 3.2.2 Modification of porosity and related permeability 37
- 3.3 Model verification 37
- 3.4 Long-term predictions of permeability 42
  - 3.4.1 Modeling conditions 43
  - 3.4.2 Prediction results 46
- 3.5 Summary 52
- References 53

Chapter 4 Multi-Physics Simulations for Predicting the Evolution of Permeability and Reactive Transport Behavior within Rock Fractures 57
4.1 Overview 57
4.2 Model description 61
  4.2.1 Constitutive equations 61
  4.2.2 Mineral reactions 63
  4.2.3 Aperture change with mineral reactions 67
4.3 Model verification 70
  4.3.1 Replicating experimental measurements 70
  4.3.2. Comparisons with experimental measurements 76
4.4 Summary 87
References 89

Chapter 5 Coupled Thermal-Hydraulic-Mechanical-Chemical Model Incorporating Pressure Dissolution with Dual Porosity Theory and Its Application to Long-term Flow Simulation of Fractured Rock 95
5.1 Overview 95
5.2 Numerical model 96
  5.2.1 Model description 96
  5.2.2 Governing equations 97
    (a) Fluid flow 98
    (b) Stress analysis 100
    (c) Heat transfer 100
    (d) Reactive transport 101
    (e) Mineral reactions in porous rock 101
    (f) Mineral reactions in rock matrix 102
    (g) Permeability change in rock matrix 103
    (h) Mineral reactions in rock fractures 103
    (i) Permeability change in rock fractures 105
5.3 Numerical analysis 106
5.4 Analysis results 109
  5.4.1 Long-term evolution of permeability 109
  5.4.2 Parametric study 113
5.5 Summary 114
References 116

Chapter 6 Coupled Thermal-Hydraulic-Mechanical-Chemical Analyses for Fractured Rock by Incorporating Damage Theory......**119**
6.1 Overview......119
6.2 Numerical model......120
  6.2.1 Model description......120
  6.2.2 Governing equations......121
    (a) Stress analysis......123
    (b) Damage theory......124
    (c) Heterogeneity of mechanical properties......126
    (d) Fluid flow......129
    (e) Heat transfer......130
    (f) Reactive transport......130
    (g) Pressure dissolution within fractures......131
    (h) Free-face dissolution/precipitation within fractures......135
    (i) Fracture aperture change......135
    (j) Relation between fracture initiation/propagation and contact area ratio with change in fracture aperture......136
6.3 Numerical simulation......137
  6.3.1 Verification of fracture initiation/propagation......137
  6.3.2 Numerical analysis related to high-level radioactive geological disposal......141
    (a) Analysis of cavity excavation......143
    (b) Long-term coupled THMC analysis......146
6.4 Summary......155
References......157

Chapter 7 Conclusions and Future Studies......**161**
References......167

List of Tables and Figures

Tables

Table 3.1 Values of α_m (m = 0-7) in Eq. (3.13).

Table 3.2 Calculation parameters to simulate experimental results.

Table 3.3 Calculation parameters to simulate long-term permeability.

Table 4.1 Compositions of granite and mudstone$^{4.6)}$.

Table 4.2 Calculation setting of mineral composition and roughness factor in calculations for E-3$^{4.6),4.37)}$.

Table 4.3 Calculation settings of mineral composition and roughness factor in calculations for H-11$^{4.36),4.38)}$.

Table 4.4 Parameters of kinetic dissolution rate constant for minerals$^{4.39)\sim4.45)}$.

Table 4.5 Calibration of parameters used in analysis$^{4.6),4.30),4.27)\sim4.45)}$.

Table 5.1 Parameters used in calculation$^{5.20)\sim5.22)}$.

Table 6.1 Parameters used in simulation of uniaxial compression test.

Table 6.2 Parameters used in simulation for predicting changes in rock permeability.

Figures

Fig. 2.1 Example analysis: evolutions of temperature and pH in the near-field$^{2.8)}$.

Fig. 2.2 Conceptual models showing newly created and pre-existing fractures around a gallery. The extent of the EDZ, shown as a gray-colored zone, and that of the newly created fracture on the floor side are poorly understood$^{2.22)}$.

Fig. 2.3 Schematic of pressure dissolution for twin contacting grains comprising an aggregate and fractured rock comprising a discontinuity. At the contacts, the mineral dissolves due to the high localized stresses, and the dissolved mass diffuses from the interface into the pore space. Finally, precipitation occurs on the free faces of the pore walls$^{2.32)}$.

Fig. 2.4 Normalized silica as a function of time for two experiments at 150°C during which effective stresses of 345 bar (A) and 690 bar (B) are applied and removed. The vertical lines indicate changes in effective stress and the separate regions of constant effective stress$^{2.35)}$.

Fig. 2.5 Porosity as a function of time for three experiments conducted at 150°C and one at 23°C$^{2.35)}$.

Fig. 2.6 SEM photomicrographs of indented grain contacts. A: from experiment at 150°C with P_e =

345 bar and B: from experiment at 150°C with $P_e = 690$ bar[2.35)].

Fig. 2.7 Schematic of flow-through experiment and rock sample. Effluent water is recorded to evaluate the flow rate throughout the experiment, and the portion is utilized for chemical analysis[2.34)].

Fig. 2.8 Evolution of effluent element concentrations of Si, Al, K, Fe, Ca, Na, and Mg at confining pressures of 10 MPa (ef-1) and 5 MPa (ef-2 and ef-3). They are measured using ICP-AES. All element concentrations are augmented at 90°C [2.34)].

Fig. 2.9 Evolution of fracture aperture at confining pressures of 10 MPa (ef-1) and 5 MPa (ef-2 and ef-3). The smaller aperture is apparent in ef-1 because of the higher compactive pressure. For ef-2 and ef-3, the behaviors at 90°C (gray area) match each other well[2.34)].

Fig. 2.10 Conceptual model of coupled processes in the near-field[2.8)].

Fig. 2.11 Schematic of pressure dissolution. At the grain-to grain contacts, the mineral dissolves due to the high stress concentration. Solutes diffuse from the interface into the pore space. Finally, precipitation occurs as a result of the oversaturation of the solutes in the pore fluid[2.46)].

Fig. 2.12 Structure of thesis.

Fig. 3.1 THMC interactions considered in the developed numerical model.

Fig. 3.2 Geometrical model of grain-to-grain contact. Initially, two grains contact each other with an initial contact-area ratio of R_{c0}. As compaction proceeds, due to the pressure dissolution, contact-area ratio R_c increases and free-face dissolution/precipitation occurs simultaneously, resulting in porosity modification.

Fig. 3.3 Comparison of porosity reduction with time between experimental data[3.24)] and predictions by the model.

Fig. 3.4 Comparison of silica concentration in pore fluid between experimental data[3.24)] and predictions by the model.

Fig. 3.5 Calculation domain. The calculation domain is a rectangle with vertical and horizontal lengths of 700 and 12.2 m, respectively. The cavity, with a diameter of 2.22 m, is excavated by lateral setting at a depth of 450 m. The EDZ ranges in the radial direction from the cavity wall to 0.8 m.

Fig. 3.6 Distribution of von Mises stress before and after cavity excavation.

Fig. 3.7 Temperature change with time that is used as the boundary condition applied on the periphery of the cavity[3.39)].

Fig. 3.8 Change in temperature distribution with time in the range of 10^0 to 10^4 years under the PS condition.

Fig. 3.9 Change in Si concentration distribution with time in the range of 10^0 to 10^4 years under the PS condition.

Fig. 3.10 Changes in normalized permeability with time in the range of 10^0 to 10^4 years under the no-PS condition. No permeability change is confirmed.

Fig. 3.11 Changes in normalized permeability with time in the range of 10^0 to 10^4 years under the PS condition. The permeability decreases with time. The reduction is especially significant around the periphery of the cavity.

Fig. 3.12 Specific locations where changes in permeability with time are observed.

Fig. 3.13 Permeability changes with time at specific locations indicated in **Fig. 3.12**: (a) the no PS condition and (b) the PS condition.

Fig. 3.14 Permeability changes with time under the PS condition at No. 1, indicated in **Fig. 3.12**: (a) initial porosity of 0.40 and (b) 0.45.

Fig. 4.1 Geometrical model that includes representative element in rock fracture area4.4). Tributary area A^{l}_{t} (center) is the representative element composed of asperity contact area $R_{f,c}\,A^{l}_{t}$ and pore space (right side).

Fig. 4.2 Relation between fracture aperture and contact-area ratio4.6).

Fig. 4.3 Sequential procedure to conduct consistent calculations of changes in aperture with time.

Fig. 4.4 Schematic of flow-through experiment (left side) and rock samples (right side) 4.6).

Fig. 4.5 Model geometry for analysis of E-3 and H-11

Fig. 4.6 Comparisons of evolution in fracture aperture (E-3) between measurements and predictions with different values for *a* used in Eq. (4.30).

Fig. 4.7 Comparisons of element concentrations (E-3) between measurements and predictions with different values for *a* used in Eq. (4.30): (a) Si, (b) Al, (c) K, (d) Fe, (e) Ca, (f) Na, and (g) Mg.

Fig. 4.8 Comparisons of element concentrations (E-3) between measurements and predictions with a = 0.03 used in Eq. (4.30)

Fig. 4.9 Comparisons of evolution of fracture aperture (H-11) between measurements and predictions with different values for *a* used in Eq. (4.30).

Fig. 4.10 Comparisons of element concentrations (H-11) between measurements and predictions with different values for *a* used in Eq. (4.30): (a) Si, (b) Al, (c) K, (d) Fe, (e) Ca, (f) Na, and (g) Mg..

Fig. 4.11 Comparisons of element concentrations (H-11) between measurements and predictions with a = 0.06 used in Eq. (4.30): (a) for whole experimental period and (b) for experimental period after 200 h.

Fig. 5.1 THMC interactions considered in the developed model.

Fig. 5.2 Calculation flow.

Fig. 5.3 Concept of dual porosity theory5.16).

Fig. 5.4 Geometrical model that includes representative element in the rock fracture area[5.12)].

Fig. 5.5 Calculation domain.

Fig. 5.6 Evolution of mean effective stress after cavity excavation.

Fig. 5.7 Evolution of permeability with time under (a) the no PS condition and (b) the PS condition.

Fig. 5.8 Measurement points.

Fig. 5.9 Permeability changes with time at measurement points in No PS and various PS conditions.

Fig. 5.10 Permeability changes with time at measurement Point1 with different values for a = 0.07, 0.12, and 0.17 used in Eq. (5.23).

Fig. 6.1 THMC interactions considered in the developed model. The interactions expressed as gray arrows were not considered in our previous model[6.26)] introduced in **Chapter 5**, while the ones expressed as white arrows were taken into account.

Fig. 6.2 Calculation flow.

Fig. 6.3 Constitutive law of elastic damage theory under uniaxial tensile stress and uniaxial compressive stress[6.20),6.22),6.29)] .

Fig. 6.4 Statistical distribution of probability density function for uniaxial compressive strength with different homogeneity indices (m = 5.0, 4.0, 3.0, 2.0, 1.5) and characteristic value of $f_{c0}{}^{s}$ = 200 MPa.

Fig. 6.5 Distribution of uniaxial compressive strength within numerical domains with different homogeneity indices (m = 5.0, 3.0, 1.5) and characteristic value that $f_{c0}{}^{s}$ = 200 MPa.

Fig. 6.6 Schematic of pressure dissolution at contacting asperities within the fracture[6.11)].

Fig. 6.7 Geometrical model that includes representative element in rock fracture area[6.11),6.38)].

Fig. 6.8 Driving forces for generating fractures in two failure modes.

Fig. 6.9 Calculation domain and boundary conditions for simulation of uniaxial compression test using granite.

Fig. 6.10 Comparison of relationship between vertical stress and strain between experimental result and prediction.

Fig. 6.11 (a) Evolution of damage variable D obtained from simulation of uniaxial compression test using granite (Point A and Point B correspond to Point A and Point B shown in **Fig. 6.10**, respectively) and (b) fracture distribution obtained from the experiment.

Fig. 6.12 Calculation domain of simulation for predicting changes in rock permeability.

Fig. 6.13 Description of excavation analysis.

Fig. 6.14 Evolution of damage variable D with different values for lateral pressure coefficient K_0:

(a) $K_0 = 0.5$, (b) $K_0 = 1.0$, and (c) $K_0 = 1.5$.

Fig. 6.15 Temperature change with time used as boundary condition applied on periphery of cavity6.40).

Fig. 6.16 Evolution of permeability with different values for lateral pressure coefficient under no-PS condition: (a) $K_0 = 0.5$, (b) $K_0 = 1.0$, and (c) $K_0 = 1.5$.

Fig. 6.17 Evolution of permeability with different values for lateral pressure coefficient under PS condition: (a) $K_0 = 0.5$, (b) $K_0 = 1.0$, and (c) $K_0 = 1.5$.

Fig. 6.18 Quantity of fracture aperture change due to pressure dissolution and free-face dissolution/precipitation: (a) b^{PS} (quantity of fracture aperture change due to pressure dissolution used in Eq. (6.34)) and (b) b^{FF} (quantity of fracture aperture change due to free-face dissolution/precipitation used in Eq. (6.33)).

Fig. 6.19 Distribution of permeability in tensile damage zone.

Fig. 6.20 Evolution of normalized mean permeability with different values for lateral pressure coefficient.

Chapter 1

Introduction

1.1 Background

In recent years, as most of the nuclear power plants in Japan have ceased operations, the safe disposal of the high-level radioactive waste that is the byproduct of long-term nuclear power generation has become an important issue. In accordance with the Designated Radioactive Waste Final Disposal Act (enacted in May 2000), the high-level radioactive waste that is generated from the processing of spent nuclear fuel must be processed into vitrified objects. Then, after remaining isolated in a cooling storage facility for about 30 to 50 years1.1), the objects need to be disposed under the ground at a depth greater than 300 m. In Japan, the multiple barrier system has been discussed for use in the geological disposal of high-level radioactive waste. The system is composed of an artificial barrier and a natural barrier. The artificial barrier is formed by inserting vitrified high-level radioactive waste into a metal canister overpack, which subsequently is covered with buffer material composed primarily of bentonite1.2). By adding a natural barrier, composed of a stable host rock that performs the function of delaying the transport of the radionuclides, the multiple barrier system isolates the radionuclides within the deep underground. As the high-level radioactive waste is disposed and left in the deep underground for thousands of years, the prediction of the long-term evolution of the hydraulic property of the rock surrounding the radioactive waste is essential for evaluating the performance of geological disposal systems.

During the geological disposal, phenomena such as heat radiation from the waste package, mass transport due to the ground water flow, fracture initiation/propagation within rock masses due to the redistribution of stress induced by the excavation of the disposal cavity, and mineral dissolution and precipitation occur within the surrounding rock and affect each other, bringing about complicated coupling interactions[1.3)]. It is expected that the hydraulic property of the surrounding rock may change with time due to the coupled interactions among the thermal–hydraulic–mechanical–chemical components. Therefore, in order to evaluate the long-term evolution of the hydraulic property of the surrounding rock, it is necessary to conduct coupled thermal-hydraulic-mechanical-chemical (later addressed as THMC) numerical simulations that comprehensively take into account the phenomena related to the thermal, hydraulic, mechanical, and chemical components as well as the interactions among these phenomena.

In the prediction of the long-term evolution of the hydraulic property of the target rock, the geochemical phenomena, such as the mineral reactions of the mineral dissolution and the precipitation occurring on the free-face and at the contact area of the grains and fractures within the rock, comprise the most important aspect. In the deep underground where radioactive waste is disposed, the level of confining pressure is high, and the ambient temperature of the surrounding rock should increase due to the radiation of heat from the waste. Consequently, the dissolution and precipitation of the minerals composing the rock become eminent and may change the pore structure and permeability of the rock. The mineral dissolution and precipitation occurring on the free surfaces of the rock is called "free-face dissolution/precipitation"[1.4)], while the mineral dissolution occurring at the grain contacts and the contacting asperities within the rock fractures is called "pressure dissolution"[1.5)~1.12)]. Past studies[1.13)~1.15)] confirmed that pressure dissolution may change the permeability of the rock by several orders of magnitude over a long duration. Therefore, it is necessary to develop coupled THMC numerical models that can evaluate the influence of the mineral reactions (i.e., free-face dissolution/precipitation and pressure dissolution) in order to estimate the long-term evolution of the hydraulic property of the natural barrier.

To date, the long-term coupled phenomena in the near field, including the artificial and natural barriers, have been predicted by utilizing coupled THMC models[1.16), 1.17)]. However, the studies that employed these models mostly focused on the long-term behavior of the artificial barrier, and sufficient results have not been produced for predictions of the hydraulic property of the surrounding rock. There have been several THMC numerical models[1.18) ~ 1.20)] incorporating the mineral reactions within the rock, and while the mineral dissolution/precipitation occurring on the free surfaces of the rock has been taken into account, the effect of the pressure dissolution has not been taken into account. Precise predictions of the influence of the mineral reactions require that consideration be given to the pressure dissolution, and an extremely complex THMC coupling process may be necessary for this purpose. Moreover, the mineral reactions occurring within the rock fractures should be considered by adding the process of fracture evolution (fracture initiation/propagation). After all, numerical models that can accurately predict the long-term changes in permeability of the rock due to the mineral reactions under the THMC coupling conditions have not yet been developed.

1.2 Objective

Based on the aforementioned background, the aim of this study is to develop numerical models that can accurately predict the long-term changes in permeability of the rock due to the mineral reactions under coupled THMC conditions. In addition, by applying the developed models, predictions can be made of the long-term evolution of the permeability of the rock near high-level radioactive waste within geological disposal systems. In order to realize these predictions, two coupled TMHC numerical models that incorporate the mineral reactions within the rock matrix and the rock fractures are firstly developed, and the validity of the models is examined by replicating the experimental measurements. Subsequently, a coupled THMC numerical model that can consider the mineral reactions within the dual porosity system of the rock matrix and the rock fractures is proposed. Using this model, the long-term evolution of the permeability of the fractured rock near radioactive material is predicted, and the influences of the mineral reactions in the rock matrix and the rock fractures are investigated. Finally, a coupled THMC model is developed; it includes the process of the fracture initiation/propagation and the mineral dissolution/precipitation within the generated fractures. Employing the developed model, long-term THMC coupled simulations are conducted, including an excavation analysis for a disposal cavity under various initial ground pressure conditions, and scenarios are presented for the changes in permeability of the rock during the period of the geological disposal.

In this study, long-term predictions over 10^2~10^4 years are conducted using the developed models in order to estimate the evolution of the rock permeability during the geological disposal period. Most of the previous experimental works, performed to observe the changes in rock permeability under THMC coupled conditions, were conducted for periods of less than 1 year. No experiments have been conducted for long durations such as 10^2 years. Thus, although it is very difficult at this stage to confirm the validity of the long-term predictions conducted in this study, the developed models are validated by replicating the existing experimental measurements and considering complex coupled phenomena similar to those in actual environments in order to propose reliable prediction results.

References

1.1) Japan Nuclear Cycle Development Institute: Whole on the geological disposal of high-level radioactive waste plan. 2006.

1.2) Japan Nuclear Cycle Development Institute: Second Progress Report on Research and Development for the Geological Disposal of HLW in Japan, Supporting Report 2 Repository Design and Engineering Technology, H12: Project to Establish the Scientific and Technical Basis for HLW Disposal in Japan. JNC TN1410 2000-003, IV-139-IV-160.

1.3) Tsang, CF., ed.: Coupled Processes Associated with Nuclear Waste Repositories. Elsevier Inc.; ISBN 9780323142403; 2012.

1.4) Lasaga, AC.: Chemical Kinetics of Water-Rock Interactions. J. Geophys. Res., 1984; 89:4009-25.

1.5) Croizé, D., Renard, F., Bjørlykke, K. and Dysthe, DK.: Experimental calcite dissolution under stress: evolution of grain contact microstructure during pressure solution creep. J. Geophys. Res., 2010; 115, B09207, doi:10.1029/2010JB000869.

1.6) Neveux, L., Grgic, D., Carpentier, C., Pironon, J., Truche, L. and Girard, JP.: Experimental simulation of chemomechanical processes during deep burial diagenesis of carbonate rocks. J. Geophys. Res., 2014; 119, 984.1007, doi:10.1002/2013JB010516.

1.7) Raj, R.: Creep in polycrystalline aggregates by matter transport though a liquid phase. J. Geophys. Res., 1982; 87:4731-39.

1.8) Robin, P-YF.: Pressure solution at grain-to-grain contacts. Geochim. Cosmochim. Acta., 1978; 42:1383-89.

1.9) Spiers, CJ, De-Meer, S., Niemeijer, A.R. and Zhang, X.: Kinetics of Rock Deformation by Pressure Solution and the Role of Thin Aqueous Films. In: Frontiers Science Series, 2003:129e158.

1.10) Wely, PK.: Pressure solution and force of crystallization-A phenomenological theory. J. Geophys. Res., 1959; 64:2001-25.

1.11) Zhang, X., Spiers, C.J. and Peach, C.J.: Compaction creep of wet granular calcite by pressure solution at 28°C to 150°C. J. Geophys. Res., 2010; 115 (B9):B09217.

1.12) Zubtsov, S., Renard, F., Gratier, J.P., Guiguet, R., Dysthe, D.K. and Traskine, V.: Experimental pressure solution compaction of synthetic halite/calcite aggregates. Tectonophysics, 2004; 385:45-57.

1.13) Yasuhara, H., Elsworth, D. and Polak, A.: Evolution of permeability in a natural fracture: The significant role of pressure solution. J. Geophys. Res., 2004; 109(B3):B03204, doi:10.1029/2003JB002663.

1.14) Yasuhara, H., Kinoshita, N., Ohfuji, H., Lee, DS., Nakashima, S. and Kishida, K.: Temporal alteration of fracture permeability in granite under hydrothermal conditions and its interpretation by coupled chemo-mechanical model. Appl. Geochem., 2011; 26:2074-88.

1.15) Elias, BP. and Hajash, A.: Change in quartz solubility and porosity change due to effective stress: An experimental investigation of pressure solution. Geology, 1982; 20:451-54.

1.16) Suzuki, H., Nakama, S., Fujita, T., Imai and H., Sazarshi, M.: A long-term THMC assessment on the geochemical behavior of the bentonite buffer. J. Nucl. Fuel Cycle Environ., 2012; 19:39-50.

1.17) Tsang, Y.: Effects of coupled processes on a proposed high-level radioactive waste repository at Yucca Mountain. Nevada. Geological Society of America Memoirs, 2012; 209:363-93.

1.18) Rutqvist, J., Wu, Ys., Tsang, CF. and Bodvasson, G.: A modeling approach for analysis of coupled multiphase fluid flow, heat transfer, and deformation in fractured porous roc. Int. J. Rock Mech. Min. Sci., 2002; 39: 429-42.

1.19) Nasir, O., Fall, M. and Evgin, E.: A simulator for modeling of porosity and permeability changes in near field sedimentary host rocks for nuclear waste under climate changes influences. Tunneling and Underground Space Technology, 2014; 42:122-135.

1.20) Fall, M., Nasir, O. and Nguyen, T. S.: A coupled hydro-mechanical model for simulation of gas migration in host sedimentary rocks for waste repositories, Eng. Geol., 2014;176:24-44.

Chapter 2

Literature Review

2.1 Technical development for geological disposal of high-level radioactive waste

The Japan Nuclear Cycle Development Institute (currently, the Japan Atomic Energy Agency) indicated the technical reliability for the geological disposal of high-level radioactive waste in Japan by releasing a technical report in 1999 entitled, "Second Progress Report on Research and Development for the Geological Disposal of HLW in Japan". The report concluded that it is possible to perform the geological disposal of high-level radioactive waste in Japan[2.1)]. Following the release of this technical report, "The Designated Radioactive Waste Final Disposal Act" was enacted in May 2000, which established that high-level radioactive waste needs to be disposed in stable stratum deeper than 300 m[2.2)]. As mentioned in **Chapter 1,** the application of a multiple barrier system for high-level radioactive waste disposal has been discussed in Japan. The system consists of an artificial barrier and a natural barrier. The artificial barrier is formed by inserting vitrified high-level radioactive waste into a metal canister overpack, which subsequently is covered with buffer material composed primarily of bentonite. This artificial barrier is expected to prevent the leakage of radionuclides for about 1000 years. The host rock covering the artificial barrier is the natural barrier, which is expected to delay the transport of radionuclides[2.3)]. When securing the performance of a geological disposal system of high-level radioactive waste, evaluating the behavior of the ground water flow within the multiple barrier system that controls the radionuclide transport is one of the most important issues. In particular, it is essential to examine the long-term behavior of the ground water flow within the natural barrier that works as the final barrier for preventing the leakage of radionuclides. Thus, it is necessary that accurate long-term predictions of the hydraulic property of the surrounding rock that works as a natural barrier be made by numerical simulations.

To date, the physical and chemical phenomena in the near-field, that include artificial and natural barriers, have been investigated by various in-situ tests and numerical simulations2.4)~2.8). For example, Fuji et al.2.4) performed coupled in-situ thermo-hydro-mechanical experiments at Kamaishi Mine. The coupled THM numerical code “THAMES”, developed by Ohnishi et al.2.5), was validated by reproducing the above-mentioned in-situ experiments and then applying the code to the performance of a coupled THM analysis in the near-field to evaluate the long-term performance of the artificial barrier. The development of coupled numerical models was promoted mainly through an international research collaboration project called “DECOVALEX”, and numerical simulations using the developed models were conducted as part of this project2.6), 2.7). Suzuki et al.2.8) performed a coupled THMC numerical analysis considering the heat radiation and the chemical reactions in pore water for evaluating the influence of the geochemical changes in the near-field (**Fig. 2.1**). As described above, although various experimental and numerical works targeting the phenomena that occur in the near-field have been conducted, to date, sufficient results have not been obtained with respect to quantitative long-term predictions of the hydraulic property of the surrounding rock.

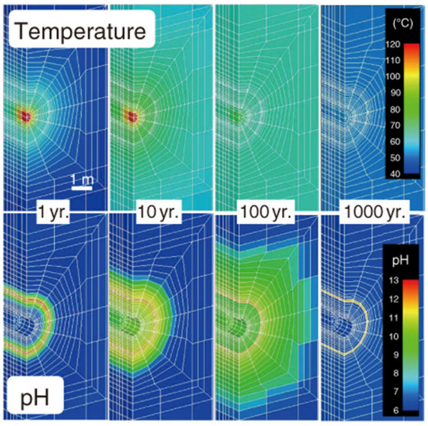

Fig. 2.1 Example analysis: evolutions of temperature and pH in the near-field2.8).

2.2 Evolution of hydraulic property of rock

As mentioned in **Chapter 1**, within the surrounding rock, phenomena such as heat radiation from the waste package, the mass transport with the fluid flow, the fracture initiation/propagation within rock masses due to the redistribution of stress induced by a cavity excavation for disposing radioactive waste, and the dissolution and precipitation of minerals composing the rock, interact with each other complicatedly[2.9)]. These phenomena and the coupled interactions among the phenomena for the thermal, hydraulic, mechanical, and chemical components should alter the hydraulic property of the surrounding rock with time. Among the phenomena, the ones that are of significant importance in terms of evaluating the evolution of the hydraulic property of the rock are described below.

2.2.1 Evolution of hydraulic property of rock due to fracture evolution

It is assumed that fracture initiation and propagation within rock masses during the excavation of a disposal cavity for radioactive waste should cause an increase in permeability and a decrease in the stiffness and strength of rock masses near the disposal cavity[2.10)]. The area where these changes in mechanical and hydraulic properties occur is called the Excavation Damaged Zone (EDZ)[2.11)]. In particular, the area where the permeability increases may become a main transport path for radionuclides after disposing the radioactive waste. The evolution and influence of the EDZ have been examined through various in-situ tests performed at underground research laboratories around the world[2.12)~2.22)]. For instance, Aoyagi et al.[2.20)] reported the results of an acoustic wave refraction survey and permeability tests that were performed within a horizontal gallery at a depth of 250 m in the Hokkaido Horonobe Underground Research Laboratory in Japan. The numerical analysis showed that the rock permeability increased to about two orders of magnitude greater than intact rock within the range of about 50 cm to 1.5 m from the cavity wall where a number of fractures were distributed. Sato et al.[2.21)] conducted an elastic wave tomography investigation and permeability tests at Tono

Mine and confirmed that the rock permeability increased by more than about two orders of magnitude within the range of 1.0 m from the cavity wall where the velocity of the elastic wave significantly decreased. Moreover, Tokiwa et al.[2.22] developed a conceptual model of the EDZ, shown in **Fig. 2.2**, by investigating the newly created and pre-existing fractures around a gallery from a geological observation of the tunnel face and the side-wall during the gallery excavation.

Based on the above review, it is necessary to develop a numerical model that can predict the evolution of the EDZ and its influences for evaluating the performance of the natural barrier. In addition, it is also important to predict the permeability evolution within the EDZ after the cavity has been excavated.

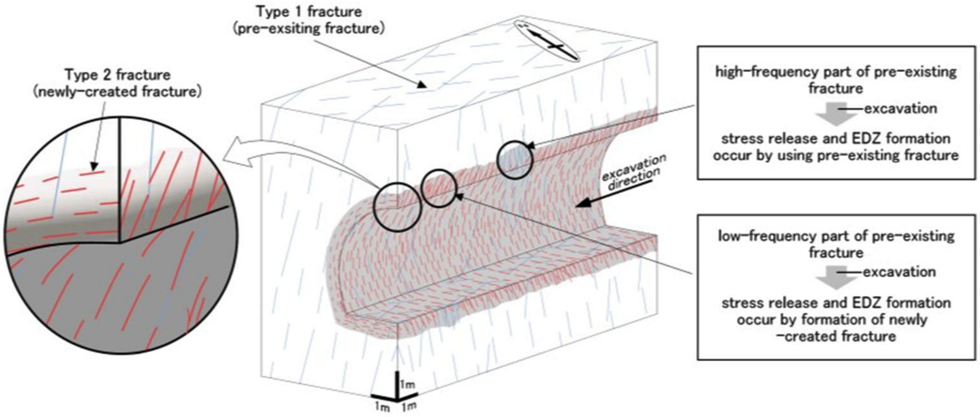

Fig. 2.2 Conceptual models showing newly created and pre-existing fractures around a gallery. The extent of the EDZ, shown as a gray-colored zone, and that of the newly created fracture on the floor side are poorly understood[2.22].

2.2.2 Evolution of hydraulic property of rock due to mineral reactions

It is known that mineral reactions, such as mineral dissolution/precipitation (i.e., free-face dissolution[2.23] and pressure dissolution[2.24)~2.31]), occurring within the rock may change the hydraulic property of the rock in a longer timescale when compared to the mechanical processes that include the fracture evolution and the elastic deformation of the rock structure. The mineral dissolution/precipitation that depends on the temperature acting on the rock and the concentration of solute in the pore water is called “free-face dissolution/precipitation”. The dissolution at the free face results in an increase in void, while the precipitation causes a decrease in void. The mineral dissolution occurring at the grain contacts and contacting asperities within rock fractures, that is controlled by the temperature and stress conditions, is called “pressure dissolution”; it reduces the pore space within the rock with time[2.32)~3.26)] (**Fig. 2.3**). In previous works[2.32)~2.36)], it was indicated that pressure dissolution may change the permeability of porous and fractured rocks by several orders of magnitude over a long duration.

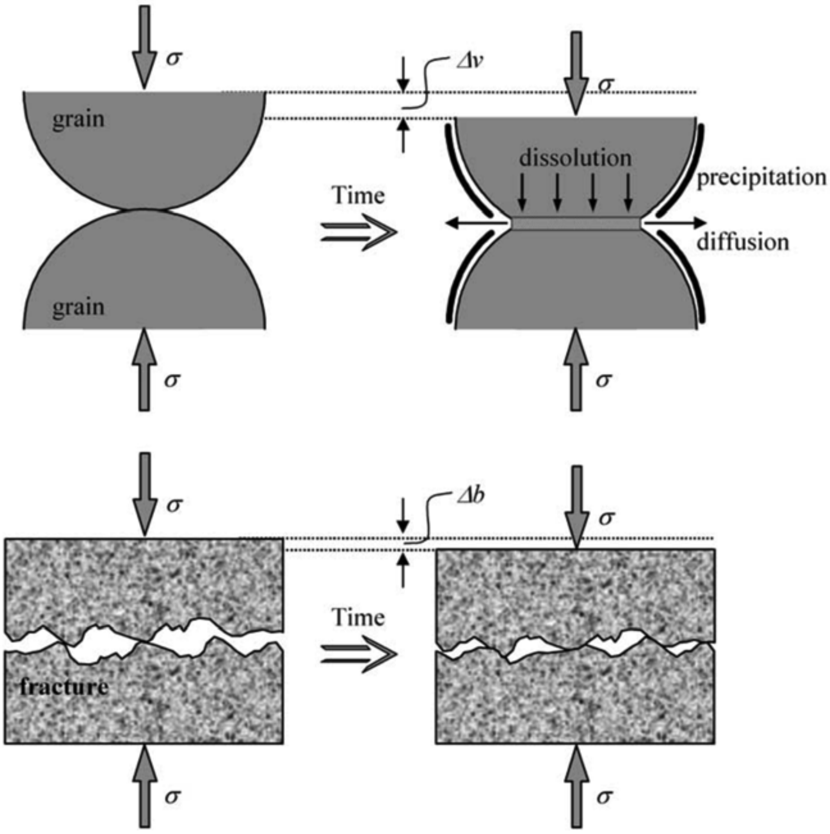

Fig. 2.3 Schematic of pressure dissolution for twin contacting grains comprising an aggregate and fractured rock comprising a discontinuity. At the contacts, the mineral dissolves due to the high localized stresses, and the dissolved mass diffuses from the interface into the pore space. Finally, precipitation occurs on the free faces of the pore walls[2.32)].

For example, Elias and Hajash[2.35)] conducted compaction experiments using saturated quartz sand under constant effective stresses of 69.0, 34.5, and 17.2 MPa at 150°C, and measured the changes in porosity and the silica concentration in the pore fluid over time in order to examine the chemical and physical processes associated with pressure dissolution. The experimental results confirmed that an increase in effective stress results in an increase in the porosity reduction rate and the silica concentration (**Figs. 2.4** and **2.5**) and that a decrease in porosity with time is caused by pressure dissolution at the grain contacts. In addition, the SEM photomicrographs of indented grain contacts, shown in **Fig. 2.6**, indicate that some contacts have ridges widened by dissolution and that these widened ridges express the occurrence of pressure dissolution at the grain contacts.

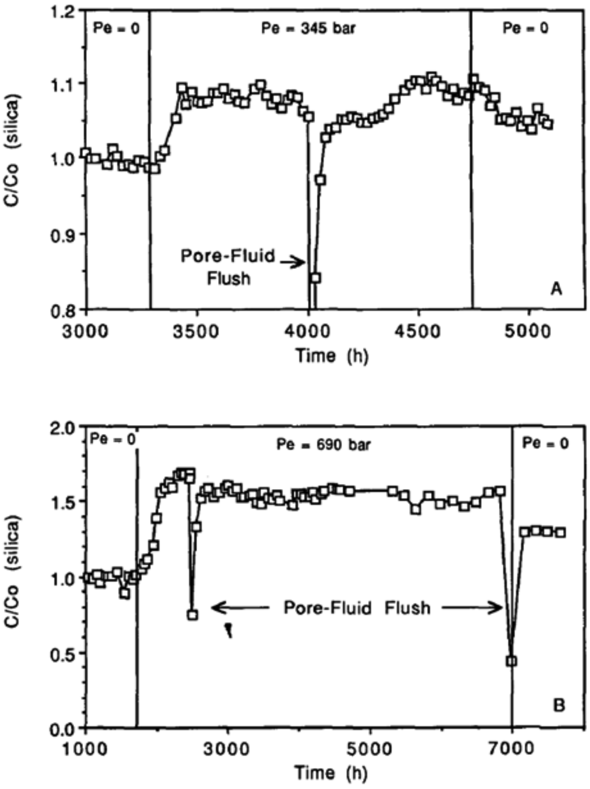

Fig. 2.4 Normalized silica as a function of time for two experiments at 150°C during which effective stresses of 345 bar (A) and 690 bar (B) are applied and removed. The vertical lines indicate changes in effective stress and the separate regions of constant effective stress[2.35)].

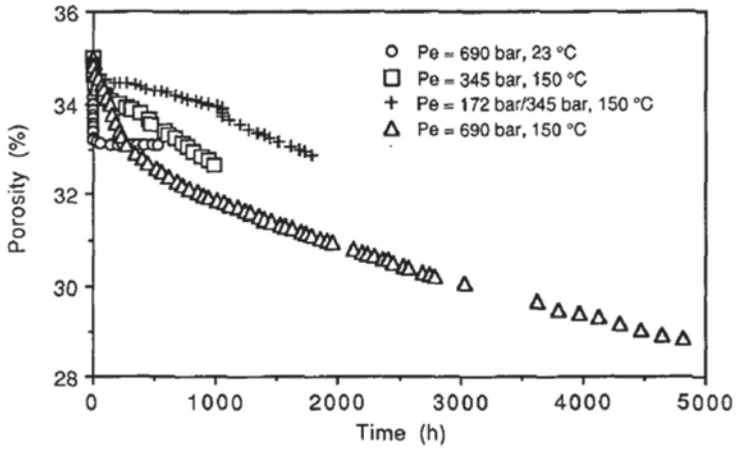

Fig. 2.5 Porosity as a function of time for three experiments conducted at 150°C and one at 23°C[2.35].

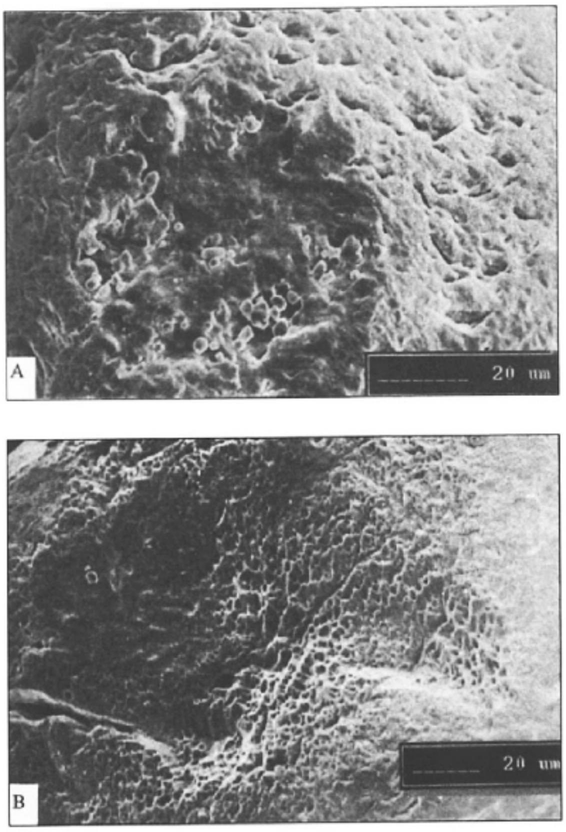

Fig. 2.6 SEM photomicrographs of indented grain contacts. A: from experiment at 150°C with P_e = 345 bar and B: from experiment at 150°C with P_e = 690 bar[2.35].

Moreover, Yasuhara et al.[2.34)] performed flow-through experiments using granite specimens with a single artificial fracture (**Fig. 2.7**) at two different temperatures (20°C and 90°C) and at two different confining pressures (5 MPa and 10 MPa), and the effluent element concentrations and hydraulic aperture obtained from the flow rate were measured over time (**Figs. 2.8** and **2.9**). The experimental results confirmed that the mineral dissolution depends on the prescribed stress and temperature conditions, which is the pressure dissolution, and should result in the evolution of the fracture aperture/permeability.

Based on the above review, within the rock near high-level radioactive waste, which is assumed to be under high-temperature and high-stress conditions, it is expected that mineral dissolution/precipitation, such as pressure dissolution, will occur and the rock permeability may change with time. Thus, in order to secure the long-term performance of the natural barrier, a numerical model needs to be developed that can accurately predict the changes in rock permeability with time due to mineral dissolution/precipitation.

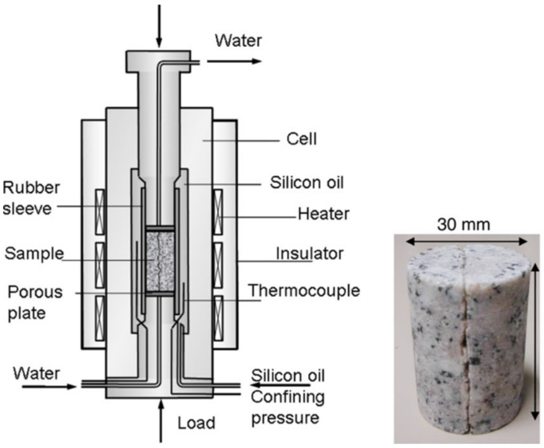

Fig. 2.7 Schematic of flow-through experiment and rock sample. Effluent water is recorded to evaluate the flow rate throughout the experiment, and the portion is utilized for chemical analysis[2.34].

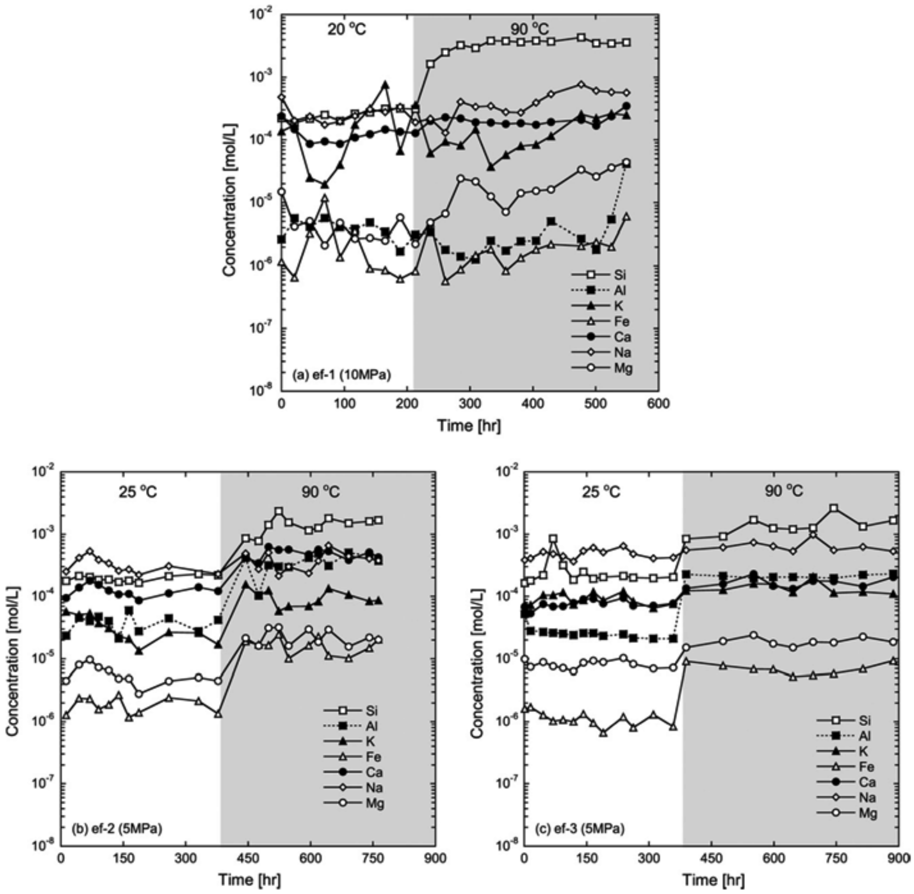

Fig. 2.8 Evolution of effluent element concentrations of Si, Al, K, Fe, Ca, Na, and Mg at confining pressures of 10 MPa (ef-1) and 5 MPa (ef-2 and ef-3). They are measured using ICP-AES. All element concentrations are augmented at 90°C [2.34].

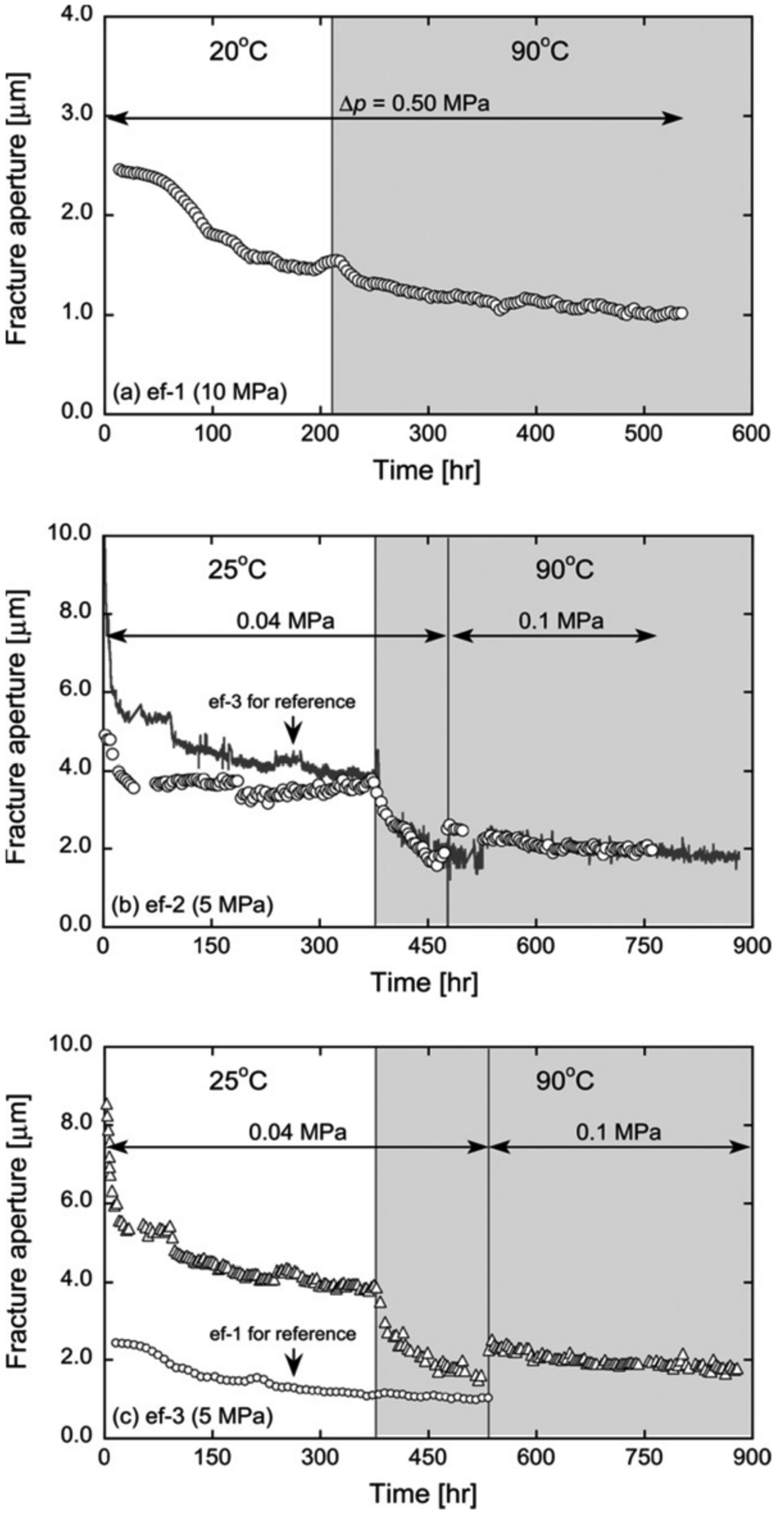

Fig. 2.9 Evolution of fracture aperture at confining pressures of 10 MPa (ef-1) and 5 MPa (ef-2 and ef-3). The smaller aperture is apparent in ef-1 because of the higher compactive pressure. For ef-2 and ef-3, the behaviors at 90°C (gray area) match each other well[2.34)].

2.3 Coupled multi-physics numerical simulations

Although various coupled THMC numerical models[2.8), 2.37)~2.42)] have been developed, most of them considered only the free-face dissolution/precipitation in the calculation of the geochemical processes, while the pressure dissolution at the grain contacts and at the contacting asperities within rock fractures, which depend on the temperature and stress conditions, was not taken into account. For example, in the coupled THMC processes considered in the model developed by Suzuki et al.[2.8)] (**Fig. 2.10**), the coupled interactions between the mechanical and chemical components (e.g., pressure dissolution) were not incorporated.

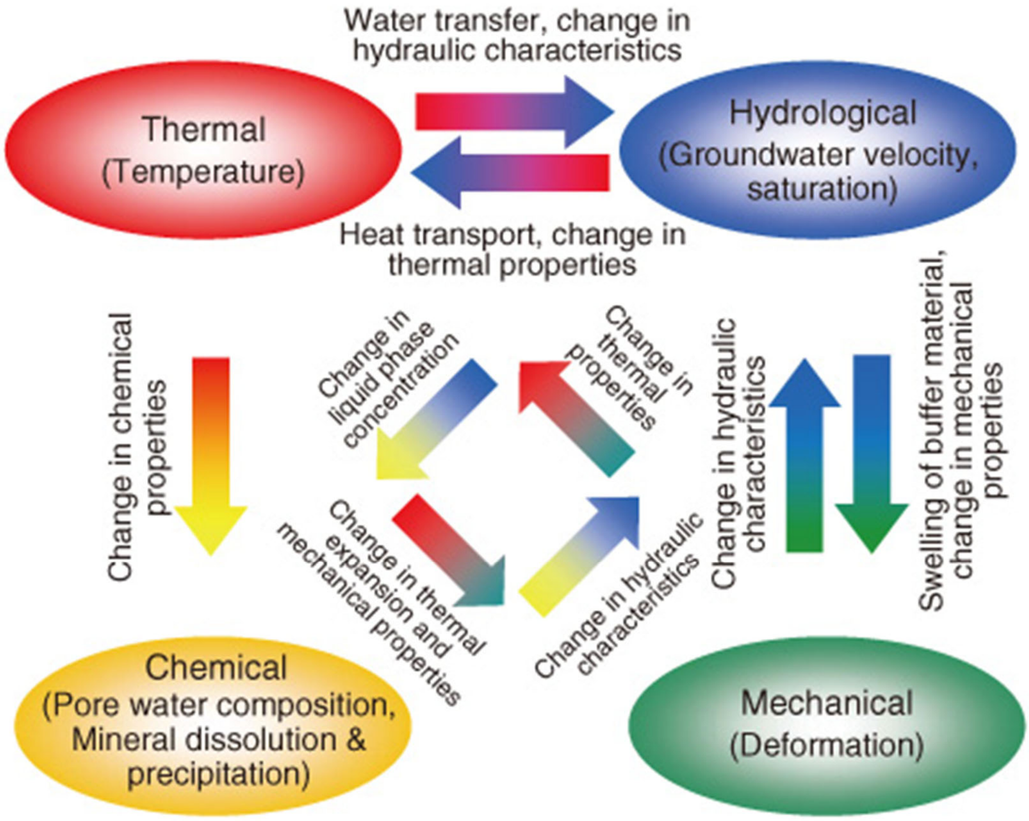

Fig. 2.10 Conceptual model of coupled processes in the near-field[2.8)].

To date, several conceptual models have been proposed to describe the pressure dissolution[2.43)~2.46)]. Yasuhara et al.[2.46)] proposed a theoretical conceptual model for the pressure dissolution at the grain-to-grain contacts including the three serial processes – (1) mineral dissolution at the stressed contacts, (2) diffusive transport through the thin film of water, and (3) re-precipitation of the mineral matter at the pore wall (**Fig. 2.11**). However, this conceptual model[2.46)] describes the pressure dissolution only in the representative elementary scale; and thus, it cannot be applied to numerical simulations at the field scale. Thus far, coupled THMC numerical models that can evaluate the influence of the pressure dissolution at the grain contacts in the field scale have not been well developed; and therefore, it is impossible to accurately evaluate the evolution of porosity/permeability within the rock matrix.

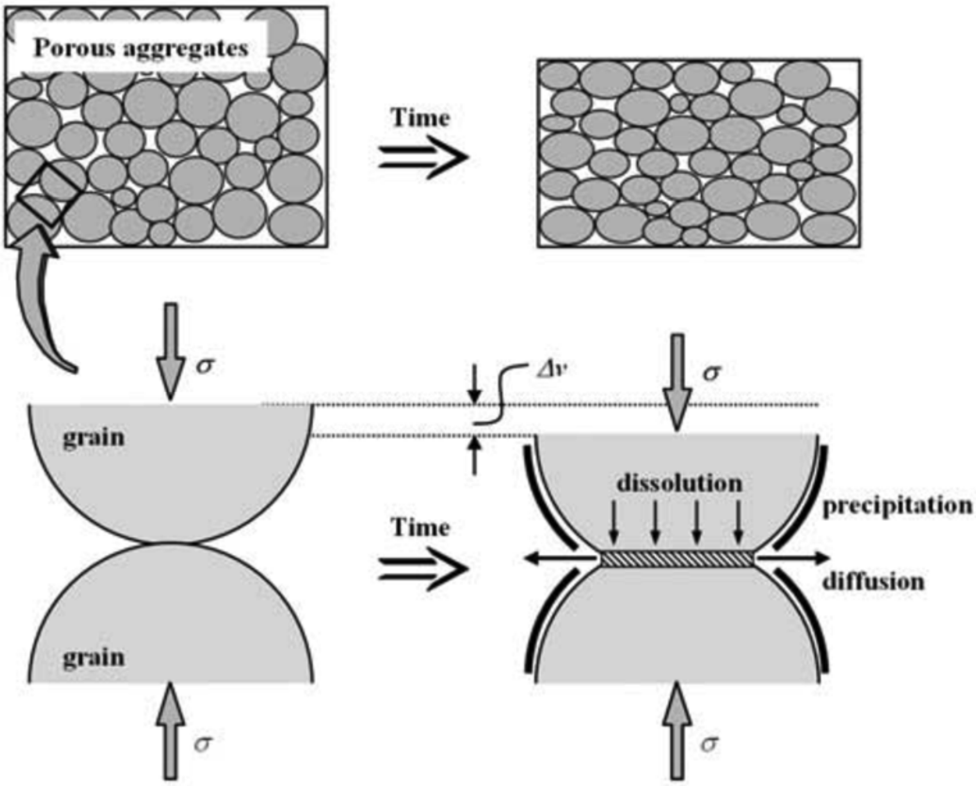

Fig. 2.11 Schematic of pressure dissolution. At the grain-to-grain contacts, the mineral dissolves due to the high stress concentration. Solutes diffuse from the interface into the pore space. Finally, precipitation occurs as a result of the oversaturation of the solutes in the pore fluid[2.46)].

Yasuhara et al.[2.32)] developed a theoretical conceptual model of the pressure dissolution at the contacting asperities within rock fractures by applying the developed model[2.46)]. In addition, although multiple research institutes have attempted to simulate the flow-through experiments of a single fracture in granite[2.32)] by utilizing coupled THMC models which incorporate conceptual models[2.32)], the experimental results cannot be reproduced without applying fitting parameters in the wide range of 245-10^6 in the calculation of the mineral reactions[2.47)]. Therefore, it is necessary to propose coupled numerical models that can precisely predict the changes in permeability of the rock fractures due to geochemical effects.

Moreover, in order to accurately estimate the evolution of the hydraulic property of fractured rock, coupled numerical models that can describe the alternation of the pore structure within both the rock matrix and the rock fractures is required; however, such models have not yet been developed.

In addition, in order to perform highly realistic predictions for changes in permeability within rock fractures in the actual field, the mineral reactions occurring within the rock fractures should be considered by adding the process of the fracture evolution (fracture initiation/propagation). For instance, numerous fractures are generated within rock masses during the excavation of a disposal cavity for radioactive waste, and after that, the mineral reactions of the free-face dissolution/precipitation and pressure dissolution within the generated fractures may occur, which may change the rock permeability with time. Recently, several coupled models [2.48)~2.53)] that can describe the evolution of the physical properties, such as the mechanical and hydraulic properties of rock masses, have been developed. For example, Wei et al.[2.48)] and Li et al.[2.49)] proposed coupled thermal-hydraulic models that can calculate the fracture evolution by applying a damage theory, including the heterogeneity of the mechanical property of the rock and the changes in the thermal property of the rock. Then, they predicted the evolution of the EDZ and the mechanical property of the rock under high-temperature and high-confining pressure conditions. As mentioned above, although various coupled models have been proposed, no models have ever been developed that can describe the process of mineral dissolution/precipitation within newly generated fractures.

2.4 Scope and structure

The structure of this thesis is shown in **Fig. 2.12**. Outlines of **Chapters 3** to **7** are summarized below.

In **Chapter 3**, a coupled THMC numerical model that can describe the changes in permeability within the matrix of porous rock is developed by incorporating the pressure dissolution at the grain contacts, and the validity of the model is examined by replicating the previous experiments[2.35)]. Subsequently, the long-term evolution of the permeability in porous rock is evaluated under the expected stress and temperature conditions where high-level radioactive waste has been disposed. In particular, the influence of the pressure dissolution on the changes in rock permeability is closely examined.

In **Chapter 4,** a coupled THMC numerical model incorporating the pressure dissolution at the contacting asperities of rock fractures is proposed in order to predict the changes in permeability of rock fractures. Subsequently, in order to confirm the validity of the developed model, a comparison is made between the model predictions and the experimental measurements obtained from flow-through experiments[2.32)] using granite and mudstone fractures.

In **Chapter 5,** a coupled THMC numerical model that describes the pressure dissolution both at the contacting asperities within rock fractures and at the grain contacts is developed by improving the models proposed in **Chapters 3** and **4**. Subsequently, by utilizing the proposed model, the long-term evolution of the permeability in fractured rock near radioactive waste is predicted and the impact of the pressure dissolution on the changes in permeability is closely evaluated

In **Chapter 6**, a coupled THMC model, including fracture initiation and propagation, is developed by incorporating the damage theory and the process of mineral dissolution/precipitation (i.e., pressure dissolution and free-face dissolution/precipitation) within the generated fractures. Subsequently, numerical simulations are conducted which incorporate the damage theory for the fracture evolution process in order to validate the developed model by simulating uniaxial compression tests on a granite specimen. Finally, predictions of the long-term evolution of the rock permeability in a high-level radioactive waste geological disposal facility are performed under various initial ground pressure conditions, and scenarios of the long-term permeability evolution of the rock during the geological disposal period are discussed in detail.

In **Chapter 7,** the conclusions of this thesis and recommendations for future works are provided.

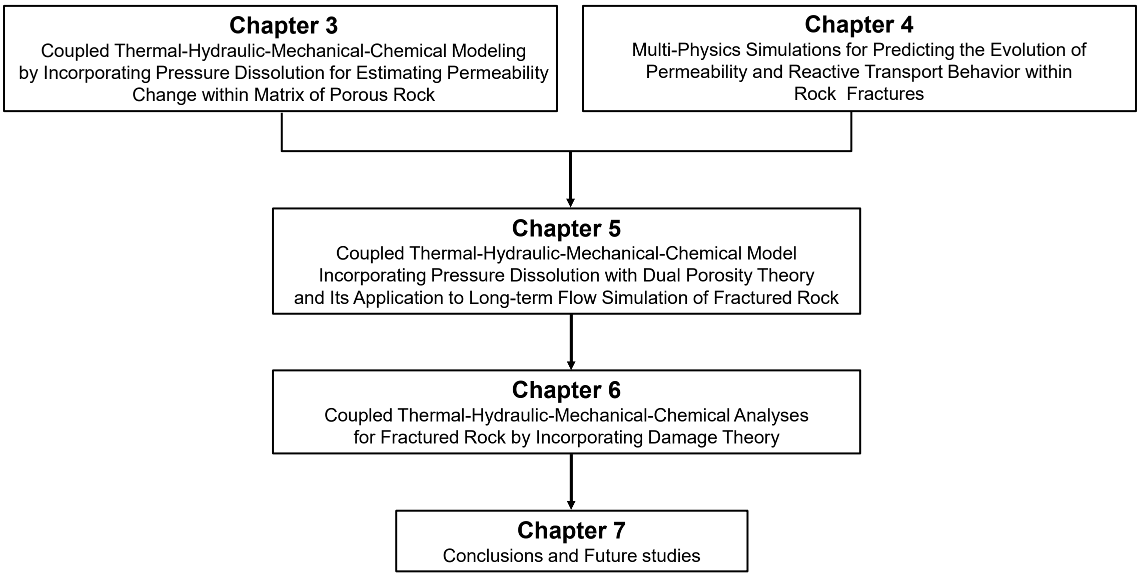

Fig. 2.12 Structure of thesis.

References

2.1) Japan Nuclear Cycle Development Institute, 1999: Second Progress Report on Research and Development for the Geological Disposal of HLW in Japan, General Report. JNC TN1400 99-020.

2.2) Japan Nuclear Cycle Development Institute: Whole on the geological disposal of high-level radioactive waste plan. 2006.

2.3) Japan Nuclear Cycle Development Institute, 1999: Second Progress Report on Research and Development for the Geological Disposal of HLW in Japan, Supporting Report 3, Safety Assessment of Geological Disposal System. JNC TN1400 99-023.

2.4) Fujita, T., Sugita, Y., Chijimastu, M., Amemitya, K. and Moro, Y.: Field Experiment of Coupled T-H-M Processed in the Near field. International Workshop, Key Issues in Water Isolation Research, Barcelona, 1998.

2.5) Ohnishi, Y., Shibata, H., and Kobayashi, A.: Development of Finite Element Code for the Analysis of Coupled Thermo-Hydro-Mechanical Behaviors of a Saturated-Unsaturated Medium. Proc. of Int. Symp. on Coupled Process Affecting the Performance of Nuclear Wastes Repository, Berkeley, 1985:263-268.

2.6) Jing, L., Stephansson, O., Tsang, C-F. and Kautsky, F.: DECOVALEX-Mathematical Models of Couples T-H-M Processes for Nuclear Wastes Repository. Executive Summer for Phases, I, II and III, SKI Report 96:58, 1996.

2.7) Jing, L., Stephansson, O., Bögesson, L., Chijimatsu, M., Kautsky, F. and Tsang, C-F.: DECOVALEX II, Technical Report-Task 2C, SKI Report 99:23, 1996.

2.8) Suzuki, H., Nakama, S., Fujita, T., Imai and H., Sazarshi, M.: A long-term THMC assessment on the geochemical behavior of the bentonite buffer. J. Nucl. Fuel Cycle Environ., 2012; 19:39-50.

2.9) Tsang, CF., ed.: Coupled Processes Associated with Nuclear Waste Repositories. Elsevier Inc.; ISBN 9780323142403; 2012.

2.10) Japan Nuclear Cycle Development Institute (2000) H12: project to establish the scientific and technical basis for HLW disposal in Japan-report 3 safety assessment of the geological disposal system, Technical report. JNC TN1410 2000-004, Tokai-mura, Japan.

2.11) Tsang , C.F., Bernier, F. and Davies, C.: Geohydromechanical processes in the excavation damage zone in crystalline rock, rock salt, and disposal. Int J Rock Mech Min Sci, 2005; 42:109-125.

2.12) Aoyagi, K. and Ishii, E.: A method for Estimating the Highest Potential Hydraulic Conductivity in the Excavation Damaged Zone in Mudstone, Rock Mech Eng, 2019; 52:385-401.

2.13) Zhang, C.-H.: The stress-strain-permeability behaviour of clay rock during damage and recompaction, J. Rock Mech. Geotech. Eng., 2016; 8:16-26.

2.14) Tsang, C-F., Jing, L., Stephansson, O. and Kautsky, F.: The DECOVALEX III project: A summary of activities and-lessons learned. Int. J. Rock Mech. Min. Sci., 2005; 42:593-610.

2.15) Homand-Etienne, F. and Sebaibi, A.: Study of microcracking of the Lac du Bonnet granite. Eurock-ISRM Int. Symp., 1996; 2:1353-1362.

2.16) Souley, M., Homand, F., Peda, S. and Hoxha, D.: Damaged-induced permeability changes in granite: a case example at the URL in Canada. Int. J. Rock Mech. Min. Sci., 2001; 38:297-310.

2.17) Carlsson, SR. and Young, RP.: Acoustic emission and ultrasonic velocity study of excavated-induced microcrack damage at the underground research laboratory. Int. J. Rock Mech. Min. Sci., 1993; 30:901-907.

2.18) Kelsall, PC., Case, JB. and Chabanne, CR.: Evaluation of excavation induced changes in permeability. Int. J. Rock Mech. Min. Sci., 1984; 21:121-135.

2.19) Bauer, C., Homand, F. and Henry, JP.: In situ low permeability pulse test measurements. Int. J. Rock Mech. Min. Sci., 1995; 32:357-63.

2.20) Aoyagi, K., Tsusaka, K., Nohara, S., Kubota K., Kondo, K., and Inagaki, D.: Hydrogeomechanical investigation on an Excavation Damaged Zone based on seismic surveys and hydraulic tests in the Horonobe Underground Research Laboratory. Proc. of 2014 ISRM Int. Symp. - 8th Asia Rock Mech. Symp, 2014:2804-2811.

2.21) Sato, T., Kikuchi, T., Sugihara, K. : In-situ experiments on an excavation disturbed zone induced by mechanical excavation in Neogene sedimentary rock at Tono Mine, Central Japan, Eng. Geol., 2000; 56:97–108.

2.22) Tokiwa, T., Tsusaka, K., Matsubara, M. and Ishikawa, T. : Fracture characterization around a gallery in soft sedimentary rock in Horonobe URL of Japan, Int. J. Rock Mech. Min. Sci., 2014; 65:1-7.

2.23) Lasaga, AC.: Chemical Kinetics of Water-Rock Interactions. J. Geophys. Res., 1984; 89:4009-25.

2.24) Croizé, D., Renard, F., Bjørlykke, K. and Dysthe, DK.: Experimental calcite dissolution under stress: evolution of grain contact microstructure during pressure solution creep. J. Geophys. Res., 2010; 115, B09207, doi:10.1029/2010JB000869.

2.25) Neveux, L., Grgic, D., Carpentier, C., Pironon, J., Truche, L. and Girard, JP.: Experimental simulation of chemomechanical processes during deep burial diagenesis of carbonate rocks. J. Geophys. Res., 2014; 119, 984.1007, doi:10.1002/2013JB010516.

2.26) Raj, R.: Creep in polycrystalline aggregates by matter transport though a liquid phase. J. Geophys. Res., 1982; 87:4731-39.

2.27) Robin, P-YF.: Pressure solution at grain to grain contacts. Geochim. Cosmochim. Acta., 1978; 42:1383-89.

2.28) Spiers, CJ, De-Meer, S., Niemeijer, A.R. and Zhang, X.: Kinetics of Rock Deformation by Pressure Solution and the Role of Thin Aqueous Films. In: Frontiers Science Series, 2003:129e158.

2.29) Wely, PK.: Pressure solution and force of crystallization-A phenomenological theory. J. Geophys. Res., 1959; 64:2001-25.

2.30) Zhang, X., Spiers, C.J. and Peach, C.J.: Compaction creep of wet granular calcite by pressure solution at 28°C to 150°C. J. Geophys. Res., 2010; 115 (B9):B09217.

2.31) Zubtsov, S., Renard, F., Gratier, J.P., Guiguet, R., Dysthe, D.K. and Traskine, V.: Experimental pressure solution compaction of synthetic halite/calcite aggregates. Tectonophysics, 2004; 385:45-57.

2.32) Yasuhara, H., Elsworth, D. and Polak, A.: Evolution of permeability in a natural fracture: The significant role of pressure solution. J. Geophys. Res., 2004; 109(B3): B03204, doi:10.1029/2003JB002663.

2.33) Yasuhara, H., Elsworth, D., Polak, A., Liu, J., Grader, A. and Halleck, P.: Spontaneous Permeability Switching in Fractures in Carbonate: Lumped Parameter Representation of Mechanically- and Chemically-Mediated Dissolution. Transp. Porous Media, 2006; 65:385-409.

2.34) Yasuhara, H., Kinoshita, N., Ohfuji, H., Lee, DS., Nakashima, S. and Kishida, K.: Temporal alteration of fracture permeability in granite under hydrothermal conditions and its interpretation by coupled chemo-mechanical model. Appl. Geochem., 2011; 26:2074-88.

2.35) Elias, BP. and Hajash, A.: Change in quartz solubility and porosity change due to effective stress: An experimental investigation of pressure solution. Geology, 1992; 20:451-54.

2.36) Dewers, T. and A. Hajash.: Rate laws for water-assisted compaction and stress-induced water-rock interaction in sandstones. J. Geophys. Res., 1995; 100 (B7):13093-13112.

2.37) Zheng L, Samper J.: A coupled THMC model of FEBEX mock-up test. Phys. Chem. Earth., 2008; 33:S486–98.

2.38) Taron J, Elsworth D, Min K-B.: Numerical simulation of thermal-hydrologic-mechanical-chemical processes in deformable, fractured porous media. Int. J. Rock Mech. Min. Sci., 2009; 46:842-54.

2.39) Nasir, O., Fall, M. and Evgin, E.: A simulator for modeling of porosity and permeability changes in near field sedimentary host rocks for nuclear waste under climate change influences. Tunnelling Underground Space Technology, 2014; 42:122-35.

2.40) Kim, J., Sonnenthal, E. and Rutqvist, J.: A sequential implicit algorithm of chemo-thermo-poro-mechanics for fractured geothermal reservoirs. Comput. Geotech., 2015; 76:59-71.

2.41) Lang, PS., Paluszny, A. and Zimmerman, RW.: Hydraulic sealing due to pressure solution contact zone growth in siliciclastic rock fractures. J. Geophys. Res., 2015; 120:4080‑4101, doi:10.1002/2015JB011968.

2.42) McDermott, C., Bond, A., Harris, AF., Chittenden, N. and Thatcher, K.: Application of hybrid numerical and analytical solutions for the simulation of coupled thermal, hydraulic, mechanical and chemical processes during fluid flow through a fractured rock. Environ. Earth. Sci., 2015; DOI 10.1007/s12665-015-4422-7.

2.43) Revil, A.: Pervasive pressure-solution transfer: a poro-visco-plastic model. Geophys. Res. Lett., 1999; 26:255-58.

2.44) Shimizu, I.: Kinetics of pressure solution creep in quartz: theoretical considerations. Tectonophysics, 1995; 245: 121-134.

2.45) Stephenson, LP., Plumley, WJ. and Palciauskas, VV.: A model for sandstone compaction by grain interpenetration. J. Sediment Petrol., 1992; 62:11-22.

2.46) Yasuhara, H., Elsworth, D. and Polak, A.: A mechanistic model for compaction of granular aggregates moderated by pressure solution. J. Geophys. Res., 2003; 108(11):2530, doi:10.1029/2003JB002536.

2.47) Bond, A., Brusky, I., Chittenden, N., Feng, X-T., Kolditz, O., Lang, P., Lu, R., McDermott, C., Neretnieks, I., Pan, P-Z., Sembera, J., Shao, H. and Yasuhara, H.: Development of approaches for modelling coupled thermal–hydraulic–mechanical–chemical processes in single granite fracture experiments. Environ. Earth. Sci., 2016; 75:1313.

2.48) Wei, CH., Zhu, WC. Chen, S. and Ranjith, PG.: A coupled thermal-hydrological-mechanical damage model and its numerical simulations of damage evolution in APSE. Materials, 2016; 9: 841, doi:10.3390/ma9110841.

2.49) Li, LC., Tang, CA., Wang, SY. and Yu, J.: A coupled thermo-hydrologic-mechanical damage model and associated application in a stability analysis on a rock pillar. Tunneling and Underground Space Technology, 2013; 34:38-53.

2.50) Wei, CH., Zhu, WC., Yu, QL., Xu, T. and Jeon, S.: Numerical simulation of excavation damaged zone under coupled thermal-mechanical conditions with varying mechanical parameters. Int. J. Rock Mech. Min. Sci., 2015; 75:169-181.

2.51) Xu, T., Zhou, GL., Heap, J-M., Zhu, WC., Chen, CF. and Boud, P.: The influence of temperature on time-dependent deformation and failure in granite: a mesoscale modeling approach. Rock Mech. Rock Eng., 2017; doi:10.1107/ s00603-0.17-1228-9.

2.52) Poulet, T., Karrech, A., Lieb, RK., Fisher, L. and Schaubs, P.: Thermal-hydraulic-mechanical-chemical coupling with damage mechanics using ESCRIPTRT and ABAQUAS. Tectonophysics, 2013:124-132.

2.53) Marschall, P., Giger, S., Vassiere, DLR., Shao, H., Leung, H., Nussbaum, C., Trick, T., Lanyon, B., Senger, R., Lisjak, A. and Alcolea, A.: Hydro-mechanical evolution of the EDZ as transport path for radionuclides and gas: insights from the Mont Terri rock laboratory (Switzerland). Swiss J. Geosci., 2017; 110:173-194.

Chapter 3

Coupled Thermal-Hydraulic-Mechanical-Chemical Modeling by Incorporating Pressure Dissolution for Estimating Permeability Change within Matrix of Porous Rock

3.1 Overview

This chapter proposes a coupled THMC model that examines the changes in permeability with time within the rock matrix.

As described in previous chapters, the rock that works as a natural barrier in the transportation of radionuclides should be affected by the convolved phenomena that include the heat transfer from the waste package, the groundwater flow, the variation in induced stress, and the mineral reactions such as mineral dissolution and precipitation3.1),3.2). Thus, a numerical model that can consider the coupled THMC processes is necessary for estimating the long-term evolution of the hydraulic property. Specifically, an accurate modeling of the mineral reactions taking place at the interface between the grain particles composing the rock and the pore water is of considerable importance for attaining precise estimations. Coupled THMC numerical models were previously proposed to deal with some engineering issues such as the geological disposal of CO_2 and radioactive waste, and energy production from geothermal reservoirs3.3)~3.9). By applying some of the above models, the long-term phenomena occurring in the artificial and natural barriers were estimated by assuming specific subsurface conditions, the heat transfer, the groundwater flow, the stress/deformation, and the mineral reactions. In the calculations of the mineral reactions in the THMC models, the mineral dissolution and precipitation taking place at the free face of the rock3.10) are typically taken into account, but the dissolution active at the grain contacts (e.g., pressure dissolution$^{3.11)\sim3.18)}$) is not considered . In past works$^{3.19)\sim3.23)}$, it was implied that pressure dissolution over a long duration may alter the permeability of porous and fractured rocks by several orders of magnitude; and thus, the phenomenon must be incorporated into the modeling process when examining the long-term evolution of the hydraulic property of the rock. Although several THMC numerical models have recently been developed that can take into account the process of pressure dissolution$^{3.7)\sim3.9)}$, most of the models address fracture media and do not predict the changes in hydraulic property within the matrix of porous rock.

In this chapter, a new coupled THMC numerical model was developed that incorporates the important process of pressure dissolution at the grain contacts, as well as the free-face dissolution and precipitation, and the capability of the model was validated by reproducing the experimental measurements obtained from Elias and Hajash (1992)$^{3.24)}$. Subsequently, the long-term alternation of the permeability within porous rock was estimated under the probable stress and temperature conditions where high-level radioactive waste is disposed. In particular, the influence of pressure dissolution on the evolution of the rock permeability was fully investigated.

3.2 Model description

The coupled THMC model proposed in this chapter enables the changes in the permeability of porous rock to be followed with time by taking into account the interactions of the thermal, hydraulic, mechanical, and geochemical processes (i.e., heat transfer, groundwater flow in saturated porous media, stress/deformation, mass transport, and mineral dissolution/precipitation). The processes included in this model are schematically summarized in **Fig. 3.1**.

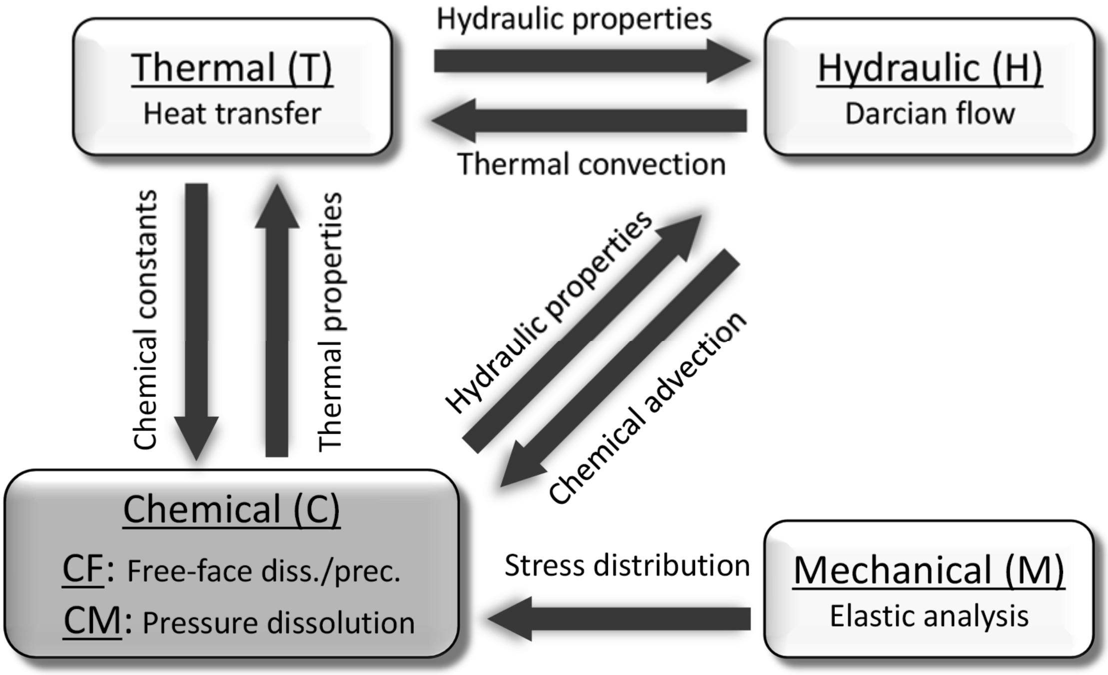

Fig. 3.1 THMC interactions considered in the developed numerical model.

As is obvious from this figure, two-way interactions are considered between the T and H, the H and C, and the C and T components. In the M component, the stress distribution is calculated and then rendered to calculate a chemo-mechanical process, which is expressed as CM in **Fig. 3.1**. In the C components, two different chemical processes are incorporated into the model; one is the free-surface dissolution/precipitation (CF) and the other is the pressure dissolution (CM). The pressure dissolution includes three serial processes - mineral dissolution at the stressed contacts, diffusive transport through the thin film of water, and re-precipitation of the mineral matter at the pore wall. The mineral dissolution at the stressed contacts is explicitly incorporated into the proposed model as the CM component. It should be noted that conceptual chemo-mechanical models have been proposed to simulate the change in permeability of porous and fractured rocks3.19)~3.23), and that the work in this chapter is an attempt to fit the conceptual model into the coupled numerical model and to perform numerical simulations at the field scale instead of at a representative element scale. It should also be noted that the interactions between the H and M and the M and T components are intentionally excluded in proposed model. These processes may influence the evolution of permeability, but the main focus of this chapter is to investigate the influences of the mineral reactions (i.e., free-face dissolution/precipitation and pressure dissolution) on the changes in permeability by the developed model.

3.2.1 Governing equations

The equations applied to calculate each of the THMC processes are presented in this section. In this chapter, COMSOL Multiphysics[3.25)], a simulation software using the Finite Element Method (FEM), is employed to solve the partial differential equations (PDE) describing the coupled THMC processes. The coupled THMC processes are solved sequentially by exchanging and updating the dependent variables (i.e., porosity/permeability, flow velocity, stress, temperature, and dissolution/precipitation rate constants).

The groundwater flow in saturated porous rock is modeled by the conservation of water mass and the Darcian flow, given by

$$\frac{\partial(\rho_w \phi)}{\partial t} + \nabla \cdot (\rho_w \boldsymbol{u}) = f_m , \tag{3.1}$$

$$\boldsymbol{u} = -\frac{\boldsymbol{k}}{\mu}(\nabla p + \rho_w g \nabla h) , \tag{3.2}$$

where ρ_w [kg m^{-3}] is the density of the fluid, ϕ [-] is the porosity, $\boldsymbol{u}$ [m s^{-1}] is the fluid velocity tensor, f_m [kg m^{-3} s^{-1}] is the source term for the flow, $\boldsymbol{k}$ [m^2] is the rock permeability tensor, μ [Pa s] is the fluid dynamic viscosity, p [Pa] is the pore pressure, g [m s^{-2}] is the gravity acceleration, and h [m] is the potential head.

The transfer of heat is calculated by considering thermal convection and conduction without the radiation effect, given by

$$(\rho C_p)_{eq}\frac{\partial T}{\partial t}+\rho_w C_{p,w}\boldsymbol{u}\cdot\nabla T=\nabla\cdot(\boldsymbol{\lambda}_{eq}\nabla T)+Q_h\,, \tag{3.3}$$

where T [K] is the system temperature, $(\rho\, C_p)_{eq}$ [J K^{-1} m^{-3}] is the equilibrium volumetric heat capacity, $C_{p,w}$ [J kg^{-1} K^{-1}] is the heat capacity of the fluid, $\boldsymbol{\lambda}_{eq}$ [W m^{-1} K^{-1}] is the equilibrium thermal conductivity tensor, and Q_h [W m^{-3}] is the heat source. $(\rho\, C_p)_{eq}$ and $\boldsymbol{\lambda}_{eq}$ can be calculated by the following equations:

$$(\rho C_p)_{eq}=(1-\phi)\,\rho_m C_{p,m}+\phi\,\rho_w C_{p,w}\,, \tag{3.4}$$

$$\boldsymbol{\lambda}_{eq}=(1-\phi)\,\boldsymbol{\lambda}_m+\phi\,\boldsymbol{\lambda}_w\,, \tag{3.5}$$

where ρ_m [kg m^{-3}] is the density of the solid, $C_{p,m}$ [J kg^{-1} K^{-1}] is the heat capacity of the solid, and $\boldsymbol{\lambda}_m$ and $\boldsymbol{\lambda}_w$ [W m^{-1} K^{-1}] are the thermal conductivity tensors of the solid and the fluid, respectively.

The mechanical response of the rock masses is calculated by the quasi-static equilibrium equation and the typical Hooke's law, as follows:

$$-\nabla\cdot\boldsymbol{\sigma}=\boldsymbol{F}_v\,, \tag{3.6}$$

$$\boldsymbol{\sigma}=\boldsymbol{E}:\boldsymbol{\varepsilon}\,, \tag{3.7}$$

where $\boldsymbol{\sigma}$ [Pa] is the stress tensor, $\boldsymbol{F_v}$ [Pa m^{-1}] is the body force, $\boldsymbol{E}$ [Pa] is the elasticity tensor, and $\boldsymbol{\varepsilon}$ [-] is the strain tensor. In the developed model, the thermal stress and the inelastic behavior are disregarded. A self-weight analysis is conducted to calculate the initial stress field, while changes in the stress distribution due to the excavation of the disposal cavity are calculated using these equations. .

The reactive transport equation that considers advection and diffusion is used to calculate the solute transport behavior. Neither the mechanical dispersion nor the retardation due to the sorption processes is taken into account here.

$$\frac{\partial(c_i\phi)}{\partial t}+\boldsymbol{u}\cdot\nabla c_i=\nabla\cdot(\phi\tau\,\boldsymbol{D}_{b,i}\nabla c_i)+R_i\,, \tag{3.8}$$

where c_i [mol m^{-3}] is the concentration of solute i in the pore water, τ [-] is the coefficient related to tortuosity, $\boldsymbol{D_{b,i}}$ [m^2 s^{-1}] is the diffusion coefficient tensor, and R_i [mol m^{-3} s^{-1}] is the source of solute *i*. The diffusion coefficient is determined by the system temperature and can be defined by an Arrhenius-type equation$^{3.26)}$, as follows:

$$D_{b,i} = D_{b,i}^{0} \exp(-E_{D,i}/RT)\,, \tag{3.9}$$

where $D_{b,i}^{0}$ [m^2 s^{-1}] and $E_{D,i}$ [J mol^{-1}] are the pre-exponential factor and the activation energy of the diffusion of solute *i*, respectively, and R [J mol^{-1} K^{-1}] is the gas constant.

The source term, R_i, is calculated by considering both the free-face dissolution/precipitation and the pressure dissolution, and can be expressed by

$$R_i = R_i^{FF} + R_i^{PS}\,, \tag{3.10}$$

where R_i^{FF} and R_i^{PS} [mol m^{-3} s^{-1}] are the rates of the free-face dissolution/precipitation and the pressure dissolution, respectively. They express the mineral dissolution and precipitation per volume and time. The rate of the free-face dissolution/precipitation is defined by$^{3.10)}$

$$R_i^{FF} = k_+ A (a_{H+})^q (1 - Q/K_{eq})\,, \tag{3.11}$$

where k_+ [mol m^{-2} s^{-1}] is the mineral dissolution rate constant, A [m^2 m^{-3}] is the specific surface area, a_{H+} [-] is the activity of H^+, and q [-] is the constant, which may be obtained from experimental observations in the literature. Q [-] is the ionic activity product and K_{eq} [-] is the equilibrium constant. When Q/K_{eq} <1, free-face dissolution occurs; when Q/K_{eq} >1, free-face precipitation occurs. The specific surface area is obtained by measurement using the BET method, as follows:

$$A = A_{BET}\,\rho_m\,, \tag{3.12}$$

where A_{BET} [m^2 kg^{-1}] is the specific surface area determined by the BET method. In this chapter, the rock is assumed to be composed purely of quartz, and subscript *i* in Eqs. (3.8) - (3.10) is omitted hereinafter. The equilibrium and the dissolution rate constants in Eq. (3.11) are obtained from PHREEQC$^{3.27)}$ and Rimstidt and Barnes (1980)$^{3.28)}$, respectively. These constants are temperature-dependent and are given via polynomial approximation and an Arrhenius expression, as follows:

$$K_{eq} = \sum_{m=0}^{7} \alpha_m T^m , \tag{3.13}$$

$$k_+ = k_+^0 \exp(-E_{k_+} / RT) , \tag{3.14}$$

where α_m (m = 0-7) [-] is the constant (see **Table 3.1**), $k^0{}_+$ [mol m^{-2} s^{-1}] is the pre-exponential factor, and E_{k+} [J mol^{-1}] is the activation energy of the mineral dissolution.

Table 3.1. Values of α_m (m = 0-7) in Eq. (3.13).

α_0	α_1	α_2	α_3
-187.4	3.012	-2.156×10^{-2}	8.622×10^{-5}
α_4	α_5	α_6	α_7
-2.065×10^{-7}	2.952×10^{-10}	-2.330×10^{-13}	9.374×10^{-17}

Incorporating the process of pressure dissolution into the developed model is the most important task in this chapter. As mentioned above, conceptual models that describe the process[3.19)~3.23)] have been developed. The flux that expresses the pressure dissolution is induced by the gradient in the chemical potential between the highly-stressed contacts and the less-stressed site of the pore walls[3.13),3.26)]. Dissolution is most conveniently defined in terms of a dissolution mass flux, $\dot{M}^{PS}$, the rate of the supply of the dissolved mass into the solution at the interface, given as[3.19)]

$$\dot{M}^{PS} = \frac{3 V_m^2 (\sigma_a - \sigma_c) k_+ \rho_g A_c}{RT} , \tag{3.15}$$

where V_m is the molar volume of the solid (2.27×10^{-5} m^3 mol^{-1} for quartz), σ_a [Pa] is the disjoining pressure[3.29)] equal to the amount by which the pressure acting at the contacts exceeds the hydrostatic pore pressure, ρ_g is the grain density (2650 kg m^{-3} for quartz), A_c [m^2] is the area of the grain contact, and σ_c [Pa] is the critical stress, which determines the stress state where the compaction of the grain aggregate will halt[3.30]. This stress is calculated by considering the energy balance under the applied stress and temperature conditions, given by[3.26),3.30)]

$$\sigma_c = \frac{E_m(1 - T / T_m)}{4V_m}, \tag{3.16}$$

where E_m and T_m are the heat and temperature of the fusion, respectively (E_m = 8.57 kJ mol^{-1} and T_m = 1883 K for quartz).

Based on Eq. (3.15), the rate of the pressure dissolution, R^{PS}, is derived through the following procedure. Firstly, the strain rate due to the pressure dissolution is expressed as[3.19)]

$$\dot{\varepsilon}^{PS} = \frac{\dot{M}^{PS}}{d\rho_g A_c} = \frac{3V_m^2 k_+}{RTd}\left(\frac{\sigma_{eff}}{R_c} - \sigma_c\right), \tag{3.17}$$

$$\sigma_a = \frac{\sigma_{eff}}{R_c}, \tag{3.18}$$

where $\dot{\varepsilon}^{PS}$ [-] is the strain state, d [m] is the grain diameter, σ_{eff} [Pa] is the effective stress exerted on the representative element, and R_c ($0 < R_c < 1$) [-] is the contact-area ratio. In this chapter, the FE analyses are conducted with the 2D domain in the following sections. To this end, the effective stress is replaced with the von Mises stress that can reduce any complex stress conditions down to a single representative scalar value. Thus, Eq. (3.17) may be expressed as

$$\dot{\varepsilon}^{PS} \approx \frac{3V_m^2 k_+}{RTd}\left(\frac{\sigma_{VM}}{R_c} - \sigma_c\right), \tag{3.19}$$

$$\sigma_{VM} = \sqrt{\frac{3}{2}\boldsymbol{\sigma} : \boldsymbol{\sigma}}, \tag{3.20}$$

where σ_{VM} [Pa] is the von Mises stress. When the system is assumed to consist of simple cubic packing with uniformly sized contacting spheres, as shown in **Fig. 3.2**, the volumetric rate due to the pressure dissolution can be defined by

$$\dot{V}^{PS} = \frac{\Delta d \cdot d^2}{\Delta t} = \dot{\varepsilon}^{PS} d^3 = \frac{3V_m^2 k_+ d^2}{RT}\left(\frac{\sigma_{VM}}{R_c} - \sigma_c\right), \tag{3.21}$$

where $\dot{V}^{PS}$ [m^3 s^{-1}] is the volumetric rate of the pressure dissolution. The dissolution rate, with regard to the representative element, can be simply obtained by dividing the volumetric rate by the

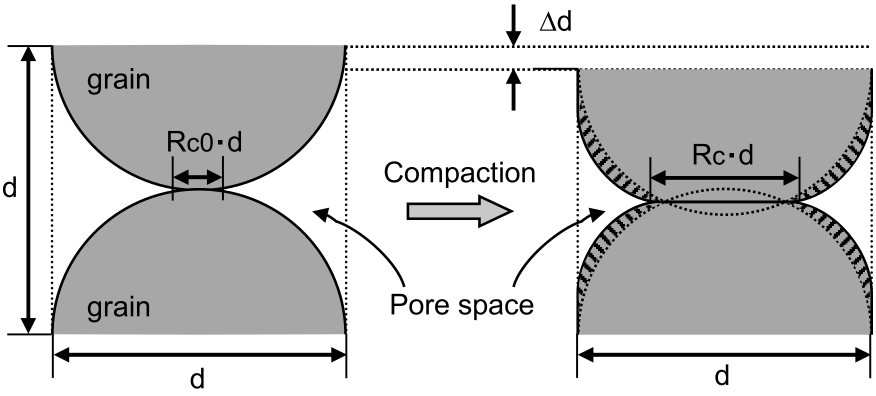

Fig. 3.2 Geometrical model of grain-to-grain contact. Initially, two grains contact each other with an initial contact-area ratio of R_{c0}. As compaction proceeds, due to the pressure dissolution, contact-area ratio R_c increases and free-face dissolution/precipitation occurs simultaneously, resulting in porosity modification.

the molar volume, as

$$\frac{\dot{V}^{PS}}{V_m} = \frac{3V_m k_+ d^2}{RT}\left(\frac{\sigma_{VM}}{R_c} - \sigma_c\right). \tag{3.22}$$

The volume of the representative element shown in **Fig. 3.2** is d^3 [m^3], and the number of grains per unit volume should be d^{-3} [m^{-3}]. Finally, the rate of pressure dissolution is formulated by multiplying Eq. (3.22) by d^{-3}, as follows:

$$R^{PS} = \frac{3V_m k_+}{RTd}\left(\frac{\sigma_{VM}}{R_c} - \sigma_c\right). \tag{3.23}$$

As the pressure dissolution proceeds, contact-area ratio R_c increases and corresponding porosity ϕ decreases. Thus, the relation between R_c and ϕ should be obtained in order solve Eq. (3.23) with time.

Considering the geometrical scheme (see **Fig. 3.2**), solid volume V_s, in the representative elementary volume, is calculated by subtracting the sums of the volumes truncated between the contacts of two hemispheres from the volume of a sphere of diameter d, given as

$$V_s = \frac{1}{6}\pi h(3a^2 + \frac{3d^2}{4} + h_d^2), \tag{3.24}$$

where h_d [m] is one-half of the domain height and a [m] is the radius of the contact area. One-half of the domain height, h_d, is given as

$$h_d = \sqrt{\frac{d^2}{4} - a^2}\,. \tag{3.25}$$

The porosity, ϕ, is derived by subtracting solid volume V_s, divided by the total volume of the domain, V_t, from one, as follows:

$$\phi = 1 - \frac{V_s}{V_t} = 1 - \frac{\frac{1}{6}\pi\sqrt{\frac{d^2}{4} - a^2}(2a^2 + d^2)}{d^2\sqrt{\frac{d^2}{4} - a^2}} = 1 - \frac{\pi(2a^2 + d^2)}{6d^2}\,. \tag{3.26}$$

The radius of the contact area is expressed as

$$a^2 = \frac{d^2}{4} R_c\,. \tag{3.27}$$

By substituting Eq. (3.27) into Eq. (3.26), porosity ϕ is reformulated as

$$\phi = 1 - \frac{\pi\left(\frac{d^2}{2} R_c + d^2\right)}{6d^2} = 1 - \left\{\frac{\pi}{12}(R_c + 2)\right\}. \tag{3.28}$$

$$\Rightarrow R_c = \frac{12}{\pi}(1 - \phi) - 2\,. \tag{3.29}$$

Consequently, the rate of pressure dissolution is reformulated by substituting Eq. (3.29) into Eq. (3.23), as follows:

$$R^{PS} = \frac{3V_m k_+}{RTd}\left(\frac{\sigma_{VM}}{(12/\pi)(1-\phi) - 2} - \sigma_c\right). \tag{3.30}$$

In the previous numerical works, R^{PS} - the rate of pressure dissolution at the grain contacts - was not formulated well. Thus, the existing coupled models cannot describe the influence of the pressure dissolution on the changes in rock porosity/permeability and the other physical processes such as the changes in concentration of the chemical solutes. In this chapter, as described above, the rate of pressure dissolution is formulated theoretically and incorporated into the coupled model. This is one of the remarkable characteristics in comparison with other coupled models.

3.2.2 Modification of porosity and related permeability

In the present work, changes in porosity are only induced by the mineral reactions of the free-face dissolution/precipitation and the pressure dissolution. The rates for the changes in porosity due to the two mineral reactions are defined by

$$\dot{\phi}^{FF} = V_m R^{FF}, \tag{3.31}$$

$$\dot{\phi}^{PS} = -V_m R^{PS}, \tag{3.32}$$

where $\dot{\phi}^{FF}$ and $\dot{\phi}^{PS}$ [s^{-1}] are the rates of porosity change of the free-face dissolution/precipitation and the pressure dissolution, respectively. Thus, the porosity at an arbitrary time is obtained by using Eqs. (3.31) and (3.32), given as

$$\phi = \phi_i + \int \dot{\phi}^{FF} dt + \int \dot{\phi}^{PS} dt, \tag{3.33}$$

where ϕ_i [-] is the initial porosity. Once the porosity has been evaluated, the related permeability can also be evaluated by the Kozeny-Carman equation$^{3.31)}$, as follows:

$$k = k_i \frac{(1-\phi_i)^2}{(1-\phi)^2} \left(\frac{\phi}{\phi_i} \right)^3, \tag{3.34}$$

where k and k_i [m^2] are the permeability at an arbitrary time and the initial permeability, respectively.

3.3 Model verification

In the previous section, a coupled THMC model was proposed to simulate the changes in porosity/permeability in porous media. In order to validate the proposed model, the model predictions are compared with the measurements obtained from laboratory experiments performed by Elias and Hajash (1992)$^{24)}$. The compaction of quartz sand, with a mean grain diameter of 180-250 μm, has been conducted under the constant effective stresses of 69.0, 34.5, and 17.2 MPa at

150°C. The evolution of the porosity and that of the silica concentration in the pore fluid were measured over time to investigate the chemical and physical processes related to the pressure dissolution[3.24)]. In this section, both the reduction in porosity and the evolving silica concentration in the pore fluid were predicted. The parameters used in the simulations are summarized in **Table 3.2**.

Table 3.2 Calculation parameters to simulate experimental results.

Diameter d [μm]	Temperature T [°C]	Effective stress σ_{eff} [MPa]	Critical stress σ_c [MPa]	Equilibrium constant K_{eq} [mol m^{-3}]
215	150	69.0, 34.5, 17.2	73.2	1.79

Diffusion coefficient D_b [m^{2}s^{-1}]	Dissolution rate constant k_+ [mol m^{-2} s^{-1}]	Young's modulus E [GPa]	Poisson's ratio ν [-]
1.12×10^{-9}	2.51×10^{-9}	72.4	0.17

In the simulations, the calculation domain whose porosity initially starts with 0.35, equivalent to that of the experiments[3.24)], was set to be a square with side lengths of 0.01 m. The constant uniaxial confining pressures of 69.0, 34.5, and 17.2 MPa and the temperature of 150°C were applied as the boundary conditions and as the initial condition, respectively. The silica concentration within the domain was initially fixed at the equilibrium concentration of quartz at 150°C, which was calculated by Eq. (3.13). It was altered over time by considering the free-face dissolution/precipitation and/or the pressure dissolution of quartz. All the boundaries were assumed to be thermally and hydraulically outflow boundaries. The initial contact-area ratio, R_{c0}, was evaluated by assuming the Hertzian contacts[3.32),] given as

$$R_{c0} = \left(\frac{3\sigma_{eff}\pi(1-\nu^2)}{4E} \right)^{2/3}, \tag{3.35}$$

where σ_{eff} [Pa] is the effective stress (i.e., 69.0, 34.5, or 17.2 MPa), ν [-] is Poisson's ratio, and E [Pa] is Young's modulus. When the pressure dissolution proceeds, the contact-area ratio increases. The changes are obtained utilizing Eqs. (3.29), (3.31), and (3.32), as follows:

$$\begin{aligned} R_c &= R_{c0} + \int \dot{R}_c dt \\ &= R_{c0} - \frac{12}{\pi}\int \dot{\phi} dt \\ &= R_{c0} - \frac{12}{\pi}\int \left(\dot{\phi}^{FF} + \dot{\phi}^{PS} \right) dt \\ &= R_{c0} - \frac{12}{\pi}\left(\int V_m \cdot R^{FF} dt - \int V_m \cdot R^{PS} dt\right) \end{aligned} \tag{3.36}$$

After every time step, the new R_c was updated and used for calculating the rate of the pressure dissolution, R^{PS}, in the following time step. It should be noted that in these predictions for verification, R^{PS} was calculated over time with Eq. (3.23) instead of Eq. (3.30) because R_c can be calculated directly with Eq. (3.36). It should also be noted that the specific surface area in Eq. (3.11) cannot be obtained from the literature[3.24)]. Thus, by introducing roughness factor f_r [3.33)], which is the ratio of the true (microscopic) surface area over the apparent (geometric) surface area, the model predictions were performed. The relation between specific surface area A and roughness factor f_r is expressed as follows:

$$A = f_r A_{geo}, \tag{3.37}$$

where A_{geo} [m^2 m^{-3}] is the geometric specific surface area, which is simply evaluated by the ratio of the surface area of the spherical grain of diameter d over the volume, as

$$A_{geo} = \frac{\pi d^2}{\frac{\pi d^3}{6}} = \frac{6}{d}. \tag{3.38}$$

In the model predictions, three roughness factors, namely, 10, 20, and 80, were applied. The values are equivalent to the magnitude indicated by Anbeek (1992)[3.34)], who concluded that it fell in the range of 2.5 to 11 for freshly created surfaces, and Sverdrup (1990)$^{3.35)}$, who showed that it varied between 1.5 and 71 for 28 silicate minerals.

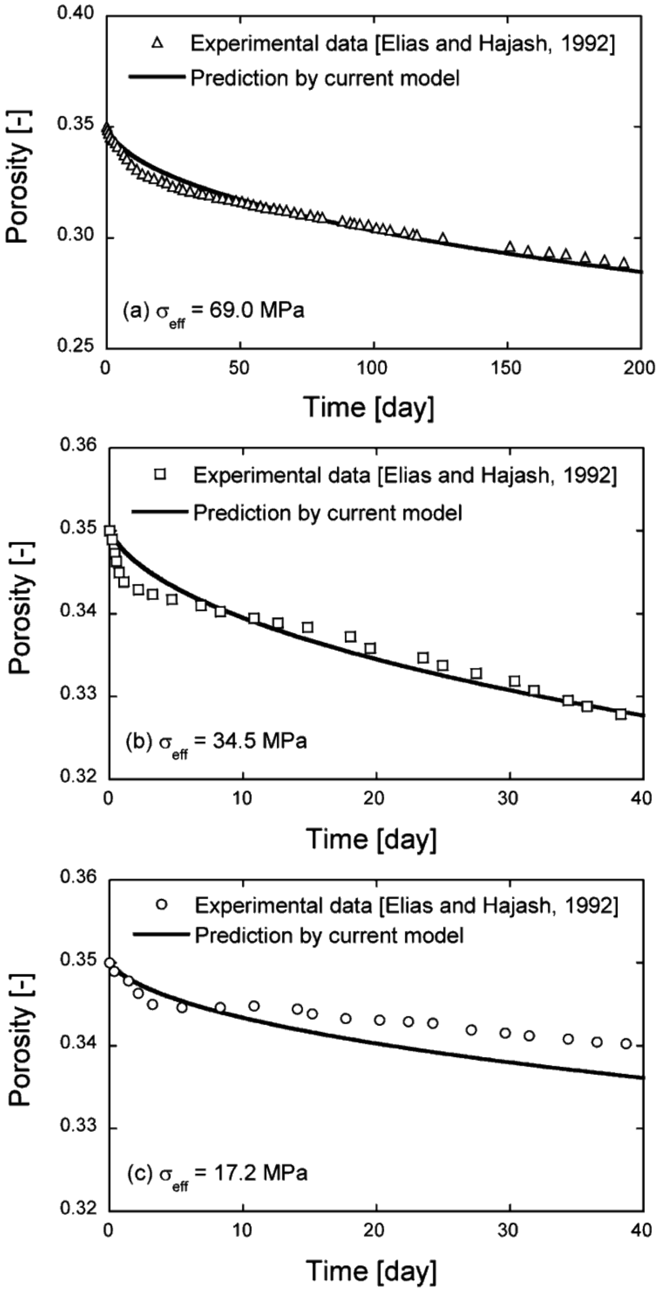

Fig. 3.3 Comparison of porosity reduction with time between experimental data$^{3.24)}$ and predictions by the model.

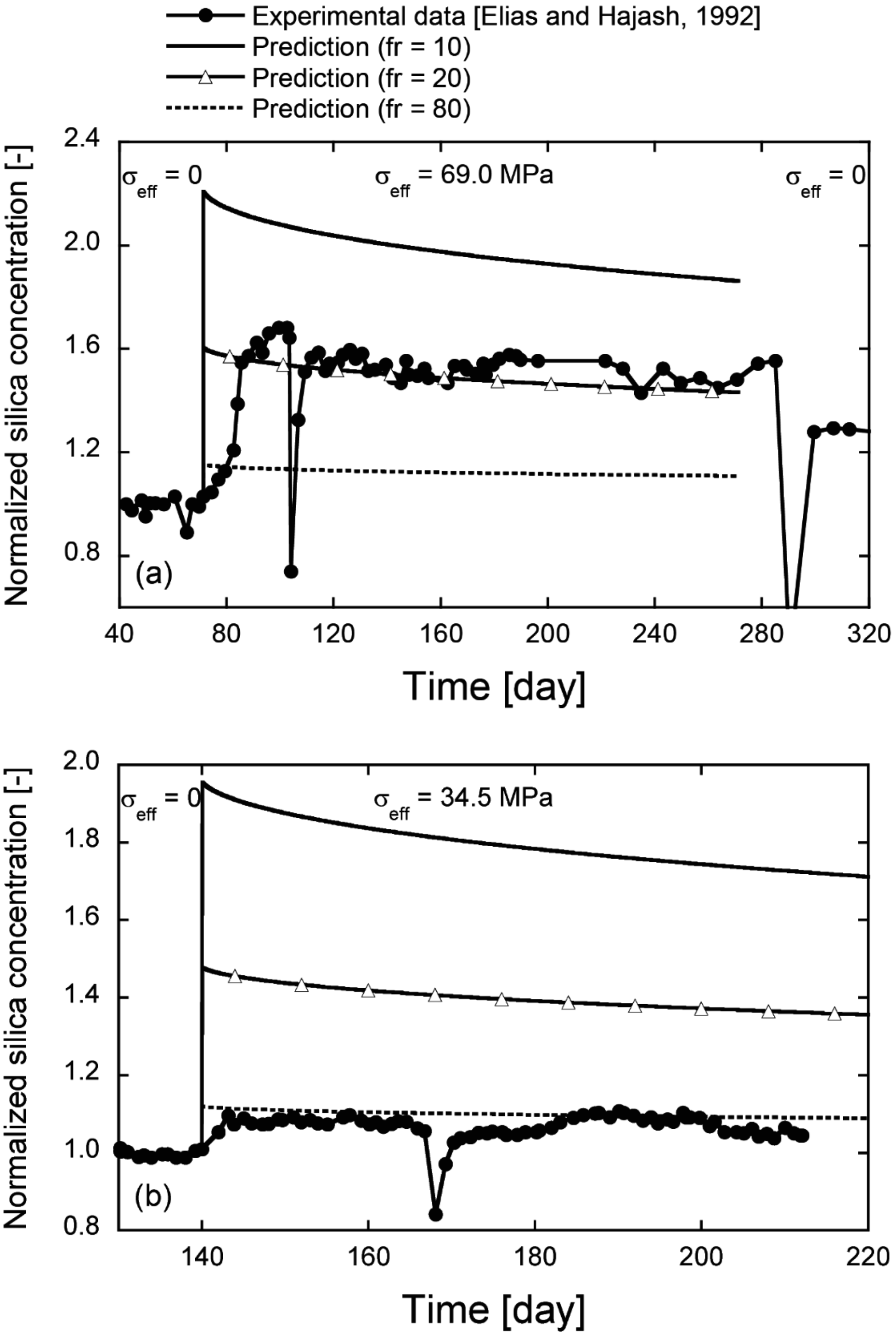

Fig. 3.4 Comparison of silica concentration in pore fluid between experimental data[3.24)] and predictions by the model.

Predictions of the evolution of the porosity and that of the silica concentration, normalized by the initial values, are shown in **Figs. 3.3** and **3.4**, respectively, together with the data obtained from the experiments. As is apparent from **Fig. 3.3**, all the predicted porosity reductions with time are in excellent agreement with the experimental measurements. It is noted that changing the roughness factor has little influence on the changes in porosity; and therefore, the predicted results with different roughness factors are not shown in **Fig. 3.3**. In contrast, the predicted silica concentration is apparently dependent on which roughness factor is applied (**Fig. 3.4**). The utilization of higher roughness factors induces the prediction of lower silica concentrations. The system in the pore fluid is always oversaturated with silica because it is initially equivalent to the equilibrium concentration, and the additional solute is supplied from the grain contacts due to the pressure dissolution. Therefore, the rates of precipitation increase with the higher roughness factors, resulting in the lower silica concentrations. The predictions express some variations because of the different roughness factors, but they replicate the tendency confirmed in the experiments well (i.e., the abrupt increase after applying pressure and the gradual decrease with time). Overall, a comparison of the porosity reduction and the evolving silica concentration between the predictions and the experimental measurements implies the validity of the proposed model for estimating the long-term evolution of the porosity/permeability in porous media via the free-face dissolution/precipitation and the pressure dissolution that depend on the applied pressure, temperature, and flow conditions.

3.4 Long-term predictions of permeability

The developed model was utilized to predict the long-term changes in permeability in sedimentary rock near high-level radioactive waste within a simulated disposal facility. It should be noted that although actual data from related literature were utilized in the following predictions, no specific sites for geological disposal of high-level radioactive waste are anticipated.

3.4.1 Modeling conditions

The calculation domain, with a rock density of 2100 kg/m^3, was set to be a rectangle with vertical and horizontal lengths of 700 and 12.2 m, respectively. The canisters containing the radioactive waste were virtually installed as a heat source by setting them laterally at a depth of 450 m[3.36)]. The horizontal length of 12.2 m was chosen for the domain so that it would be one-half of the center-to-center spacing of each cavity, of the diameter 2.22 m[3.36)], as shown in **Fig. 3.5**. The rock for the simulations was assumed to have been fully-saturated with groundwater and to have been composed purely of quartz, with the initial porosity of 0.40[3.37)]. The thermal and hydraulic gradients were set to be 5°C/100 m and 1/1000, respectively[3.38)]. The surface temperature was fixed at 15°C. The initial silica concentration within the domain was set to be the equilibrium value, which was evaluated by Eq. (3.13). The change in pH was not taken into account and the initial value was set at pH = 7. The influence of the pre-existing fracture network in the rock was not considered.

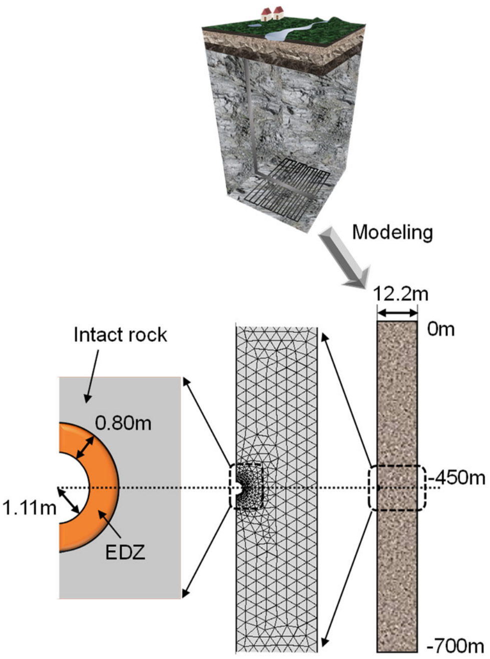

Fig. 3.5 Calculation domain. The calculation domain is a rectangle with vertical and horizontal lengths of 700 and 12.2 m, respectively. The cavity, with a diameter of 2.22 m, is excavated by lateral setting at a depth of 450 m. The EDZ ranges in the radial direction from the cavity wall to 0.8 m.

In the simulations, the Excavation Damaged Zone (EDZ) was modeled explicitly with regard to the rock permeability. The scientific and technical report, summarizing the HLW disposal construction in Japan[3.39)], shows that the EDZ in both sedimentary and crystalline rocks may range, in the radial direction, from the periphery of the excavated cavity to roughly 1 m. Thus, the range from the periphery to 0.8 m was modeled as the EDZ in the simulations (**Fig. 3.5**). The permeability within the EDZ was increased to two orders of magnitude greater than the intact rock[3.36),3.40)]. The thermal and mechanical properties in the EDZ were assumed to be equivalent to those of the intact rock, because those in the EDZ were ill-defined, and investigating the evolution of permeability due to the mineral reactions is the most important task in this chapter. In actual calculations, the changes in the von Mises stresses, due to the excavation, were evaluated by performing a self-weight analysis (**Fig. 3.6**). As is obvious from **Fig. 3.6**, the evolved von Mises stresses, greater around the periphery of the cavity, are the driving-force in the pressure dissolution (see Eq. (3.30)).

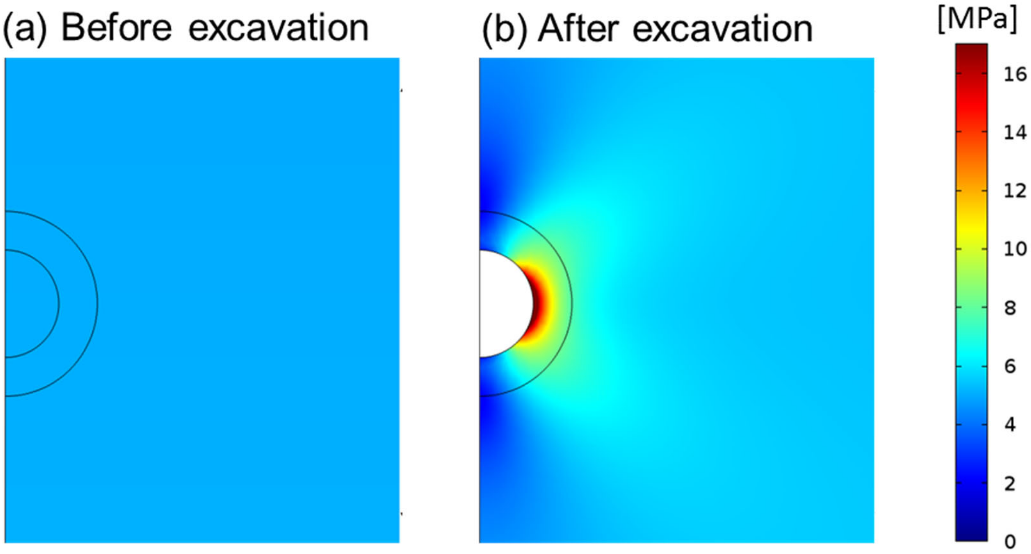

Fig. 3.6 Distribution of von Mises stress before and after cavity excavation.

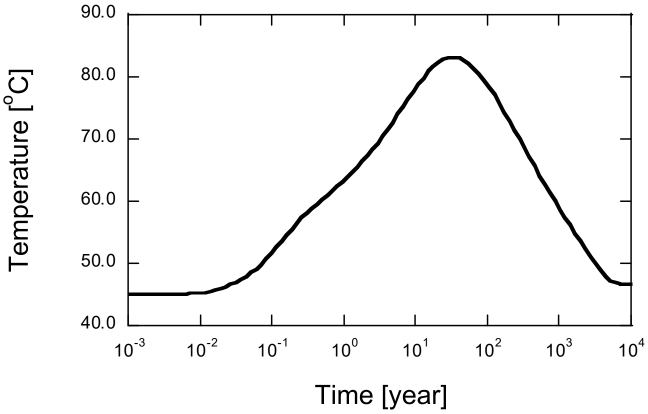

Fig. 3.7 Temperature change with time that is used as the boundary condition applied on the periphery of the cavity[3.39)].

Considering the heat source from the radioactive waste, the changes in temperature with time outside the buffer material can be obtained from the literature[3.39)], as shown in **Fig. 3.7**. In the simulations, the changes in temperature were applied at the periphery of the cavity as boundary conditions. The prediction period was set at 10^4 years after the excavation. In the calculation of the heat transfer, the following Neumann boundary condition is set at all the boundaries excluding the periphery of the cavity:

$$\frac{\partial T}{\partial \boldsymbol{n}} = 0\,, \tag{3.39}$$

where ***n*** represents the outward direction normal to targeted boundary. In the calculation of the reactive transport, the following Neumann boundary condition is set at all the boundaries of the calculation domain:

$$\frac{\partial c_i}{\partial \boldsymbol{n}} = 0\,. \tag{3.40}$$

The parameters used in the calculations are summarized in **Table 3.3**.

Table 3.3 Calculation parameters to simulate long-term permeability.

Rock type	Initial permeability k_i [m^2]	Young's modulus E [GPa]	Poisson's ratio ν [-]	Initial porosity ϕ_i [-]	Thermal conductivity λ_m [W m^{-1} K^{-1}]	Heat capacity C_p [J kg^{-1} K^{-1}]
EDZ	1.0×10^{-13}	2.5	0.30	0.40	1.60	1500
Intact	1.0×10^{-15}	2.5	0.30	0.40	1.60	1500

3.4.2 Prediction results

In this section, the predictions were performed for two different cases in order to investigate the influence of the pressure dissolution on the changes in permeability with time. One was conducted by considering the full processes and the other was conducted by excluding only the pressure dissolution. Hereinafter, the former and the latter cases are called the "PS" and the "no-PS" conditions. Calculations for the no-PS condition were conducted by merely making R^{PS} in Eq. (3.30) zero at all the calculation steps. The changes in the temperature distribution with time, predicted under the PS condition, are shown in **Fig. 3.8**.

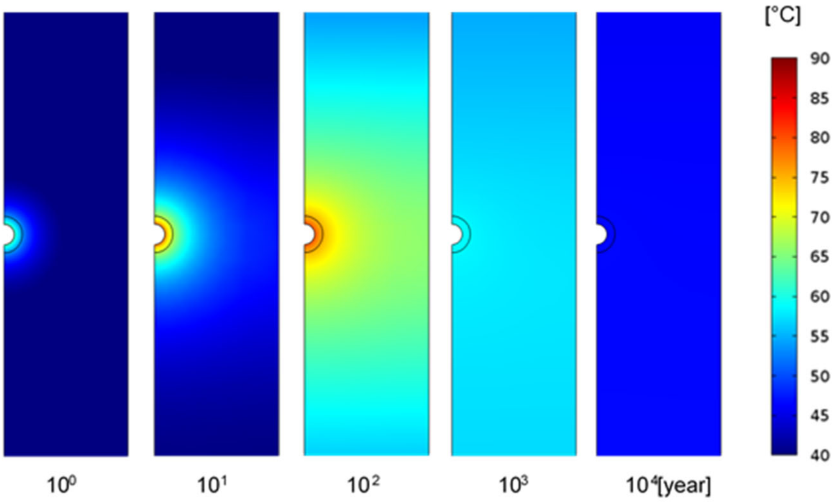

Fig. 3.8 Change in temperature distribution with time in the range of 10^0 to 10^4 years under the PS condition.

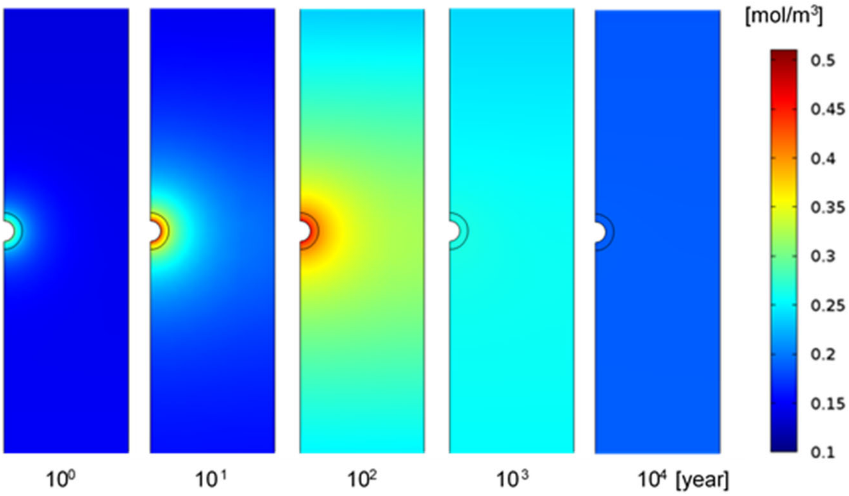

Fig. 3.9 Change in Si concentration distribution with time in the range of 10^0 to 10^4 years under the PS condition.

The temperature in the EDZ increases with time; it increases to more than 80°C between 10^1 and 10^2 years. Then, it decreases with time and reaches a steady temperature (i.e., ~45°C) after 10^4 years. This tendency is quite similar to the evolution of the distribution of the Si concentration with time (**Fig. 3.9**), which is reasonable. As the equilibrium concentration of Si only depends on the induced temperature, the changes over time should be similar. The predicted changes in both temperature and the Si concentration with time, under the no-PS condition, imply no significant difference from those under the PS condition. This is because the concentrations in the whole system approach the equilibrium values in a relatively short period via the precipitation occurring at the free face, when additional solute is supplied in the pore water due to the pressure dissolution, and through the free-face dissolution, when the system temperature and the related equilibrium concentration increase. Therefore, the Si concentrations are equivalent to the equilibrium values throughout most of the calculation period.

The changes in permeability with time under the no-PS and the PS conditions are compared in **Figs. 3.10** and **3.11**, respectively. The permeability is normalized by the initial value. As is clearly seen in the figures, there is little change in permeability with time under the no-PS condition, while the permeability decreases with time and this decrease can be observed after 10^2 years under the PS condition. In particular, the decrease is significant within the EDZ. This is because the pressure dissolution, resulting in a decrease in porosity, is activated by the increase in the von Mises stress by the cavity excavation (see **Fig. 3.6**), and an additional decrease in porosity is caused by the precipitation in the free face induced by the supply of dissolved silica due to the pressure dissolution.

In order to further examine the effect of the pressure dissolution on the changes in permeability within the EDZ, the changes with time at four specific locations, depicted in **Fig. 3.12**, are shown in **Fig. 3.13**. Three of the four points are located within the EDZ, and the fourth one is 4.99 m away from the boundary of the cavity. No change in permeability is confirmed under the no-PS condition. Actually, the free-face precipitation of the secondary minerals, driven by the dissolution of the cement materials, may result in changes in the porosity/permeability, but this is not the case in the present work. On the other hand, the permeability at No. 1 decreases by one order of magnitude in 10^4 years. However, the decrease is locally limited and is not observed at No. 4, which is located at a point one-fourth of the distance from the center-to-center spacing of each cavity (**Fig. 3.13**). In the current predictions, the decrease in permeability was observed only under the PS condition. This should cause the delay of the transportation of radioactive nuclides, and the effect needs to be investigated quantitatively.

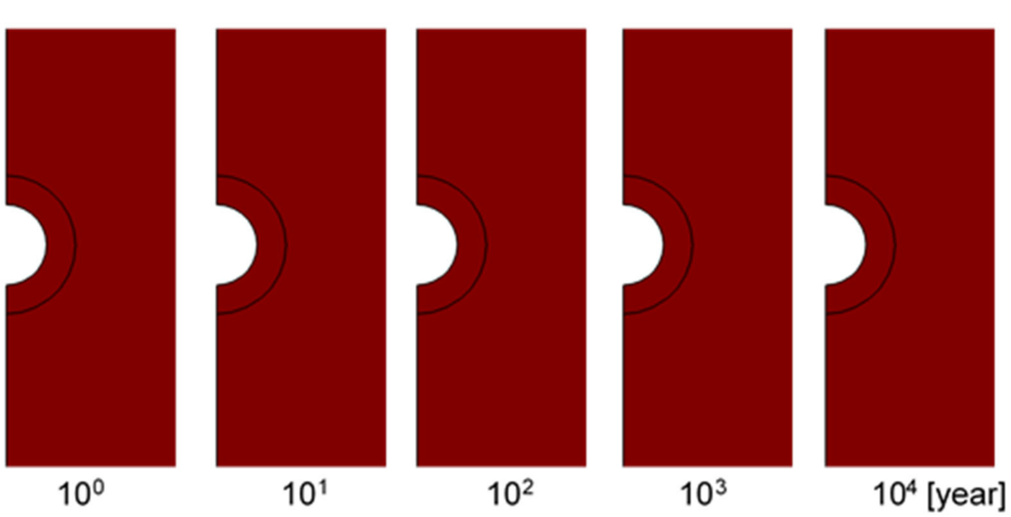

Fig. 3.10 Changes in normalized permeability with time in the range of 10^0 to 10^4 years under the no-PS condition. No permeability change is confirmed.

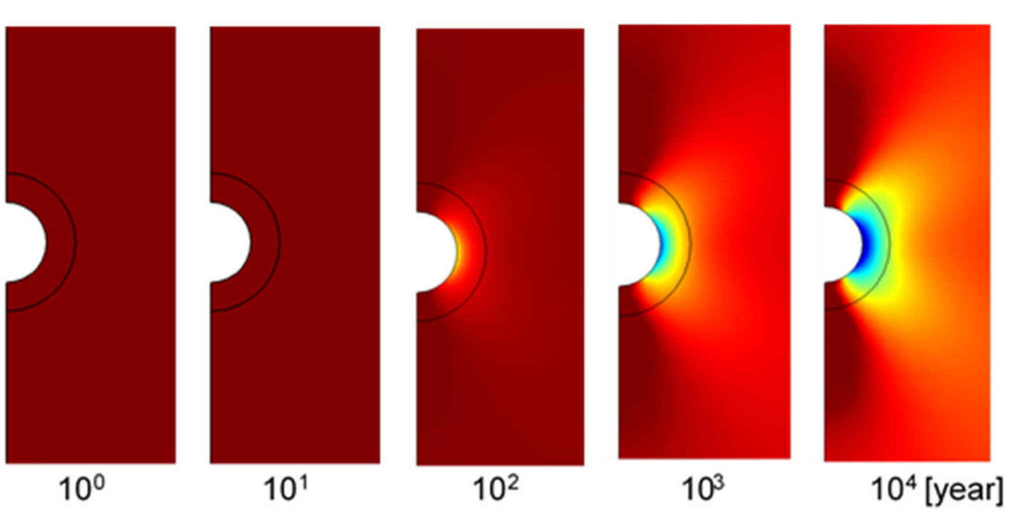

Fig. 3.11 Changes in normalized permeability with time in the range of 10^0 to 10^4 years under the PS condition. The permeability decreases with time. The reduction is especially significant around the periphery of the cavity.

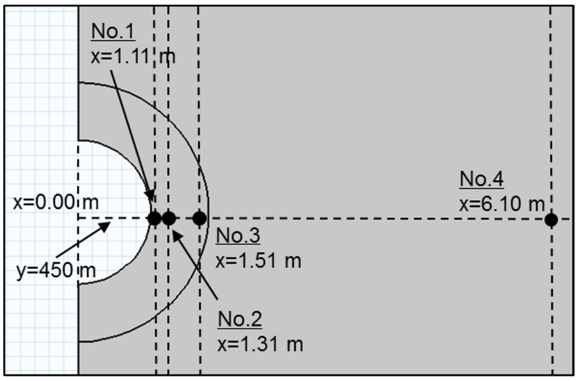

Fig. 3.12 Specific locations where changes in permeability with time are observed.

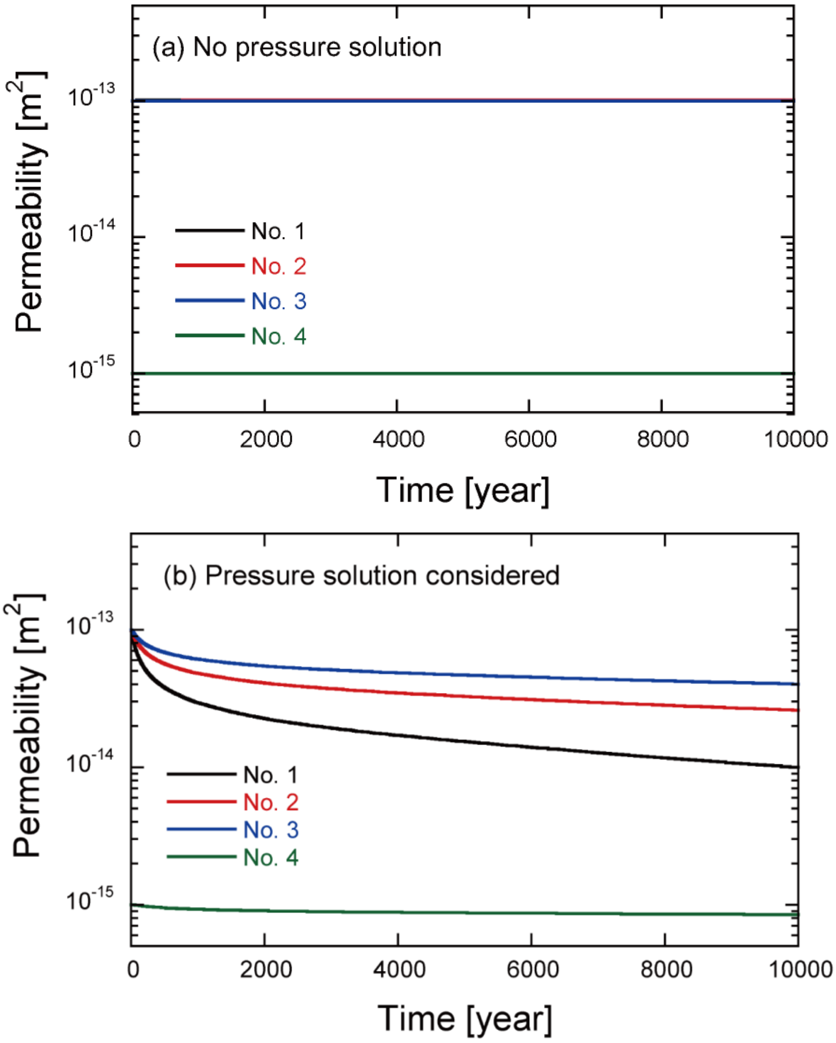

Fig. 3.13 Permeability changes with time at specific locations indicated in **Fig. 3.12**: (a) the no PS condition and (b) the PS condition.

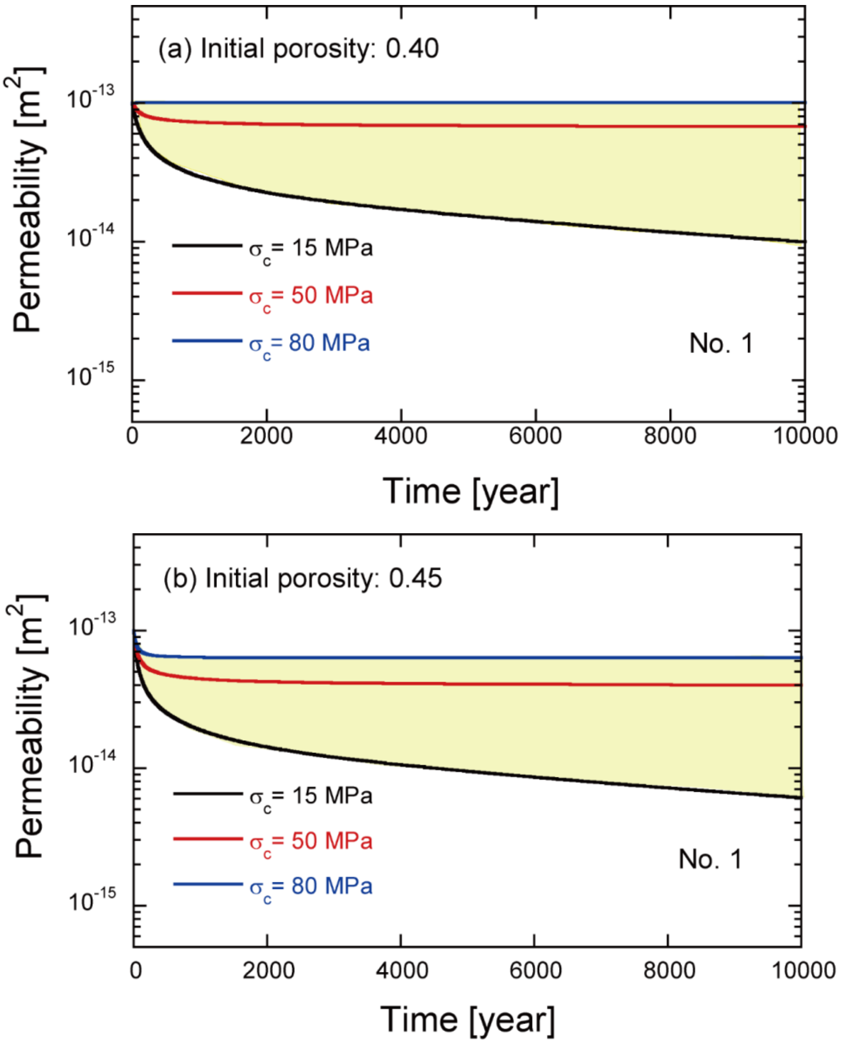

Fig. 3.14 Permeability changes with time under the PS condition at No. 1, indicated in **Fig. 3.12**: (a) initial porosity of 0.40 and (b) 0.45.

As a parametric study, predictions are performed by changing the parameters of initial porosity ϕ_i and critical stress σ_c, which should control the rate of the pressure dissolution (see Eq. (3.30)), to investigate the influence on the evolution of the permeability. Two different initial porosities, 0.40 and 0.45, are chosen to simulate Horonobe mudstone in Japan[3.37)], and three critical stresses, 15, 50, and 80 MPa, are set for the calculations. The change in permeability observed at point No. 1, shown in **Fig. 3.12**, is depicted in **Fig. 3.14**. It is apparent that when a higher critical stress is applied, a lesser change in permeability is confirmed. This is because the influence of the pressure dissolution becomes smaller when the difference between the von Mises stress and the critical stress is smaller, as is clear from Eq. (3.30). Specifically, at 80 MPa, the permeability hardly changes in the case of ϕ_i = 0.40, and it decreases roughly 30% for 10^4 years in the case of ϕ_i = 0.45. From the above calculated results, it is seen that selecting appropriate values for the critical stress is of significant importance to achieving accurate predictions.

3.5 Summary

In this chapter, a coupled THMC model was developed to predict the long-term evolution of the permeability in sedimentary rock. The model calculates the heat transfer, the groundwater flow, the variation in induced stresses, and the mineral reactions (i.e., the free-face dissolution/precipitation and the pressure dissolution), and their interactions. The changes in porosity and silica concentration in the quartz aggregates were investigated to confirm the verification of the developed model in reproducing the experimentally observed behavior3.24). The predictions closely matched the experimental measurements. Then, the validated model was applied to investigate the influence of the pressure dissolution on the change in permeability of the sedimentary rock near the high-level radioactive waste in a geological disposal facility, in assuming the expected temperature, stress, and flow conditions. The predictions under assumed conditions implied that the process of the pressure dissolution reduced the rock permeability especially close to the excavated cavity to one order of magnitude less than the initial value, which should delay the transportation of radioactive nuclides.

The developed model is straightforward and relatively simple because some interactions among the THMC processes are omitted. Thus, the current model should be updated by taking into account the omitted processes among the THMC interactions (e.g., the hydraulic-mechanical interactions; see **Fig. 3.1**) in order to describe the coupled THMC phenomena more precisely.

References

3.1) Tsang, CF., ed.: Coupled Processes Associated with Nuclear Waste Repositories. Elsevier Inc.; ISBN 9780323142403; 2012.

3.2) Tsang, Y.: Effects of coupled processes on a proposed high-level radioactive waste repository at Yucca Mountain, Nevada. Geological Society of America Memoirs, 2012; 209: 363-93.

3.3) Zheng, L., Samper, J.: A coupled THMC model of FEBEX mock-up test. Phys. Chem. Earth., 2008; 33: S486–98.

3.4) Taron, J., Elsworth, D. and Min, K.-B.: Numerical simulation of thermal-hydrologic-mechanical-chemical processes in deformable, fractured porous media. Int. J. Rock Mech. Min. Sci., 2009; 46:842-54.

3.5) Nasir, O., Fall, M. and Evgin, E.: A simulator for modeling of porosity and permeability changes in near field sedimentary host rocks for nuclear waste under climate change influences. Tunnelling Underground Space Technology, 2014; 42:122-35.

3.6) Kim, J., Sonnenthal, E. and Rutqvist, J.: A sequential implicit algorithm of chemo-thermo-poro-mechanics for fractured geothermal reservoirs. Comput. Geotech., 2015; 76:59-71.

3.7) Lang, PS., Paluszny, A. and Zimmerman, RW.: Hydraulic sealing due to pressure solution contact zone growth in siliciclastic rock fractures. J. Geophys. Res., 2015; 120:4080–4101, doi:10.1002/2015JB011968.

3.8) McDermott, C., Bond, A., Harris, AF., Chittenden, N. and Thatcher, K.: Application of hybrid numerical and analytical solutions for the simulation of coupled thermal, hydraulic, mechanical and chemical processes during fluid flow through a fractured rock. Environ. Earth. Sci., 2015; DOI 10.1007/s12665-015-4422-7.

3.9) Taron, J. and Elsworth, D.: Coupled mechanical and chemical processes in engineered geothermal reservoirs with dynamic permeability. Int. J. Rock Mech. Min. Sci., 2010; 47:1339-48.

3.10) Lasaga, AC.: Chemical Kinetics of Water-Rock Interactions. J. Geophys. Res., 1984; 89: 4009-25.

3.11) Croizé, D., Renard, F., Bjørlykke, K. and Dysth,e DK.: Experimental calcite dissolution under stress: evolution of grain contact microstructure during pressure solution creep. J. Geophys. Res., 2010; 115, B09207, doi:10.1029/2010JB000869.

3.12) Neveux, L., Grgic, D., Carpentier, C., Pironon, J., Truche, L. and Girard, JP.: Experimental simulation of chemomechanical processes during deep burial diagenesis of carbonate rocks. J. Geophys. Res., 2014; 119, 984.1007, doi:10.1002/2013JB010516.

3.13) Raj, R.: Creep in polycrystalline aggregates by matter transport though a liquid phase. J. Geophys. Res., 1982; 87:4731-39.

3.14) Robin, P-YF.: Pressure solution at grain to grain contacts. Geochim. Cosmochim. Acta., 1978; 42:1383-89.

3.15) Spiers, CJ, De-Meer, S., Niemeijer, A.R. and Zhang, X.: Kinetics of Rock Deformation by Pressure Solution and the Role of Thin Aqueous Films. In: Frontiers Science Series, 2003:129e158.

3.16) Weyl, PK.: Pressure solution and force of crystallization-A phenomenological theory. J. Geophys. Res., 1959; 64: 2001-25.

3.17) Zhang, X., Spiers, C.J. and Peach, C.J.: Compaction creep of wet granular calcite by pressure solution at 28°C to 150°C. J. Geophys. Res., 2010; 115 (B9):B09217.

3.18) Zubtsov, S., Renard, F., Gratier, J.P., Guiguet, R., Dysthe, D.K. and Traskine, V.: Experimental pressure solution compaction of synthetic halite/calcite aggregates. Tectonophysics, 2004; 385: 45-57.

3.19) Yasuhara, H., Elsworth, D. and Polak, A.: A mechanistic model for compaction of granular aggregates moderated by pressure solution. J. Geophys. Res., 2003; 108(11):2530, doi:10.1029/2003JB002536.

3.20) Yasuhara, H., Elsworth, D. and Polak, A.: Evolution of permeability in a natural fracture: The significant role of pressure solution. J. Geophys. Res., 2004; 109(B3):B03204, doi:10.1029/2003JB002663.

3.21) Yasuhara, H., Elsworth, D., Polak, A., Liu, J., Grader, A. and Halleck, P.: Spontaneous Permeability Switching in Fractures in Carbonate: Lumped Parameter Representation of Mechanically- and Chemically-Mediated Dissolution. Transp. Porous Media, 2006; 65:385-409.

3.22) Yasuhara, H. and Elsworth, D.: Compaction of a rock fracture moderated by competing roles of stress corrosion and pressure solution. Pure Appl. Geophys., 2008; 165:1289-306.

3.23) Yasuhara, H., Kinoshita, N., Ohfuji, H., Lee, DS., Nakashima, S. and Kishida, K.: Temporal alteration of fracture permeability in granite under hydrothermal conditions and its interpretation by coupled chemo-mechanical model. Appl. Geochem., 2011; 26:2074-88.

3.24) Elias, BP. and Hajash, A.: Change in quartz solubility and porosity change due to effective stress: An experimental investigation of pressure solution. Geology, 1992; 20:451-54.

3.25) COMSOL2014：COMSOL MULTIPHYSICS. Version 5.0, Available from www.comsol.com.

3.26) Revil, A.: Pervasive pressure-solution transfer: a poro-visco-plastic model. Geophys. Res. Lett., 1999; 26:255-58.

3.27) Parkhurst, DL. and Appelo, CAJ.: Description of Input and Examples for PHREEQC Version3-A Computer Program for Speciation, Batch-Reaction, One-Dimensional Transport, and Inverse Geochemical Calculations, Online version availableromhttp://wwwbrr.cr.usgs.gov/projects/GWC_coupled/phreeqc/phreeqc3-html/phreeq-c3.htm.

3.28) Rimstidt, JD. and Barnes, HL.: The kinetics of silica-water reactions. Geochim. Cosmochim. Acta., 1980; 44:1683-99.

3.29) Heidug, WK.: Intergranular solid-fluid phase transformations under stress: The effect of surface forces. J. Geophys. Res., 1995; 100:5931-40.

3.30) Stephenson, LP., Plumley, WJ. and Palciauskas, VV.: A model for sandstone compaction by grain interpenetration. J. Sediment Petrol., 1992; 62:11-22.

3.31) Bear, J.: Dynamics of Fluids in Porous Media. Dover Publications Inc.; 1972.

3.32) Hertz, H.: Ueber die Berührung fester elastischer Körper. J. Math. (Crelle's J.) 1881; 92:156-71.

3.33) Murphy, WM. and Helgeson, HC.: Thermodynamic and kinetic constraints on reaction rates among minerals and aqueous solutions. IV. Retrieval of rate constants and activation parameters for the hydrolysis of pyroxene, wollastonite, olivine, andalusite, quartz, and nepheline. Am. J. Sci., 1989; 289:17-101.

3.34) Anbeek, C.: Surface roughness of minerals and implications for dissolution studies. Geochim. Cosmochim.

Acta., 1992; 56:1461-69.

3.35) Sverdrup, H.: The Kinetics of Base Cation Release Due to Chemical Weathering. Lund University Press, Lund, Sweden; 1990.

3.36) Suzuki, H., Nakama, S., Fujita, T., Imai, H. and Sazarshi, M.: A long-term THMC assessment on the geochemical behavior of the bentonite buffer. J. Nucl. Fuel Cycle Environ., 2012; 19:39-50.

3.37) Miyazawa, D., Sanada, H., Kiyama, T., Sugita, Y. and Ishijima, Y.: Poroelastic coefficients for siliceous rocks distributed in the Horonobe area, Hokkaido, Japan. J. MMIJ, 2011; 127:132-38.

3.38) JNC (Japan Nuclear Cycle Development Institute), 2005: Development and management of the technical knowledge base for the geological disposal of HLW, Summary of the H17 project reports, Vol. 1. Scientific research of deep underground. JNC TN1400 2005-014.

3.39) Japan Nuclear Cycle Development Institute, 2000: Second Progress Report on Research and Development for the Geological Disposal of HLW in Japan, Supporting Report 2 Repository Design and Engineering Technology, H12: Project to Establish the Scientific and Technical Basis for HLW Disposal in Japan. JNC TN1410 2000-003, IV-139-IV-160.

3.40) Minato, K., ed.: JAEA R&D review 2013; ISSN 2188-1456.

Chapter 4

Multi-Physics Simulations for Predicting the Evolution of Permeability and Reactive Transport Behavior within Rock Fractures

4.1 Overview

A coupled THMC model was proposed in **Chapter 3** to predict the evolution of permeability within the rock matrix. Subsequently, this chapter introduces a coupled THMC model that simulates the evolution of permeability and the reactive transport behavior within rock fractures.

In the deep subsurface, the fluid flow behavior often depends on the hydraulic properties of the rock fractures (i.e., permeability and aperture) and the spatial distribution of the fracture network. It is well known that the permeability of fractured rock is influenced by the coupled thermal-hydraulic-mechanical-chemical (THMC) processes under the deep geological conditions4.1)~4.3). Among these several processes, mechanical-chemical (MC) processes, such as stress corrosion and the mineral reactions between the rock minerals and the pore water, may exert a non-negligible influence on the evolution of fracture permeability4.4)~4.6). However, within the context of the geological disposal of high-level radioactive waste, mineral reactions, such as free-face dissolution/precipitation4.7) and pressure dissolution4.8)~4.16), have been well recognized as important physical phenomena which may change the fracture permeability within a longer timescale in comparison to the mechanical processes. These processes within rock fractures have often been investigated under hydrothermal conditions where the fluid-rock reaction is enhanced.

Robert et al. [4.17)] conducted flow-through column-like experiments for 20 and 40 days using granite samples with a single tensile fracture by simulating a near-field setting of the shallow Enhanced Geothermal System (EGS) (i.e., temperature of 120°C and effective stress of 25-35 MPa), and the fracture permeability, the fracture aperture, and the mass of the dissolved minerals were computed through pore-pressure observations, effluent chemistry, and X-ray CT scan imaging. The results of the experiments showed a decrease in permeability that should have been due to a combination of the dissolution of the fracture propping asperities and mechanical creep. However, through measurements of the effluent solution, it was finally concluded that the decrease in permeability was actually due to the mineral dissolution of the fracture propping asperities rather than the mechanical effects. Beeler et al.[4.18)] measured the time-dependent closure of fractures in quartz at temperatures of 22-530°C and water pressures of 0.1 - 150 MPa, and reported a reduction in aperture of as much as 80% in just a few hours due to a pressure dissolution-like process. Besides these observations, many other experimental studies[4.4)~4.6),4.19),4.20)] have confirmed a reduction in the permeability of rock fractures by several orders of magnitude that was most likely brought about by the pressure dissolution.

Therefore, in order to predict the changes in permeability of fractured rock in actual fields, it should be of great importance to model the coupled THMC processes including the pressure dissolution. Conceptual models have been proposed in previous studies[4.4)~4.6),4.11),4.13),4.19)] to predict the evolution of the permeability of porous and fractured rocks due to a mechanical-chemical phenomenon (i.e., pressure dissolution). These models can only describe the mechanical-chemical processes in the representative elementary scale; and thus, coupled THMC numerical simulations cannot be conducted with them at the field scale. The aim of this chapter is to propose an FE model that can describe the coupled THMC processes including the pressure dissolution for predicting the changes in rock permeability in the field scale. Previously, a coupled THMC model using the FE scheme and incorporating the pressure dissolution at the grain-to-grain contacts[4.21)] (described in **Chapter 3)** was proposed. Updating the model by incorporating the process of pressure dissolution at the contacting asperities is the main purpose of this chapter.

Recent studies[4.20),4.22)~4.29)] also have proposed several coupled THMC numerical models, including the mineral reactions (i.e., free-face dissolution and pressure dissolution) within rock fractures to estimate the evolution of fracture permeability. For instance, Lang et al.[4.22)]developed a discrete multi-physics pore-scale model by extending the direct and coupled thermo-hydro-mechanical-chemical simulation approach of Bernabe et al.[4.23)] from single, axisymmetric grain contacts to three-dimensional models of randomly rough, self-affine surfaces. The model can estimate the changes in fracture aperture induced by pressure dissolution and elastic compression. However, the focus of most of those studies[4.22)~4.26)] was only the development of theoretical THMC models; the studies did not verify the developed models by comparing the predictions with actual measurements obtained from experiments.

In contrast, several studies[4.20),4.27)~4.29)] have developed coupled models and examined their validity by a comparison with experimental data. Yasuhara et al.[4.20)] developed a numerical model using the Lagrangian-Eulerian method that can predict the evolution of permeability and the reactive transport behavior within a single novaculite fracture by describing the mineral reactions (i.e., free-face dissolution and pressure dissolution). Their model applied additional multipliers in the calculations of the mechanical-chemical processes in order to follow the experimental measurements – the multipliers ranged from 30 to 10^6. Based on the works by Yasuhara et al.[4.6),4.20)], in Task C1 of the Decovalex project, an attempt has been made to develop THMC numerical models that can reproduce the experimental measurements of single rock fractures using novaculite and granite[4.27)~4.29)]. In the scheme of their modeling, Bond et al.[4.28),4.29)] applied some different modeling approaches, including the discretized 2D model that represents a 2D fracture surface taking the fracture topography data to locally define the fracture aperture, the homogenized (0D/1D/2D) model that treats the entire fracture surface as a single entity, and the synthetic model that uses the fracture topography data to define the statistics of the fracture aperture distribution. In their works[4.28),4.29)], several participating teams attempted to apply these different modeling approaches with each team conducting calculations using their own numerical code. Most of different numerical models developed in their works[4.28),4.29)] were able to replicate the experimental measurements relatively well (i.e., the evolution of fracture permeability and element concentrations), but in almost all cases, the prediction results were adjusted by incorporating fitting parameters, called enhancement factors and scaling factors, into the calculations of the mechanical-chemical processes with fitting parameters in the range of 245 to 10^6 [4.27)~4.29)].

In this chapter, a new coupled THMC model incorporating the pressure dissolution at the contacting asperities of rock fractures was developed using an FE scheme in order to predict the changes in permeability of rock fractures. As mentioned above, almost none of the other coupled THMC models[4.22)~4.26)], considering the pressure dissolution within rock fractures, have been validated and several coupled THMC models[4.20),4.27~4.29)] need calibrations of fitting parameters in wide ranges of 30 to 10^6 [4.20)] and 245 to 10^6 [4.27)~4.29)] in the calculation of the mechanical-chemical processes in order to follow the experiments. This may not be the case for the model developed in this chapter– minimizing the use and the values of unknown fitting parameters was a significant target for the model development. As is obvious, in order to examine the validity of the developed model, predictions made with the model were compared with the experimental measurements obtained from flow-through experiments[4.6)] using granite and mudstone samples.

4.2 Model description

4.2.1 Constitutive equations

The coupled THMC model developed in this chapter is based on a finite element scheme that can describe the interactions of multi-physics that include the heat transfer, the fluid flow, geomechanics, and the reactive transport with the mineral reactions of mineral dissolution/precipitation. By solving these THMC coupled processes, this model can evaluate the evolution of permeability in rock fractures. The equations for the model are presented in this section. The fluid flow in the fractures of saturated rock is simply modeled by the conservation of water mass and by assuming the Darcian flow, as follows:

$$\frac{\partial(\rho_w\phi)}{\partial t}+\nabla\cdot(\rho_w\boldsymbol{u})=f_m, \tag{4.1}$$

$$\boldsymbol{u}=-\frac{\boldsymbol{k}}{\mu}(\nabla p+\rho_w g\nabla h), \tag{4.2}$$

$$k=\frac{b_h^2}{12}, \tag{4.3}$$

where ρ_w [kg m^{-3}] is the density of the fluid, ϕ [-] is the porosity, $\boldsymbol{u}$ [m s^{-1}] is the fluid velocity tensor, f_m [kg m^{-3} s^{-1}] is the source term for the flow, $\boldsymbol{k}$ [m^2] is the rock permeability tensor, μ [Pa s] is the fluid dynamic viscosity, p [Pa] is the pore pressure, g [m s^{-2}] is the gravity acceleration, h [m] is the potential head, and b_h [m] is the hydraulic fracture aperture.

In the thermal process, the temperature of the rock is calculated by the heat transfer equation.

$$(\rho C_p)_{eq}\frac{\partial T}{\partial t}+\rho_w C_{p,w}\boldsymbol{u}\cdot\nabla T=\nabla\cdot(\lambda_{eq}\nabla T)+Q_h, \tag{4.4}$$

where T [K] is the system temperature, $(\rho C_p)_{eq}$ [J K^{-1} m^{-3}] is the equilibrium volumetric heat capacity, $C_{p,w}$ [J kg^{-1} K^{-1}] is the heat capacity of the fluid, λ_{eq} [W m^{-1} K^{-1}] is the equilibrium thermal conductivity tensor, and Q_h [W m^{-3}] is the heat source.

The mechanical behavior of the rock structure is calculated by the quasi-static equilibrium equation and constitutive poroelasticity.

$$-\nabla \cdot \boldsymbol{\sigma} = \boldsymbol{F}_v , \tag{4.5}$$

$$\boldsymbol{\sigma} = \boldsymbol{E} : (\boldsymbol{\varepsilon} - \boldsymbol{\varepsilon}_T) + \alpha_B p\boldsymbol{I} , \tag{4.6}$$

where $\boldsymbol{\sigma}$ [Pa] is the stress tensor, $\boldsymbol{F_v}$ [Pa m^{-1}] is the body force, $\boldsymbol{E}$ [Pa] is the elasticity tensor , $\boldsymbol{\varepsilon}$ [-] is the strain tensor, $\boldsymbol{\varepsilon}_T$ [-] is the thermal strain tensor, α_B [-] is the Biot-Willis coefficient, and $\boldsymbol{I}$ [-] is the identity tensor.

The reactive transport behavior is calculated by the basic advection-diffusion equation. The mechanical dispersion and sorption processes are not considered here.

$$\frac{\partial(c_i \phi)}{\partial t} + \boldsymbol{u} \cdot \nabla c_i = \nabla \cdot (\phi\tau \boldsymbol{D}_{b,i} \nabla c_i) + r_i , \tag{4.7}$$

where c_i [mol m^{-3}] is the concentration of solute i in the pore water, $\boldsymbol{D}_{b,i}$ [m^2 s^{-1}] is the diffusion coefficient tensor, τ [-] is the coefficient related to tortuosity, and r_i [mol m^{-3} s^{-1}] is the source term of solute i. The diffusion coefficient is temperature-dependent and can be defined by an Arrhenius-type equation [4.30), as

$$D_{b,i} = D_{b,i}^0 \exp(-E_{D,i} / RT) , \tag{4.8}$$

where $D_{b,i}^0$ [m^2 s^{-1}] and $E_{D,i}$ [J mol $^{-1}$] are the pre-exponential factor and the activation energy of the diffusion of solute i, respectively, and R [J mol $^{-1}$K^{-1}] is the gas constant. In this chapter, the rock domain consists of multi-minerals. When the number of minerals included in the targeted rocks is n, the total solute source is expressed by

$$r_i = \sum_j^n v_{i,j} R_j , \tag{4.9}$$

where $v_{i,j}$ [-] is the stoichiometry coefficient of solute i in reaction of mineral j and R_j [mol m^{-3} s^{-1}] is the rate of the mineral reactions for mineral j.

4.2.2 Mineral reactions

The mineral reactions includes free-face dissolution/precipitation and pressure dissolution. Thus, R_j is expressed by

$$R_j = R_{f,j}^{FF} + R_{f,j}^{PS}, \tag{4.10}$$

where $R_{f,j}^{FF}$ [mol m^{-3} s^{-1}] is the rate of the free-face dissolution/precipitation of mineral j within the rock fracture, and $R_{f,j}^{PS}$ [mol m^{-3} s^{-1}] is the rate of the pressure dissolution of mineral j at contacting asperities within the rock fracture. Firstly, the way to estimate the rate of the free-face dissolution/precipitation within the rock fracture is shown. The fracture area, composed of contacting asperities and the pore space, is set as the representative element (**Fig. 4.1**). The flux of the free-face dissolution/precipitation per time in the representative element is represented by$^{4.7)}$

$$\dot{M}_f^{FF} = k_+ A_{rea}(1 - Q / K_{eq,}), \tag{4.11}$$

where $\dot{M}_f^{FF}$ [mol s^{-1}] is the flux of mineral j, by the free-face dissolution/precipitation per time in the representative element, k_+ [mol m^{-2} s^{-1}] is the mineral dissolution rate constant, Q [-] is the ionic activity product, K_{eq} [-] is the equilibrium constant, and A_{rea} [m^2] is the reactive surface area. The reactive surface area is obtained by a geometric relation in the representative element, given as

$$A_{rea} = 2(1 - R_{f,c}) A_t^l, \tag{4.12}$$

$$R_{f,c} = \frac{A_c^l}{A_t^l}, \tag{4.13}$$

where $R_{f,c}$ [-] is the contact-area ratio within the fracture, A_t^l [m^2] is the total fracture cross-sectional area in the representative element, and A_c^l [m^2] is the contact area within the fracture of the representative element.

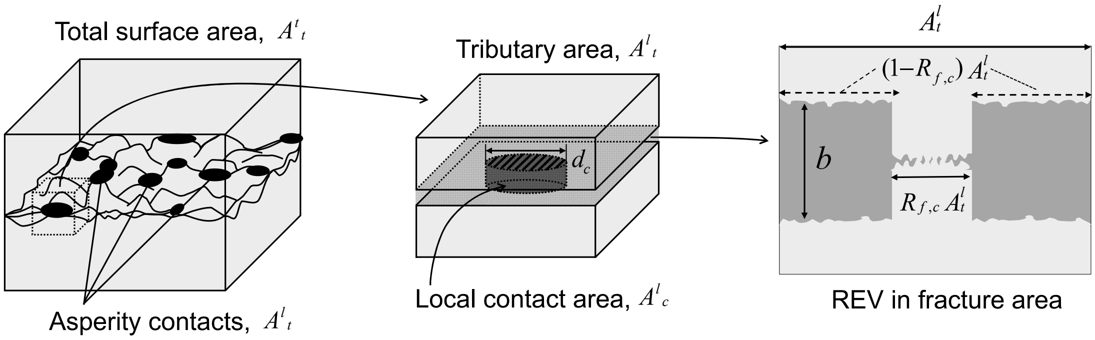

Fig. 4.1 Geometrical model that includes representative element in rock fracture area[4.4)]. Tributary area $A^l{}_t$ (center) is the representative element composed of asperity contact area $R_{f,c}A^l{}_t$ and pore space (right side).

The mineral dissolution rate constants are defined by the Arrhenius expression, given as

$$k_{+,j} = k^0_{+,j}\exp(-E_{k_{+,j}}/RT)\,, \tag{4.14}$$

where k^0_{+j} [mol m^{-2} s^{-1}] is the pre-exponential factor of mineral j and $E_{k_{+,j}}$ [J mol $^{-1}$] is the activation energy of the dissolution of mineral j. The volume of the pore space in the representative element is expressed by

$$V_p = (1-R_{f,c})\,A^l_t \cdot b\,, \tag{4.15}$$

where V_p [m^3] is the volume of the pore space in the representative element and b [m] is the average mechanical fracture aperture. The rate of the free-face dissolution/precipitation within the rock fracture can be obtained by dividing Eq. (4.11) by Eq. (4.15), as follows:

$$R^{FF}_f = 2k_+(1-Q\ /K_{eq})/b\,. \tag{4.16}$$

It represents the rate of the free face dissolution/precipitation for rock composed of a single mineral. Therefore, it can be extended to that for rock composed of multi-minerals[4.6)]. Defining the volumetric ratio of mineral j as χ_j, and the roughness factor[4.31)] $f_{r,j}$ of mineral j, which is the ratio of the true (microscopic) surface area over the apparent (geometric) surface area, the rate of the free-face dissolution/precipitation for mineral j is given by

$$R^{FF}_{f,j} = 2f_{r,j}\chi_j k_{+,j}(1-Q_j/K_{eq,j})/b\,. \tag{4.17}$$

The roughness factor is calculated by the specific surface area, as follows:

$$f_{r,j} = \frac{S_j}{6/(\rho_j d_j)}, \tag{4.18}$$

where S_j [m^2 g-^{1}] is the specific surface area of mineral j, ρ_j [kg m^{-3}] is the density of mineral j, and d_j [m] is the grain diameter of mineral j. If the number of minerals composing the targeted rock is n, the total rate of the free-face dissolution/precipitation can be defined as

$$R_f^{FF} = \sum_j^n R_{f,j}^{FF} = \sum_j^n 2 f_{r,j} \chi_j k_{+,j} (1 - Q_j / K_{eq,j}) / b. \tag{4.19}$$

When the rock is far from the equilibrium condition, it may be possible to simplify Eq. (4.19) by ignoring the effect of the precipitation.

$$R_f^{FF} = \sum_j^n R_{f,j}^{FF} = \sum_j^n 2 f_{r,j} \chi_j k_{+,j} / b. \tag{4.20}$$

Secondly, the way to estimate the rate of pressure dissolution at the contacts within rock fractures is shown. Yasuhara et al.[4.4)] defined the strain rate of the pressure dissolution at the contacting asperities within a fracture by evaluating the gradient of chemical potential between the contacting fracture asperities and the void space in the fracture area, given as

$$\begin{aligned} \dot{\varepsilon}_f^{PS} &= \frac{1}{V}\frac{dV}{dt} = \frac{V_m^2 k_+}{RTb}\left(\sigma_a - \sigma_c\right) \\ &= \frac{1}{b}\frac{\Delta b}{\Delta t} = \frac{V_m^2 k_+}{RTb}\left(\frac{\sigma_n}{R_{f,c}} - \sigma_c\right), \end{aligned} \tag{4.21}$$

$$\sigma_a = \frac{\sigma_n}{R_{f,c}}, \tag{4.22}$$

where $\dot{\varepsilon}_f^{PS}$ [s^{-1}] is the strain rate of the pressure dissolution at the contacting asperities within the fracture, V_m [m^3 mol^{-1}] is the molar volume, σ_a [Pa] is the disjoining pressure[4.32)] which is the stress acting at the contacting asperities within the fracture, σ_c [pa] is the critical stress[4.30)], and σ_n [Pa] is the compressive effective stress acting on the rock domain. The derived strain rate in Eq. (4.21) shows the uniaxial compressive state. However, under real stress conditions, pressure dissolution may occur under triaxial compressive conditions. Therefore, it is necessary to extend Eq. (4.21) to the one for such conditions. The volumetric strain summing the principal strains may represent the strain induced by the pressure dissolution under the triaxial compressive conditions, and the extended strain rate may be expressed as

$$\begin{aligned}\dot{\varepsilon}_f^{PS} &= \dot{\varepsilon}_1^{PS} + \dot{\varepsilon}_2^{PS} + \dot{\varepsilon}_3^{PS} = \frac{V_m^2 k_+}{RTb}\left(\frac{\sigma'_1 + \sigma'_2 + \sigma'_3}{R_{f,c}} - 3\sigma_c\right) \\ &= \frac{3V_m^2 k_+}{RTb}\left(\frac{\sigma'_1 + \sigma'_2 + \sigma'_3}{3R_{f,c}} - \sigma_c\right) = \frac{3V_m^2 k_+}{RTb}\left(\frac{\sigma'_m}{R_{f,c}} - \sigma_c\right)\end{aligned}, \qquad (4.23)$$

$$\sigma'_m = \frac{\sigma'_1 + \sigma'_2 + \sigma'_3}{3}, \qquad (4.24)$$

where $\dot{\varepsilon}_1^{PS}$, $\dot{\varepsilon}_2^{PS}$, and $\dot{\varepsilon}_3^{PS}$ [s^{-1}] are the strain rates in the first, second, and third principal stress directions induced by the pressure dissolution, respectively, σ'_m [Pa] is the mean effective stress, and σ'_1, σ'_2, and σ'_3 [Pa] are the first, second, and third principal effective stresses, respectively. Then, the change in the averaged mechanical aperture, due to the pressure dissolution, is defined using Eq. (4.23).

$$\frac{\Delta b}{\Delta t} = \frac{\dot{V}^{PS}}{A_c^l} = \frac{3V_m^2 k_+}{RT}\left(\frac{\sigma'_m}{R_{f,c}} - \sigma_c\right), \qquad (4.25)$$

where $\dot{V}^{PS}$ [m^{3}s^{-1}] is the rate of volume change by the pressure dissolution in the representative element. The rate of volume change by pressure dissolution $\dot{V}^{PS}$ is obtained by Eq. (4.25) and by the relation $A_c^l = R_{f,c} A_t^l$ as

$$\dot{V}^{PS} = \frac{\Delta b \cdot A_c^l}{\Delta t} = \frac{3V_m^2 k_+ R_{f,c} A_t^l}{RT}\left(\frac{\sigma'_m}{R_{f,c}} - \sigma_c\right). \qquad (4.26)$$

Accordingly, the mineral dissolution flux per time by the pressure dissolution in the representative element is defined by dividing Eq. (4.26) by the molar volume, as follows:

$$\dot{M}_f^{PS} = \frac{3V_m k_+ R_{f,c} A_t^l}{RT}\left(\frac{\sigma'_m}{R_{f,c}} - \sigma_c\right), \qquad (4.27)$$

where $\dot{M}_f^{PS}$ [mol s^{-1}] is the flux with pressure per time in the representative element. Finally, the rate of pressure dissolution in a rock fracture is defined by dividing Eq. (4.27) by Eq. (4.15).

$$R_f^{PS} = \frac{3V_m k_+ R_{f,c}}{RTb(1-R_{f,c})}\left(\frac{\sigma'_m}{R_{f,c}} - \sigma_c\right). \tag{4.28}$$

As shown in the case of the free-face dissolution/precipitation, the rate of pressure dissolution for mineral *j* is defined using the volumetric ratio and the roughness factor of mineral *j*, given as

$$R_{f,j}^{PS} = \frac{3f_{r,j}\chi_j V_{m,j} k_{+,j} R_{f,c}}{RTb(1-R_{f,c})}\left(\frac{\sigma'_m}{R_{f,c}} - \sigma_c\right), \tag{4.29}$$

4.2.3 Aperture change with mineral reactions

The interactive processes for free-face dissolution/precipitation and pressure dissolution irreversibly alter the fracture mechanical aperture, and the contact area within the fracture changes due to the change in mechanical aperture. The relationship between the mechanical fracture aperture and the contact area within the fracture in the representative element may be given by the following simple equation[4.4)]:

$$b = b_r + (b_0 - b_r)\exp(-(R_{f,c} - R_{f,c0})/a), \tag{4.30}$$

where b_r [m] is the residual fracture aperture, b_0 [m] is the initial fracture aperture, and a [-] is a constant. $R_{f,c0}$ [-] is the initial contact-area ratio within the fracture. The relationship indicated by Eq. (4.30) is shown in **Fig. 4.2**. Constant a is an important parameter that effects the gradient of the curve.

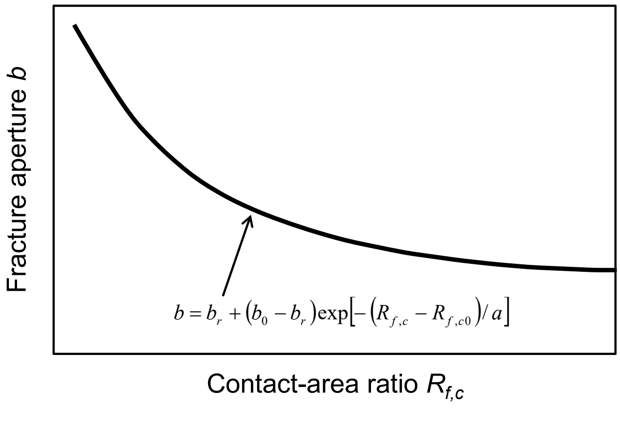

Fig. 4.2 Relation between fracture aperture and contact-area ratio[4.6)].

In this chapter, changes in the fracture aperture are only induced by the mineral reactions of both free-face dissolution/precipitation and pressure dissolution. The rate of aperture change due to the free-face dissolution/precipitation and pressure dissolution in the rock fracture is defined as follows:

$$\dot{b}^{FF} = \frac{\sum_{j}^{n} M_{f,j}^{FF} \cdot V_{m,j}}{A_l^t} = \sum_{j}^{n} 2 f_{r,j} \chi_j k_{+,j} (1 - R_{f,c}) V_{m,j} (1 - \frac{Q_j}{K_{eq,j}}), \tag{4.31}$$

$$\dot{b}^{PS} = -\frac{\sum_{j}^{n} \dot{M}_{f,j}^{PS} \cdot V_{m,j}}{A_c^l} = \sum_{j}^{n} \frac{-3 f_{r,j} \chi_j V_{m,j}^2 k_{+,j}}{RT} \left(\frac{\sigma'_m}{R_{f,c}} - \sigma_c \right), \tag{4.32}$$

where $\dot{b}^{FF}$ [m s^{-1}] is the rate of change in fracture aperture by the free-face dissolution/precipitation and $\dot{b}^{PS}$ [m s^{-1}] is the rate of change in fracture aperture by pressure dissolution. The average mechanical fracture aperture at an arbitrary time is evaluated using Eq. (4.33).

$$b(t) = b_0 + \int \dot{b}^{FF}(t)dt + \int \dot{b}^{PS}(t)dt, \tag{4.33}$$

Once the mechanical fracture aperture is calculated, the hydraulic fracture aperture is also evaluated using the following relationship[4.33),4.34)] between the hydraulic fracture aperture and the mechanical fracture aperture:

$$b_h^3 = \frac{(1 - R_{f,c})}{(1 + R_{f,c})} b^3, \tag{4.34}$$

In this chapter, COMSOL Multiphysics[4.35)] is used to solve the differential equations. The calculation procedure of the model is shown in **Fig. 4.3**. Using the scheme whereby the dependent variables (i.e., fracture aperture/permeability, flow velocity, stress, temperature, and dissolution/precipitation rate constants) are exchanged reciprocally, the coupled THMC processes are calculated sequentially.

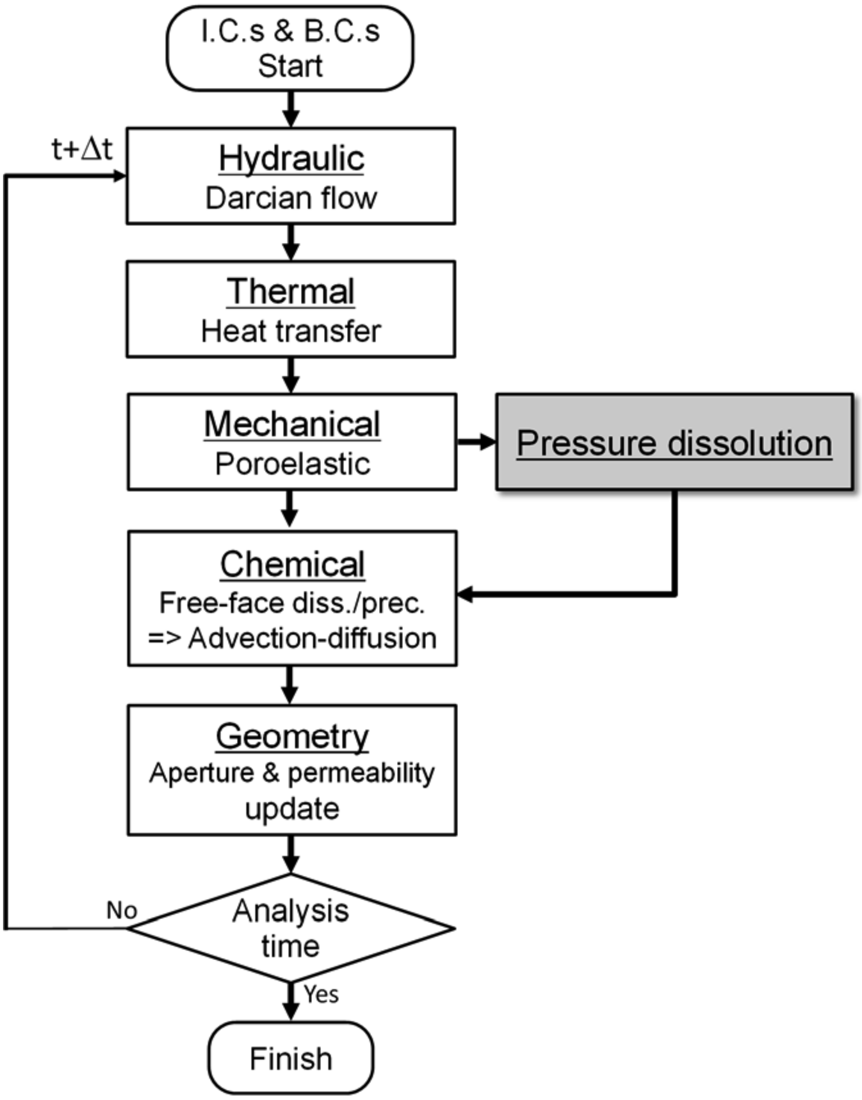

Fig. 4.3 Sequential procedure to conduct consistent calculations of changes in aperture with time.

4.3 Model verification

4.3.1 Replicating experimental measurements

In order to verify the model proposed in the previous section, an attempt is made to replicate the experimental results by the model. The experiments that are targeted for the numerical analysis are the flow-through experiments conducted on granite and mudstone samples[4.6)]. Rock samples which have a single artificial fracture, shown in **Fig. 4.4**, are used for the experiments. The experimental setup is also shown in this figure. Two experiments, namely, E-3 and H-11, are conducted with samples of granite (30 mm in diameter × 60 mm in length) and mudstone (50 mm in diameter × 100 mm in length), respectively. E-3 is conducted using deionized water (pH ~7) as the permanent at a confining pressure of 5.0 MPa, time-dependent temperatures of 25 and 90°C (0-380 h: 25°C, after 380 h: 90°C), and at differential water pressure levels ranging from 0.04 to 0.10 MPa. Similarly, H-11 is conducted using deionized water (pH ~6) at a confining pressure of 3.0 MPa, a temperature of 90°C, and a differential water pressure of 0.4 MPa. In the two experiments, the hydraulic aperture is obtained from the measured flow rate via the parallel plate approximation of Eq. (4.35).

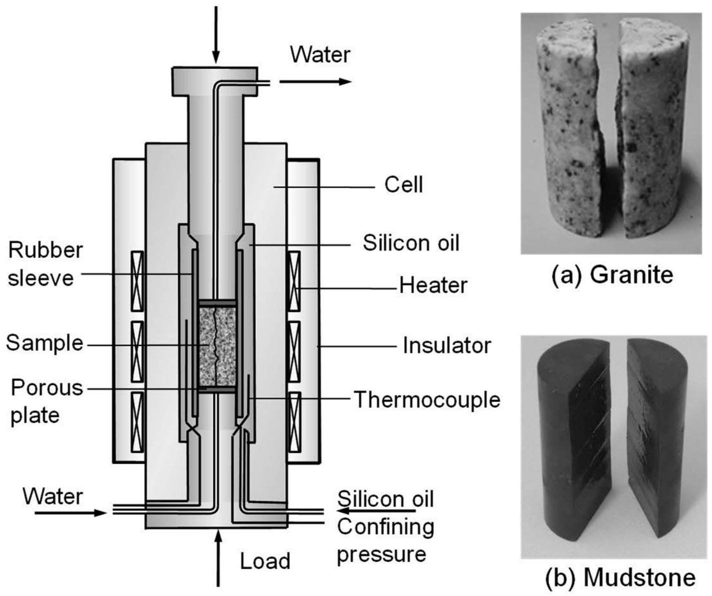

(a) Granite

(b) Mudstone

Fig. 4.4 Schematic of flow-through experiment (left side) and rock samples (right side) [4.6)].

$$<b_h> = \left(\frac{12\mu l Q}{w\Delta p}\right)^{1/3} \tag{4.35}$$

Q [m^3 s^{-1}] represents the measured flow rates, Δp [Pa] is the differential pressure, $<b_h>$ [m] is the equivalent hydraulic aperture, w [m] is width of the sample, and l [m] is the length of the sample. The concentrations of effluent elements (Si, Al, K, Fe, Ca, Na, and Mg) are obtained by examining the compositions of the fluid samples taken from the flow outlet in the two experiments using inductively coupled plasma atomic emission spectrometry (ICP-AES). The chemical compositions of the granite and mudstone used for the experiments are listed in **Table 4.1**$^{4.6)}$.

The numerical calculations using the coupled THMC model presented in this chapter are conducted to reproduce the experimental measurements of the evolution in the hydraulic fracture aperture and the effluent element concentrations for the granite (E-3) and mudstone (H-11) experiments.

Table 4.1 Compositions of granite and mudstone$^{4.6)}$.

Oxide	Granite results (wt%)	Mudstone results (wt%)
SiO_2	65.47	71.2
Al_2O_3	11.56	10.7
K_2O	7.39	2.78
Fe_2O_3	6.24	6.78
CaO	3.75	1.66
Na_2O	3.40	1.51
TiO_2	0.55	0.876
MgO	0.54	1.51
MnO	0.24	
SO_3		3.26
Others	0.66	0.48

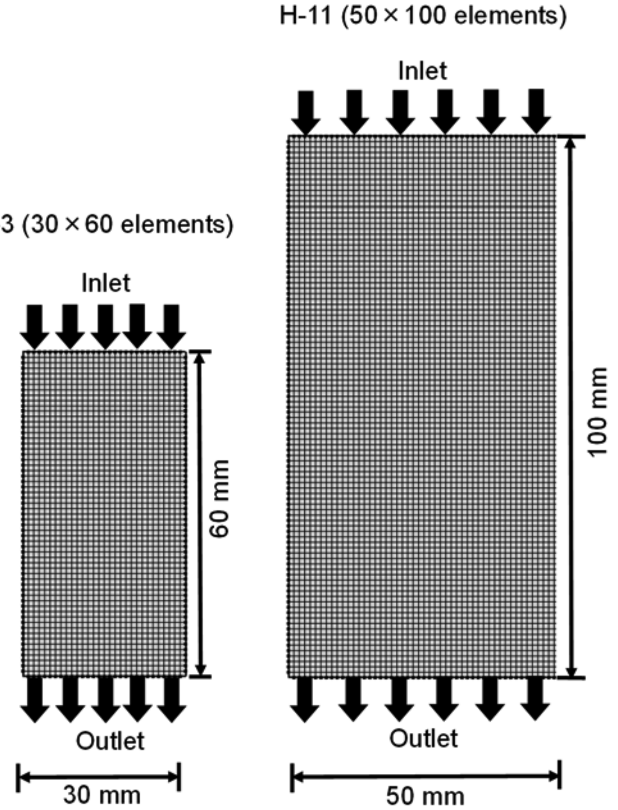

Fig. 4.5 Model geometry for analysis of E-3 and H-11.

The numerical domains that represent the rock fractures of the samples in two dimensions are set to be squares with a width of 30 mm and a length of 60 mm (E-3) and with a width of 50 mm and a length of 100 mm (H-11), respectively, and these domains for E-3 and H-11 are divided into 1800 and 5000 square elements, respectively (**Fig. 4.5**). In the models for E-3 and H-11, the equivalent values are applied as the initial hydraulic aperture and the contact-area ratio within the entire domains. The values for the initial hydraulic aperture are obtained from the experimental measurements for E-3 and H-11. As noted in Yasuhara and Elsworth[4.20)], the values for the initial contact-area ratio, the residual aperture, and constant *a* should be derived by evaluating the relation represented in Eq. (4.30) from the experimental measurements. However, the relation is not obtained from the two experiments. Thus, the initial contact-area ratio, the residual aperture, and constant *a* are assumed to be almost equivalent to those defined by Yasuhara et al.[4.6)]. The critical stresses are assumed to be 100 MPa and 15 MPa for E-3 and H-11, respectively, which are almost equivalent to their uniaxial compressive strength. The isothermal condition within the entire domains changes from 25°C to 90°C, corresponding to the experimental period for E-3, and is an invariant of 90°C for H-11. All the element (Si, Al, K, Fe, Ca, Na, and Mg) concentrations of 0 mol m^{-3} are prescribed as the initial condition within the domain and as the fixed concentration condition of the inlet boundary for E-3 and H-11. In the calculation of the mineral reactions, the model uses Eq. (4.20). This equation assumes that, based on the experimental observations, the dissolved mineral concentrations are far from equilibrium[4.6)]. Therefore, the concentrations of each element depend only on time and temperature and are calculated via the simple rate law of Eq. (4.20).

The differential pressures are set at the inlet and outlet boundaries of the domain to be in the range of 0.04-0.1 MPa and 0.4 MPa for E-3 and H-11, respectively. The mass of the water and the chemical species are obtained at the outlet boundary. For all models, an effective stress analysis is conducted by considering the distributions of both confining pressure and water pressure, and the thermal expansion of the rock structure is not considered. In the numerical analysis for the granite experiment, E-3, five minerals, namely, quartz (50 vol.%), orthoclase (20 vol.%), albite (8.0 vol.%), anorthite (20 vol.%), and biotite (2.0 vol.%), are considered (**Table 4.2**)[4.6)]. In the case of the mudstone experiment, H-11, six minerals, namely, quartz (10 vol.%), orthoclase (10 vol.%), albite (15 vol.%), Illite (13 vol.%), smectite (12 vol.%), and Opal-CT (40 vol.%), are considered (**Table 4.3**)[4.36)]. In the predictions for the granite experiment, it is assumed that the surface roughness of the rock fracture is equivalent to that of the minerals composing the rock. Therefore, in all the predictions, the roughness factors of the minerals composing the granite (see Eq. (4.18)) are estimated using the specific surface area of the granite-ground particles measured by the BET method[4.6)]. However, the roughness factor of biotite is calculated using only the specific surface area of the biotite itself, obtained from the literature[4.37)], because it is much greater than the specific surface areas of the other four minerals (i.e., quartz, orthoclase, albite, and anorthite). For the granite experiment, the roughness factor of quartz, orthoclase, albite, and anorthite is 7.12 [4.6)] and that of biotite is 512[4.37)] (**Table 4.2**). Similarly, in the case of the mudstone predictions, the roughness factors of the minerals composing the mudstone are also estimated using the specific surface area of the mudstone-ground particles measured by the BET method, but those of illite and smectite are calculated using the values obtained from the literature[4.38)]. For the mudstone experiment, the roughness factor of quartz, orthoclase, albite, and Opal-CT is 219 and that of illite and smectite are 513 and 1860, respectively (**Table 4.3**)[4.38)]. The parameters of the kinetic dissolution rate constant (see Eq. (4.14)) for the minerals considered in the calculations obtained from literature are given in **Table 4.4**[4.39)~4.45)].

Table 4.2 Calculation setting of mineral composition and roughness factor in calculations for E-3[4.6),4.37)] .

Composition	Vol (%)	Roughness factor f_r
Quartz	50	7.12
Orthoclase	20	7.12
Albite	8.0	7.12
Anorthite	20	7.12
Biotite	2.0	512

Table 4.3 Calculation settings of mineral composition and roughness factor in calculations for H-11[4.36),4.38)].

Composition	Vol (%)	Roughness factor f_r
Quartz	10	219
Orthoclase	10	219
Albite	15	219
Illite	13	513
Smectite	12	1860
Opal-CT	40	219

Furthermore, each calibration of the parameters used in the analysis is shown in **Table 4.5**[4.6),4.30),4.37)~4.45)].

Table 4.4 Parameters of kinetic dissolution rate constant for minerals[4.39)~4.45)].

Mineral	Chemical formula	Molar volume (m^3 mol^{-1})	Pre-exponential factor [mol m^{-2} s^{-1}]	Activation Energy (kJ mol^{-1})
Quartz	SiO_2	2.27×10^{-5}	276	90
Orthoclase	$KAlSi_3O_8$	1.09×10^{-4}	1.28×10^{-5}	38.0
Albite	$NaAlSi_3O_8$	1.00×10^{-4}	3.91×10^{-4}	50.7
Anorthite	$CaAl_2Si_2O_8$	1.01×10^{-4}	9.97×10^{-7}	17.8
Biotite	$K\,Mg_{2.5}Fe_{0.5}AlSi_3O_{10}(OH)_{1.75}F_{0.25}$	1.40×10^{-4}	1.01×10^{-7}	22.0
Cristobalite	SiO_2	2.59×10^{-5}	1.20×10^{-1}	65.0
Smectite	$K_{0.04}Ca_{0.5}(Al_{02.8}Fe_{0.53}Mg_{0.7})$ $(Si_{7.65}Al_{0.35})O_{20}(OH)_4$	3.22×10^{-4}	4.64×10^{-5}	49.4
Illite	$(Ca_{0.01}Na_{0.13}K_{0.53})(Al_{1.27}Fe_{0.36}Mg_{0.44})$ $(Si_{3.55}Al_{0.45})O_{10}(OH)_2$	1.48×10^{-4}	4.64×10^{-5}	49.4

Table 4.5 Calibration of parameters used in analysis[4.6),4.30),4.27)~4.45)].

Parameter	Calibration
System temperature T	Equivalent to experimental conditions of E-3[4.6)]and H-11
Diffusion coefficient $D_{b,i}$	Eq. (4.8) with literature[4.30)]
Initial aperture b_0	Experimental measurements of E-3[4.6)] and H-11
Initial contact area ratio $R_{f,c0}$	Equivalent to that defined by Yasuhara et al.[4.6)]
Residual aperture b_r	Equivalent to that defined by Yasuhara et al.[4.6)]
Critical stress σ_c	Nearly equivalent to uniaxial compressive strength
Constant a	Nearly equivalent to that defined by Yasuhara et al.[4.6)]
Roughness factor $f_{r,j}$	Eq. (4.18) with literature[4.6),4.37),4.38)]
Mineral dissolution rate constants $k_{+,j}$	Eq. (4.14) with literature[4.39)~4.45)]

4.3.2. Comparisons with experimental measurements

In the numerical analysis for the granite experiment, E-3, the predictions of the evolution of the hydraulic aperture and the effluent element concentrations obtained from the experimental results were made with the model. These predictions were obtained by utilizing different values for the uncertain parameter, *a* (= 0.02, 0.03, and 0.04), in the relation between the aperture and the contact-area ratio (Eq. (4.30)) to evaluate the influence on the changes in hydraulic aperture and element concentrations.

A comparison of the changes in hydraulic aperture between the experimental results and the predictions for E-3 is shown in **Fig. 4.6**. When the temperature is 25°C (i.e., 0 - 380 h), the predictions with *a* of 0.03 and 0.04 can replicate the experimental data. After increasing the temperature from 25°C to 90°C, predictions with *a* of 0.02 and 0.03 follow the experimental results relatively well. In particular, among the three cases, the prediction with *a* of 0.03 is the most congruent with the measurements throughout the experimental period.

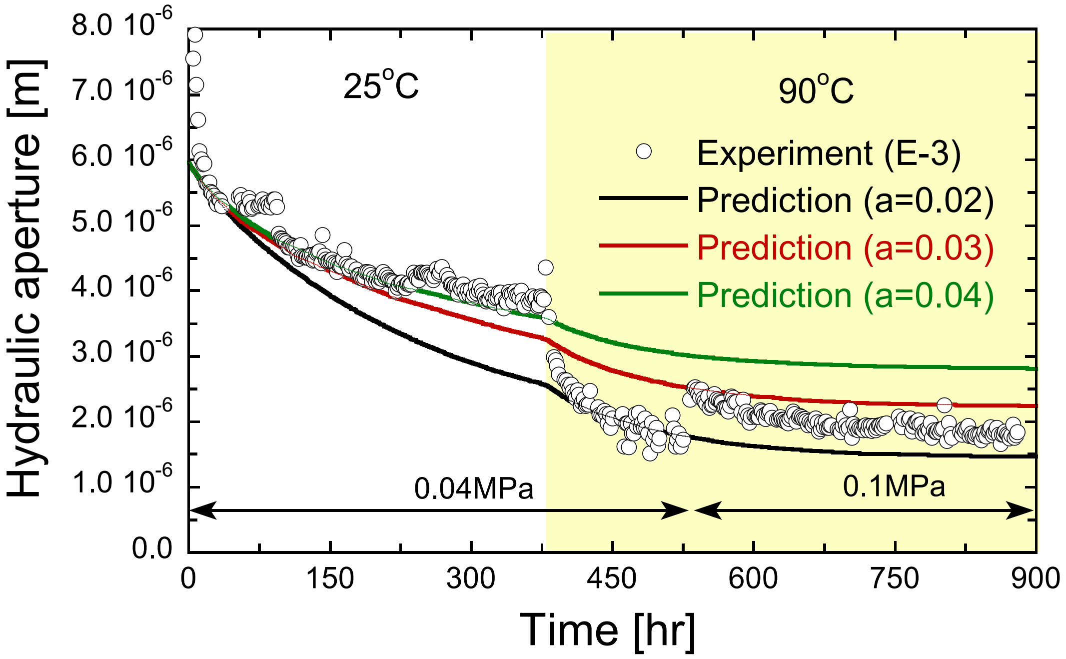

Fig. 4.6 Comparisons of evolution in fracture aperture (E-3) between measurements and predictions with different values for *a* used in Eq. (4.30).

Predictions of the evolution of concentrations for the seven elements for E-3 are shown in **Fig. 4.7**, together with the corresponding experimental data. The predicted changes in concentrations for five elements (i.e., Si, Al, Fe, Ca, and Mg), but not for K and Na, are similar to the measurements. The K and Na concentrations are underestimated by the predictions. In the case of the K concentration, the difference between the experiments and the predictions is relatively small. However, in the case of the Na concentration, the gap is relatively significant, and this is unexplainable at this stage. Although there are some differences between the experiments and the predictions, the current model can predict the evolution of the concentration for most elements. The relationship for each element concentration, between the measurements and the predictions with a = 0.03, is shown in **Fig. 4.8**. This figure shows that the predicted concentrations for four elements (i.e., Al, Fe, Ca, and Mg) coincide well with the measurements for the other elements. All the results for the comparisons between the predictions and the experimental results for E-3 indicate that the current model can replicate changes in the hydraulic aperture and the concentration within the granite fracture due to the mineral reactions (i.e., free-face dissolution and pressure dissolution) only by tuning uncertain parameter a. Previous works[4.6),4.28)], which make predictions of the experimental measurements for E-3 by numerical models, conclude that it is difficult to replicate the evolution in element concentrations only by the simple parameterizations (i.e., tuning of the parameter, namely, a in this work) for mineral reactions. For example, Bond et al.[4.28)] utilized fitting parameters, called "rate enhancement factors", ranging widely from 245 to 10^6 to adjust the rates of free-face dissolution and pressure dissolution. In contrast, the current model shown in this chapter can replicate the experiments without using these fitting parameters in the model[4.28)] .

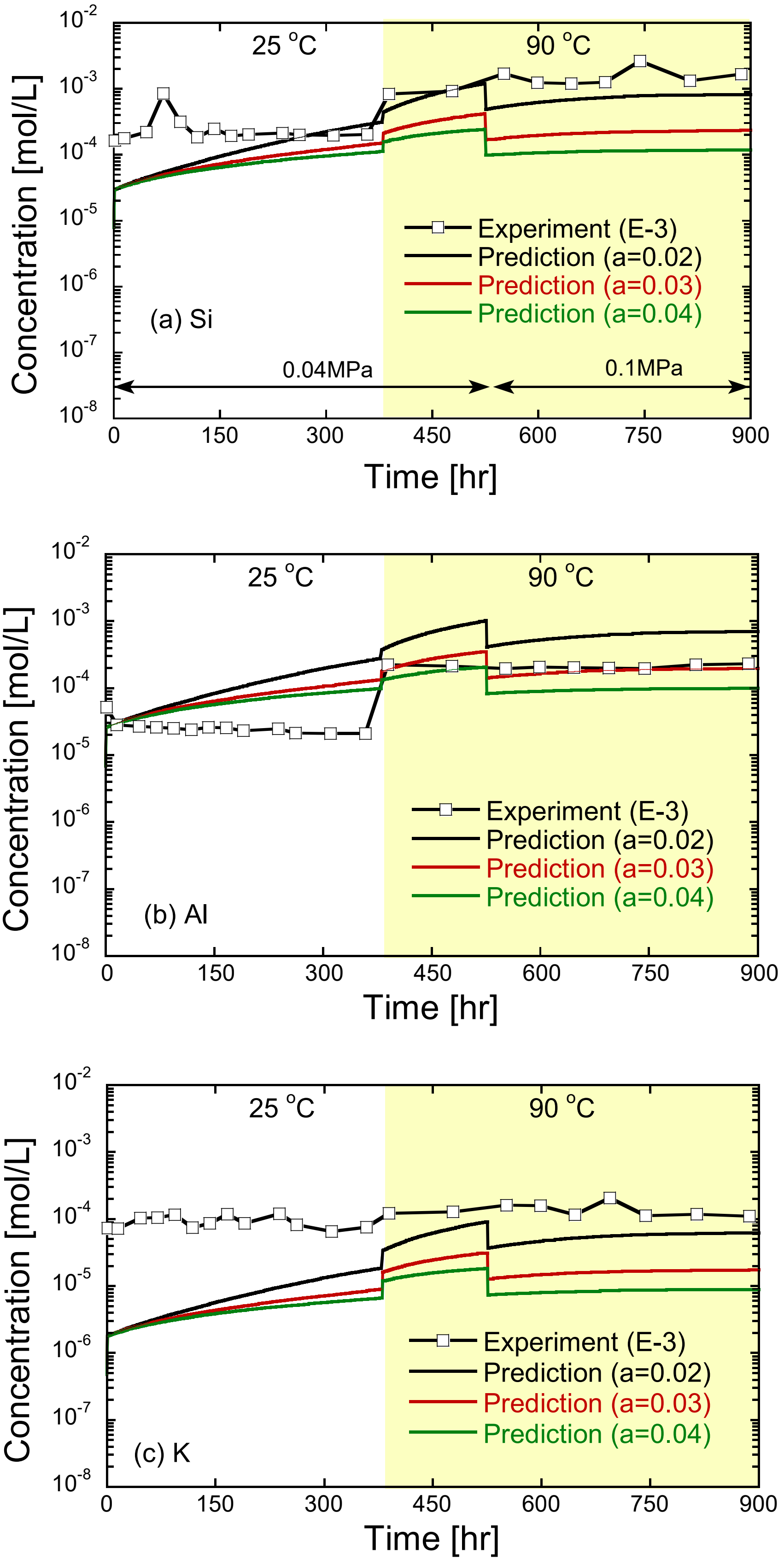
25 °C
90 °C
Experiment (E-3)
Prediction (a=0.02)
Prediction (a=0.03)
Prediction (a=0.04)
(a) Si
0.04MPa
0.1MPa
Concentration [mol/L]
Time [hr]
10^{-2}
10^{-3}
10^{-4}
10^{-5}
10^{-6}
10^{-7}
10^{-8}
0
150
300
450
600
750
900
(b) Al
(c) K

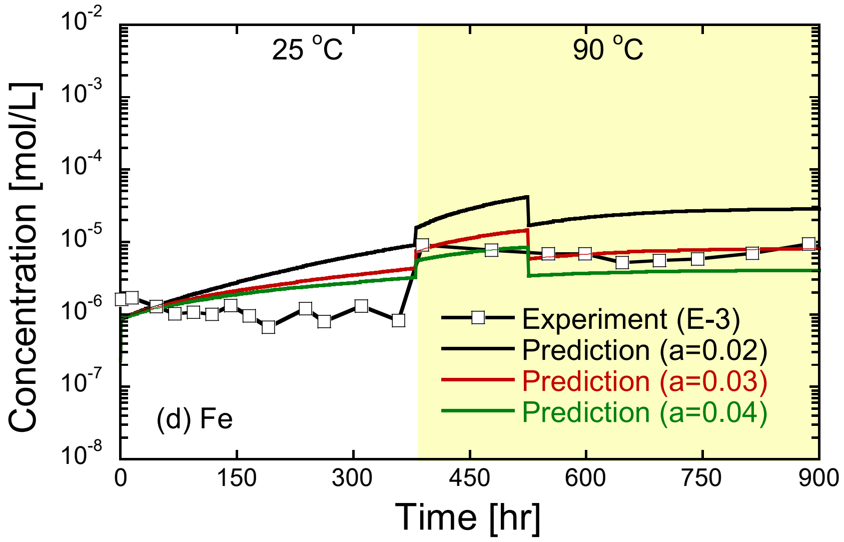
25 °C
90 °C
Experiment (E-3)
Prediction (a=0.02)
Prediction (a=0.03)
Prediction (a=0.04)
(d) Fe
Concentration [mol/L]
10^-2
10^-3
10^-4
10^-5
10^-6
10^-7
10^-8
0
150
300
450
600
750
900
Time [hr]

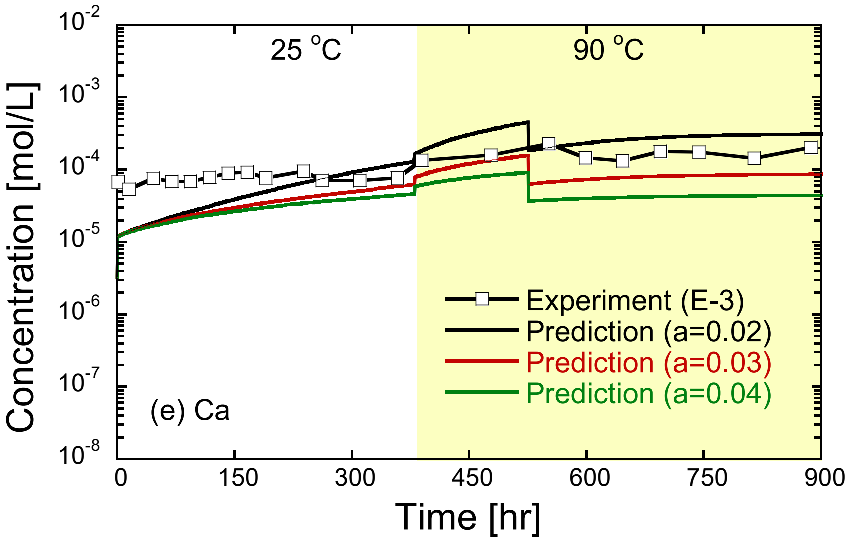
25 °C
90 °C
Experiment (E-3)
Prediction (a=0.02)
Prediction (a=0.03)
Prediction (a=0.04)
(e) Ca
Concentration [mol/L]
10^-2
10^-3
10^-4
10^-5
10^-6
10^-7
10^-8
0
150
300
450
600
750
900
Time [hr]

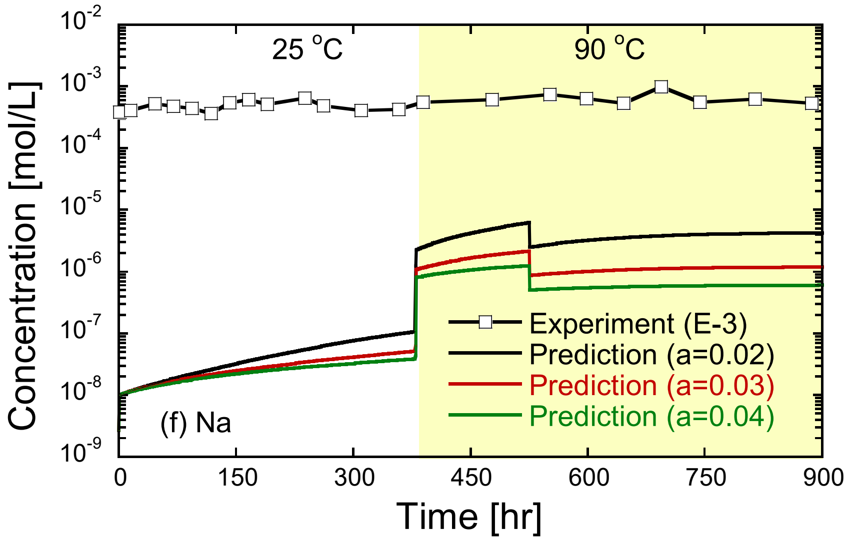
25 °C
90 °C
Experiment (E-3)
Prediction (a=0.02)
Prediction (a=0.03)
Prediction (a=0.04)
(f) Na
Concentration [mol/L]
10^-2
10^-3
10^-4
10^-5
10^-6
10^-7
10^-8
10^-9
0
150
300
450
600
750
900
Time [hr]

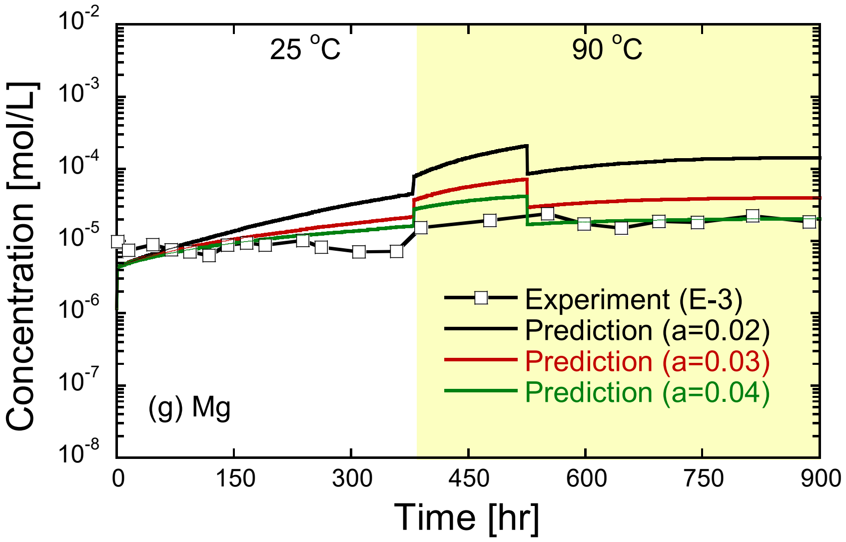

Fig. 4.7 Comparisons of element concentrations (E-3) between measurements and predictions with different values for *a* used in Eq. (4.30): (a) Si, (b) Al, (c) K, (d) Fe, (e) Ca, (f) Na, and (g) Mg.

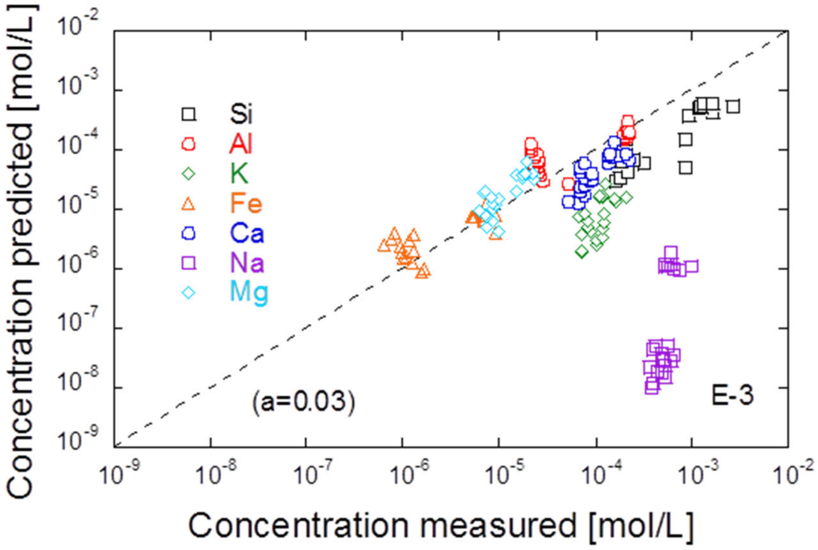

Fig. 4.8 Comparisons of element concentrations (E-3) between measurements and predictions with *a* = 0.03 used in Eq. (4.30).

In the numerical analysis for the mudstone experiment, H-11, the predictions of the evolution of rock permeability and effluent element concentration obtained from the experimental results were made with the model. In these predictions, three kinds of uncertain parameter *a,* namely, 0.06, 0.07, and 0.08, were utilized. Predictions of the evolution in rock permeability for H-11 are shown in **Fig. 4.9**, together with the experimental data. Each prediction with three values for *a* (= 0.06, 0.07, and 0.08) slightly underestimates the experimental measurements, but they are relatively congruent with the measurements taken throughout the experimental period. In particular, among the three cases, the prediction with *a* of 0.08 coincides the best with the measurements.

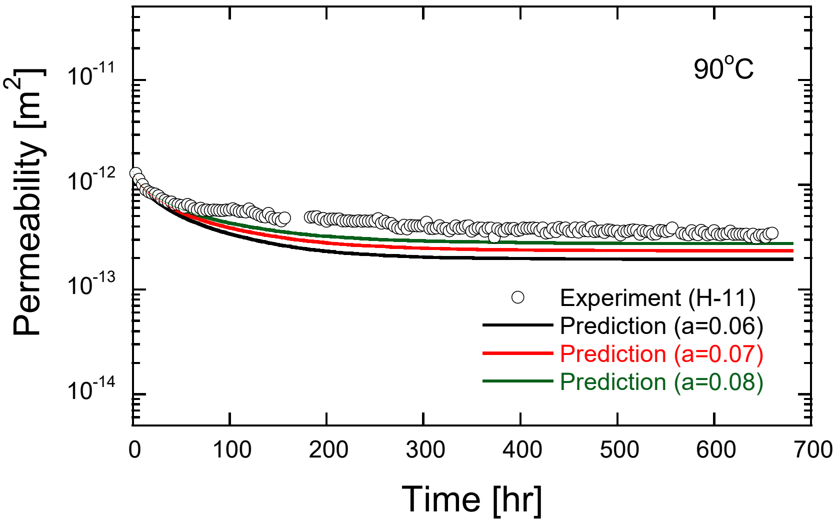

Fig. 4.9 Comparisons of evolution of fracture aperture (H-11) between measurements and predictions with different values for *a* used in Eq. (4.30).

The predicted changes in concentrations for the seven elements for H-11 are shown in **Fig. 4.10**, together with the corresponding experimental data. The trends in evolution for the element concentrations are different between the experiments and the predictions. In the experiments, the concentrations generally decrease with time, while the predicted concentrations increase with time. In experiment H-11, the fracture surfaces of the mudstone sample were not washed with water before initiating the flow. Thus, fine particles might have remained on the surfaces, and the detection of the dissolution of the fine particles might have caused the higher concentrations observed in the early experimental period. This was not considered in the predictions. Consequently, in actual data, the element concentrations are the highest at the beginning of the experiments and they decrease monotonically with time. After 200 h in the experiment, the observed concentrations are likely to be steady. This implies that the dissolution of the fine particles is completed within 200 h and that the dissolution of the rock itself becomes dominant. Once again, in the current model, the above-mentioned mechanism is not taken into account and the predictions are mismatched with the actual data in the early experimental period. However, the predicted concentrations begin to approach the experimental measurements after 200 h. The predictions of concentrations for five elements (i.e., Si, K, Fe, Ca, and Mg), but not for Al and Na, follow the measurements well after 200 h. In particular, the predicted Si concentration is in good agreement with the actual measurement. Comparisons of each element concentration between the measurements and the predictions, with a = 0.06 for the whole experimental period and for that after 200 h, are shown in **Figs. 4.11a** and **11b**, respectively. The mismatches between the measurements and the predictions are apparent from **Fig. 4.11a**, but somewhat better agreements are obtained for the predictions after 200 h, except for Al (**Fig. 4.11b**). Only the Al concentration is significantly overestimated by the prediction during most of the experimental period. This mismatch may be the result of an unaccounted contribution of the precipitation at the fracture void walls, which should be further examined.

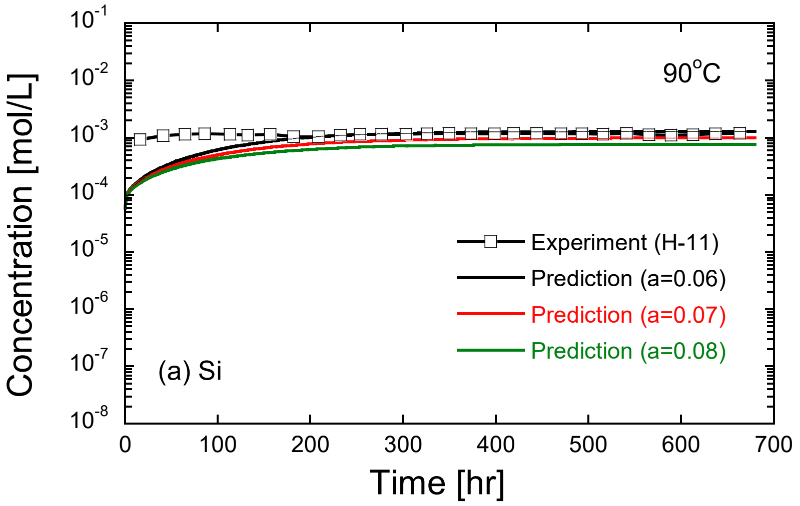

10^{-1}
10^{-2}
10^{-3}
10^{-4}
10^{-5}
10^{-6}
10^{-7}
10^{-8}
Concentration [mol/L]
90°C
Experiment (H-11)
Prediction (a=0.06)
Prediction (a=0.07)
Prediction (a=0.08)
(a) Si
0
100
200
300
400
500
600
700
Time [hr]

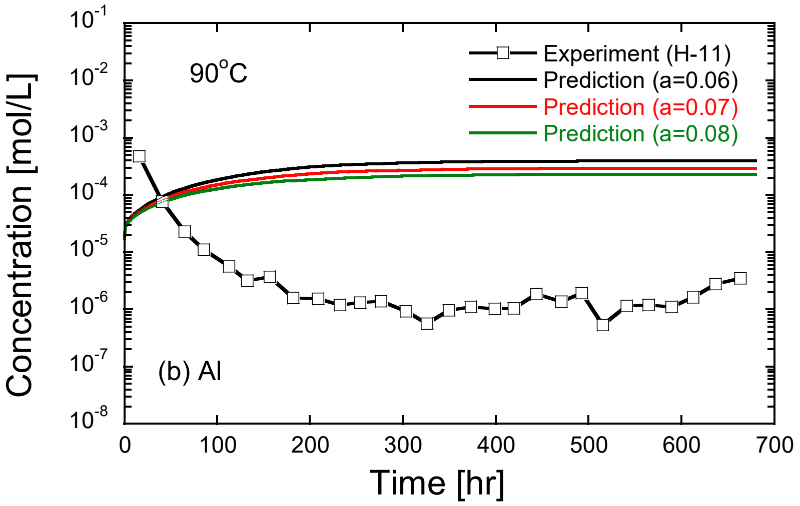

10^{-1}
10^{-2}
10^{-3}
10^{-4}
10^{-5}
10^{-6}
10^{-7}
10^{-8}
Concentration [mol/L]
90°C
Experiment (H-11)
Prediction (a=0.06)
Prediction (a=0.07)
Prediction (a=0.08)
(b) Al
0
100
200
300
400
500
600
700
Time [hr]

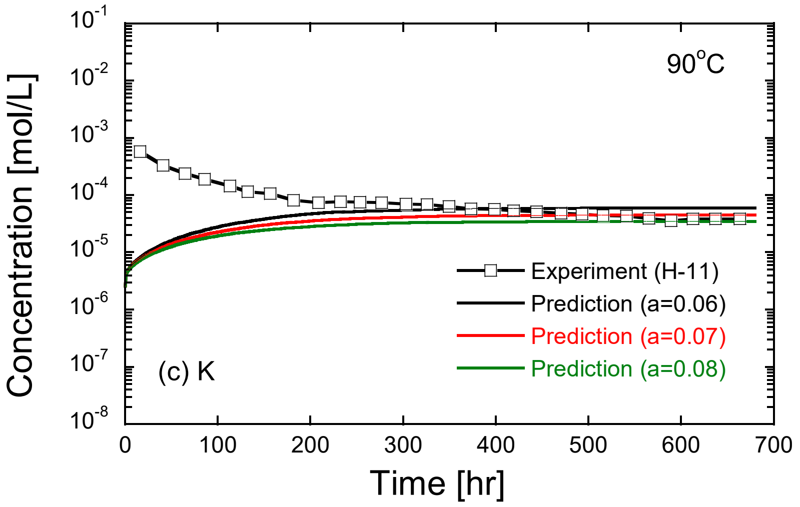

10^{-1}
10^{-2}
10^{-3}
10^{-4}
10^{-5}
10^{-6}
10^{-7}
10^{-8}
Concentration [mol/L]
90°C
Experiment (H-11)
Prediction (a=0.06)
Prediction (a=0.07)
Prediction (a=0.08)
(c) K
0
100
200
300
400
500
600
700
Time [hr]

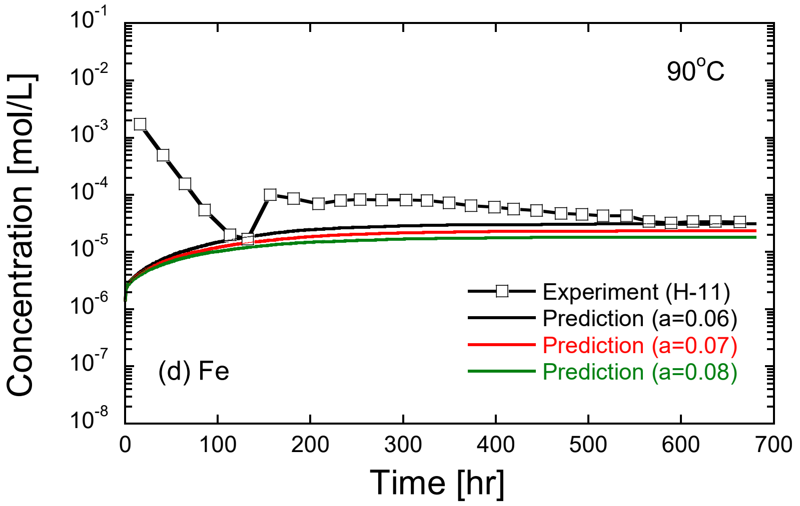

90°C
(d) Fe
Experiment (H-11)
Prediction (a=0.06)
Prediction (a=0.07)
Prediction (a=0.08)
Concentration [mol/L]
Time [hr]
10^{-1}
10^{-2}
10^{-3}
10^{-4}
10^{-5}
10^{-6}
10^{-7}
10^{-8}
0
100
200
300
400
500
600
700

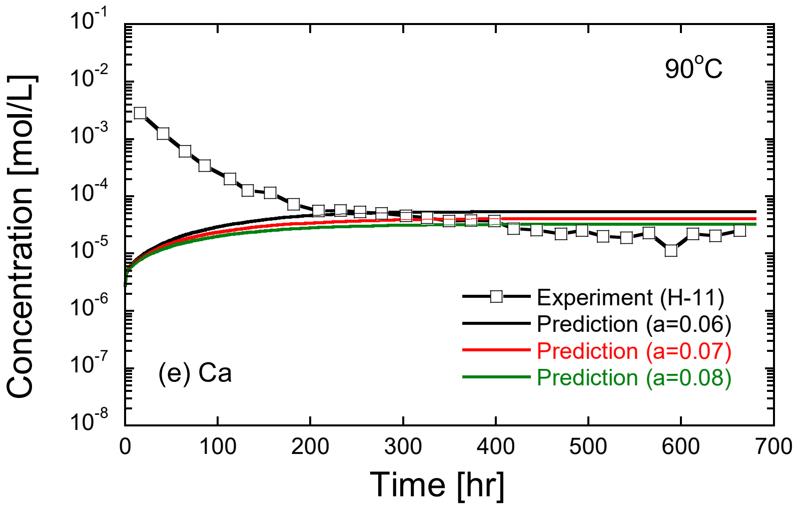

90°C
(e) Ca
Experiment (H-11)
Prediction (a=0.06)
Prediction (a=0.07)
Prediction (a=0.08)
Concentration [mol/L]
Time [hr]
10^{-1}
10^{-2}
10^{-3}
10^{-4}
10^{-5}
10^{-6}
10^{-7}
10^{-8}
0
100
200
300
400
500
600
700

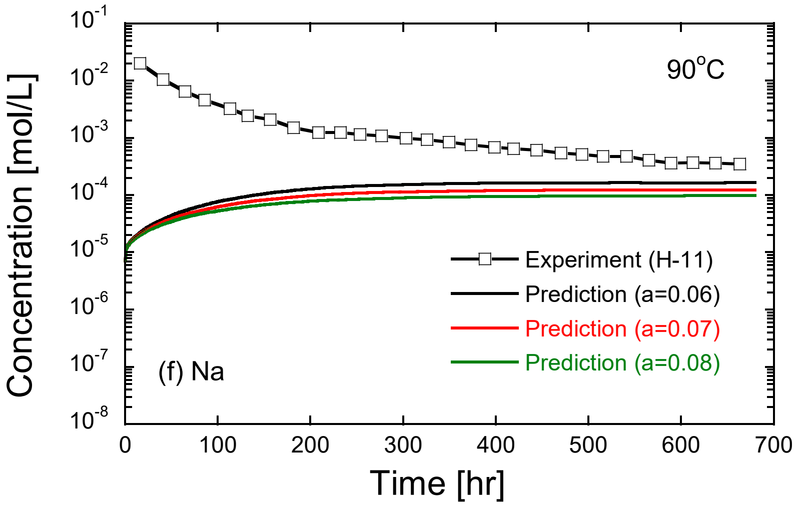

90°C
(f) Na
Experiment (H-11)
Prediction (a=0.06)
Prediction (a=0.07)
Prediction (a=0.08)
Concentration [mol/L]
Time [hr]
10^{-1}
10^{-2}
10^{-3}
10^{-4}
10^{-5}
10^{-6}
10^{-7}
10^{-8}
0
100
200
300
400
500
600
700

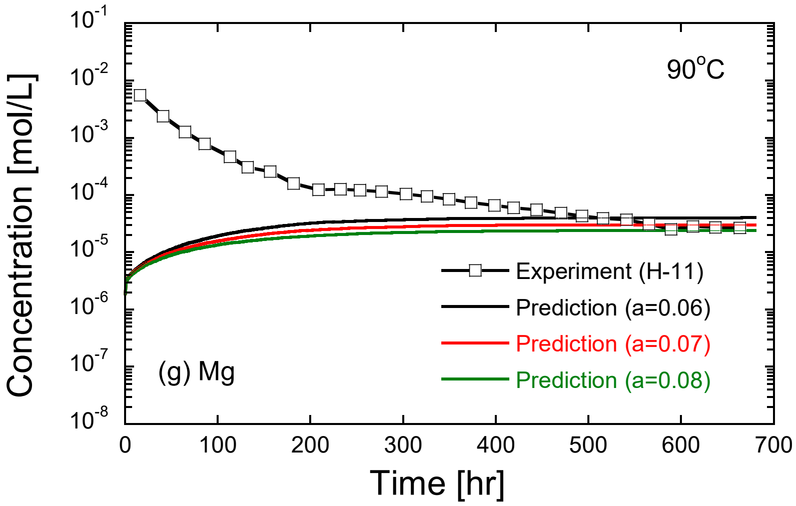

Fig. 4.10 Comparisons of element concentrations (H-11) between measurements and predictions with different values for *a* used in Eq. (4.30): (a) Si, (b) Al, (c) K, (d) Fe, (e) Ca, (f) Na, and (g) Mg.

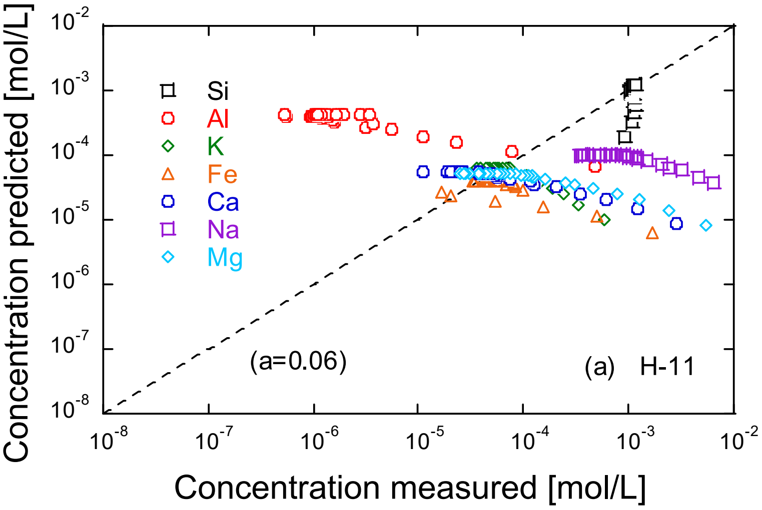

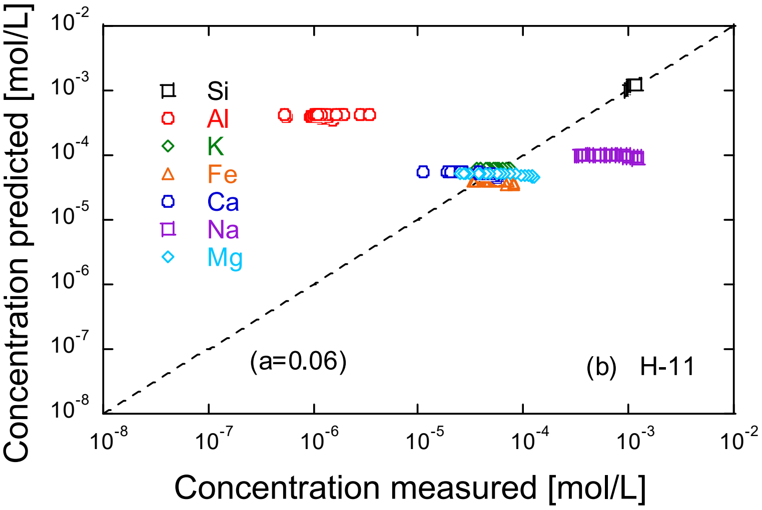

Fig. 4.11 Comparisons of element concentrations (H-11) between measurements and predictions with $a = 0.06$ used in Eq. (4.30): (a) for whole experimental period and (b) for experimental period after 200 h.

All the results of the comparisons between the predictions and the experimental measurements for H-11 indicate that the current model can follow the evolution of rock permeability and element concentrations within the mudstone fracture, resulting in the fact that the dominant mechanism of the changes in permeability should be a convolved phenomenon of the free-face dissolution and pressure dissolution. Overall, a comparison between the results of the numerical analysis and the experiments for E-3 and H-11 provides confidence and support for using the current model to evaluate the evolution in flow and the transport behavior within rock fractures due to the free-face dissolution and the pressure dissolution, depending on the applied stress and temperature conditions.

4.4 Summary

A coupled THMC model was developed based on the finite element scheme to evaluate the evolution of permeability and the reactive transport behavior in fractured rock in the field scale. The model can describe the interactions of the multi-components including heat transfer, fluid flow, the variation in stress distribution, and the reactive transport with mineral reactions (i.e., the free-face dissolution and pressure dissolution). In order to verify the developed model, the model was applied to replicate the experimental results of the changes in hydraulic aperture, fracture permeability, and element concentrations obtained from flow-through experiments conducted on granite and mudstone samples with a single artificial fracture. The predictions for the granite and mudstone experiments showed that the model can replicate the evolution of hydraulic aperture, the fracture permeability, and the effluent element concentrations by a simple parameterization (i.e., adjustment of parameter "*a*" in Eq. (4.30)). Previous coupled THMC models4.20),4.27)~4.29) have needed calibrations using fitting parameters ranging widely from 30 to 10^6 4.20) and 245 to 10^6 4.27)~4.29) when calculating the mineral reactions in order to follow the experiments, but the model presented in this chapter can replicate the experimental measurements without these fitting parameters. Thus, the developed model requires less calibration than the previous models4.20),4.27)~4.29). From the analysis results obtained in this chapter, it can be concluded that the current model should be valid for evaluating the evolution of the fluid flow and mass transport behavior within rock fractures under coupled thermal-hydraulic-mechanical-chemical conditions that may enhance the mineral reactions of free-face dissolution and pressure dissolution. However, some unpredictable behaviors, such as the evolution of the concentrations of the Na and K elements for the granite experiment and that of the Al element concentration for the mudstone experiment, still exist at this stage. Thus, further detailed investigations into the reactive transport behavior due to the geochemical process are required.

References

4.1) Nasir, O., Fall, M. and Evgin, E.: A simulator for modeling of porosity and permeability changes in near field sedimentary host rocks for nuclear waste under climate changes influences. Tunneling and Underground Space Technology, 2014; 42: 122-135.

4.2) Danko, G. and Bahrami, D.: A New T-H-M-C Model Development for Discrete-Fracture EGS studies. GRC Transactions， 2012; 36: 383-392.

4.3) Ghassemi, A.: A review of some rock mechanics issues in geothermal reservoir development. Geotech.Geol. Eng., 2012; 30: 647-664.

4.4) Yasuhara, H., Elsworth, D. and Polak, A.: Evolution of permeability in a natural fracture: the significant role of pressure solution. J. Geophys. Res., 2004; 109(B3): B03204 http://dx.doi.org/10.1029/2003JB002663.

4.5) Yasuhara, H. and Elsworth, D.: Compaction of a rock fracture moderated by competing roles of stress corrosion and pressure solution. Pure. Appl. Geophys., 2008; 165: 1289–1306.

4.6) Yasuhara, H., Kinoshita, N., Ohfuji, H., Lee, DS., Nakashima, S. and Kishida, K.: Temporal alteration of fracture permeability in granite under hydrothermal conditions and its interpretation by coupled chemo-mechanical model. Appl. Geochem., 2011; 26: 2074–2088.

4.7) Lasaga, AC.: Chemical kinetics of water-rock interactions. J. Geophys. Res., 1984; 89: 4009–4025.

4.8) Wely, PK.: Pressure solution and force of crystallization: a phenomenological theory. J. Geophys. Res., 1959; 64: 2001-2025.

4.9) Rutter, EH.: The kinetics of rock deformation by pressure solution. Philos. Trans. R. Soc. London, Ser. A, 1976; A283: 203-219.

4.10) Raj, R.: Creep in polycrystalline aggregates by matter transport through a liquid phase. J. Geophys. Res., 1982; 87: 4731-4739.

4.11) Robin, P-YF.: Pressure solution at grain to grain contacts. Geochim. Cosmochim . Acta., 1978; 42: 1383-1389.

4.12) Zhang, X., Spies, CJ. and Peach, CJ.: Compaction creep of wet granular calcite by pressure solution at 28°C

-150°C. J . Geophys. Res., 2010; 115(B9): B09217.

4.13) Yasuhara, H., Elsworth, D. and Polak, A.: A mechanistic model for compaction of granular aggregates moderated by pressure solution. J. Geophys. Res., 2003; 108(11): 2530, doi.org/10.1029/2003JB002536.

4.14) Zubtsov, S., Renard, F., Gratier, JP., Guiguet, R., Dysthe, DK. and Traskine, V.: Experimental pressure solution compaction of synthetic halite/calcite aggregates. Tectonophysics, 2004; 385: 45-57.

4.15) Nenna, F. and Aydin, A.: The formation and growth of pressure solution seams in clastic rocks: A field and analytically study. J. Struct. Geol., 2011; 33: 633-643.

4.16) Fowler, AC. and Yang, X.: Pressure solution and viscous compaction in sedimentary basins. J. Geophys. Res., 1999; 104(B6): 12989-12997.

4.17) Robert, AC., Ehsan, G., Julia, NP. and Nico, P.: Experimental investigation of fracture aperture and permeability change within Enhanced Geothermal Systems. Geothermics, 2016; 62: 12-21.

4.18) Beeler, MN. and Hickman, SH.: Stress-induced, time-dependent fracture closure at hydrothermal conditions. J. Geophys. Res., 2004; 109(B3): B02211 doi:10.1029/2002JB001782.

4.19) Yasuhara, H., Elsworth, D., Polak, A., Liu, J., Grader, A. and Halleck, P.: Spontaneous permeability switching in fractures in carbonate: lumped parameter representation of mechanically and chemically mediated dissolution. Transp Porous Media, 2006; 65: 385–409.

4.20) Yasuhara, H. and Elsworth, D.: A numerical model simulating reactive transport and evolution of fracture permeability. Int. J. Numer. Anal. Mech Geomech., 2006; 30: 1039-1062.

4.21) Yasuhara, H., Kinoshita, N., Ogata, S., Cheon, DS. and Kishida, K.: Coupled thermo-hydro-mechanical-chemical modeling by incorporating pressure solution for estimating the evolution of rock permeability, Int. J. Rock Mech. Min. Sci., 2016; 86:104-114.

4.22) Lang, PS., Paluszny, A. and Zimmerman, RW.: Hydraulic sealing due to pressure solution contact zone growth in siliciclastic rock fractures. J. Geophys. Res.: Solid Earth., 2016; 120(6): 4080–4101. http://doi.org/10.1002/2015JB011968.

4.23) Bernabe, Y and Evans, B.: Numerical modeling of pressure solution deformation at axisymmetric asperities under normal load. Geol. Soc. London Spec. Publ., 2014; 284:185-205. doi:10.1144/SP284.13.

4.24) Taron, J. and Elsworth, D.: Coupled mechanical and chemical processes in engineered geothermal reservoirs with dynamic permeability. Int. J. Rock Mech. Mi. Sci., 2010; 47: 1339-1348.

4.25) Taron, J., Elsworth, D. and Min, KB.: Numerical simulation of thermal-hydrologic-mechanical-chemical processes in deformable fractured media. Int. J . Rock Mech. Min. Sci., 2009; 46(5): 842-854.

4.26) Zhang, Y-J., Yan, C-S. and Xu, G.: FEM analysis for T-H-M-M coupling processes in dual porosity rock mass under stress corrosion and pressure solution. J. Appl. Math., 2012; Article ID 983718: 21. doi: 10.1155/2012/983718.

4.27) McDermott, C., Bond, A., Harris, AF., Chittenden, N. and Thatcher, K.: Application of hybrid numerical and analytical solutions for the simulation of coupled thermal, hydraulic, mechanical and chemical processes during fluid flow through a fractured rock. Environ. Earth. Sci., 2015; 74: 7837-7854.

4.28) Bond, A., Brusky, I., Chittenden, N., Feng, X-T., Kolditz, O., Lang, P., Lu, R., McDermott, C., Neretnieks, I., Pan, P-Z., Sembera, J., Shao, H. and Yasuhara, H.: Development of approaches for modelling coupled thermal–hydraulic–mechanical–chemical processes in single granite fracture experiments. Environ. Earth. Sci., 2016; 75: 1313.

4.29) Bond, A., Brusky, I., Cao, T., Chittenden, N., Fedors, R., Feng, X-T., Gwo, J-P., Kolditz, O., Lang, P., McDermot, C., Neretnieks, I., Pan, PZ., Sembera, J., Shao, H., Watanabe, N., Yasuhara, H. and Zheng, H.: A synthesis of approaches for modeling coupled thermal-hydraulic-mechanical-chemical process in a single novaculite fracture experiment. Environ. Earth. Sci., 2017; 76: 12.

4.30) Revil, A.: Pervasive pressure-solution transfer a poro-visco-plastic model. Geophys. Res. Lett., 1999; 26: 255–258.

4.31) Murphy, WM. and Helgeson, HC.: Thermodynamic and kinetic constraints on reaction rates among minerals and aqueous solutions. IV. Retrieval of rate constants and activation parameters for the hydrolysis of pyroxene, wollastonite, olivine, andalusite, quartz, and nepheline. Am. J. Sci., 1989; 289: 17-101.

4.32) Heidug, WK.: Intergranular solid-fluid phase transformations under stress: the effect of surface forces. J. Geophys. Res., 1995; 100: 5931–5940.

4.33) Walsh, J.: Effect of pore pressure and confining pressure on fracture permeability. Int. J. Rock Mech. Min. Sci .Geomech., 1981; 18(5): 429-435.

4.34) Zimmerman, RW., Chen, DW. and Cook, NGW.: The effect of contact are on the permeability of fractures. J. Hydrol., 1992; 139: 79-96.

4.35) COMSOL2014：COMSOL MULTIPHYSICS. Version 5.0, Available from www.comsol.com.

4.36) Ochhs, M., Tachi, Y., Trudel, D. and Suyama, T.: Kd Setting Approaches for Horonobe Mudstone Systems: Applications of TSMs and Semi-quantitative Estimation Procedures. JAEA-Research, 2012; 44: 147.

4.37) Kalinowski, BE. and Schweda, P.: Kinetics of muscovite, phlogopite, and biotite dissolution and alternation at pH 1-4, room temperature. Geochim. Cosmochim. Act., 1996; 60: 367-385.

4.38) Macht, F., Eusterhues, K., Pronk, JG. and Totsche, UK.: Specific surface area of clay minerals: composition between atomic force microscopy measurements and bulk-gas (N2) and –liquid (EGME) adsorption methods. Appl. Clay Sci., 2011; 53: 20-26.

4.39) Acker, JG. and Bricker, OP.: The influence of pH on biotite dissolution and alternation kinetics at low temperature. Geochem. Cosmochim. Acta., 1992; 56: 3073-3092.

4.40) Chou, L. and Wollast, R.: Study of weathering of albite at room temperature and pressure with a fluidized bed reactor. Geochem. Cosmochim. Acta., 1984; 48: 2205-2217.

4.41) Helgeson, HC., Murphy, WM. and Aagaard, P.: Thermodynamic and kinetic constraints on reaction rates among minerals and aqueous solutions. II. Rate constants, effective surface area, and the hydrolysis of feldspar. Geochim. Cosmochim. Acta., 1984: 48: 2405–2432.

4.42) Hellman, R.: The albite-water system: Part I. The kinetics of dissolution as a function of pH at 100, 200, and 300°C. Geochim. Cosmochim. Acta., 1994; 58: 595–611.

4.43) Oelkers, EH. and Schott, J.: Experimental study of anorthite dissolution and the relative mechanism of feldspar hydrolysis. Geochim. Cosmochim. Acta., 1995; 59: 5039–5053.

4.44) Tester, JW., Worley, WG., Robinson, BA., Grigsby, CO. and Feerer, JL.: Correlating quartz dissolution kinetics in pure water from 25 to 625°C. Geochim. Cosmochim. Acta., 1994; 58: 2407–2420.

4.45) Palandri, JL. and Kharaka, YK.: A compilation of rate parameters of mineral-water interaction kinetics for application to geochemical modelling. US Geological Survey open file report, 2004: 2004–1068.

Chapter 5

Coupled Thermal-Hydraulic-Mechanical-Chemical Model Incorporating Pressure Dissolution with Dual Porosity Theory and Its Application to Long-term Flow Simulation of Fractured Rock

5.1 Overview

This chapter establishes a coupled THMC model that can describe the changes in permeability within both the matrix and the fracture domains of fractured rock by improving the previous models proposed in **Chapter 3** and **Chapter 4**.

Although many coupled THMC models have been developed[5.1) ~ 5.5)], almost none of them can satisfactorily evaluate the changes in the hydraulic property of the fractured rock surrounding high-level radioactive waste within geological disposal facility due to mineral reactions. In the existing models, the mineral dissolution and precipitation occurring on the free surface of the rock (i.e., free-face dissolution/precipitation)[5.6)] are typically considered, but the dissolution occurring at the grain contacts and the contacting asperities within the rock fractures (e.g., pressure dissolution) is not taken into account. Pressure dissolution at both the contacts and the contacting asperities within rock fractures is mineral dissolution; it depends on the ambient temperature and the stress conditions. It has been confirmed that the pressure dissolution may change the hydraulic property of porous and fractured rocks over a long duration[5.7)~5.10)]. Thus, a coupled THMC model has been developed here that considers the pressure dissolution at the grain contacts[5.11)]. However, this model does not consider the pressure dissolution at the contacting asperities within rock fractures. In previous research, it was indicated that rock permeability decreases by several orders of magnitude over several hundreds of hours due to pressure dissolution at the contacting asperities of rock fractures[5.12)~5.14)]; and therefore, this phenomenon should have a significant impact on the changes in hydraulic property in the fractured rocks.

In this chapter, a new coupled THMC model, that incorporates pressure dissolution both at the contacting asperities within the rock fractures and at the grain contacts, was developed. Subsequently, by using the developed model, the long-term evolution of the permeability in fractured rock near high-level radioactive waste within a geological disposal system was predicted and the influence of the pressure dissolution on the changes in permeability was closely examined.

5.2 Numerical model

5.2.1 Model description

The coupled THMC model developed in this chapter can describe the coupled thermal-hydraulic-mechanical-chemical processes in the near field, including the surrounding rock (i.e., interaction of heat radiation from the waste package, the movement of groundwater and mass transport with convection, the stress and deformation in the rock, and mineral dissolution/precipitation). In this model, porous rock including fractures is set as the target of the calculation, and the physical phenomena in the artificial barrier are not considered. The THMC interactions considered in this model are shown in **Fig. 5.**1. This model can describe the fully coupled THMC processes incorporating two-way interactions between H and M and T and M, which were not considered in previous model[5.11)] (introduced in **Chapter 3)**. Describing the changes in permeability within not only the rock matrix, but also the rock fractures due to the mineral reactions, is the significant difference from the previous model.

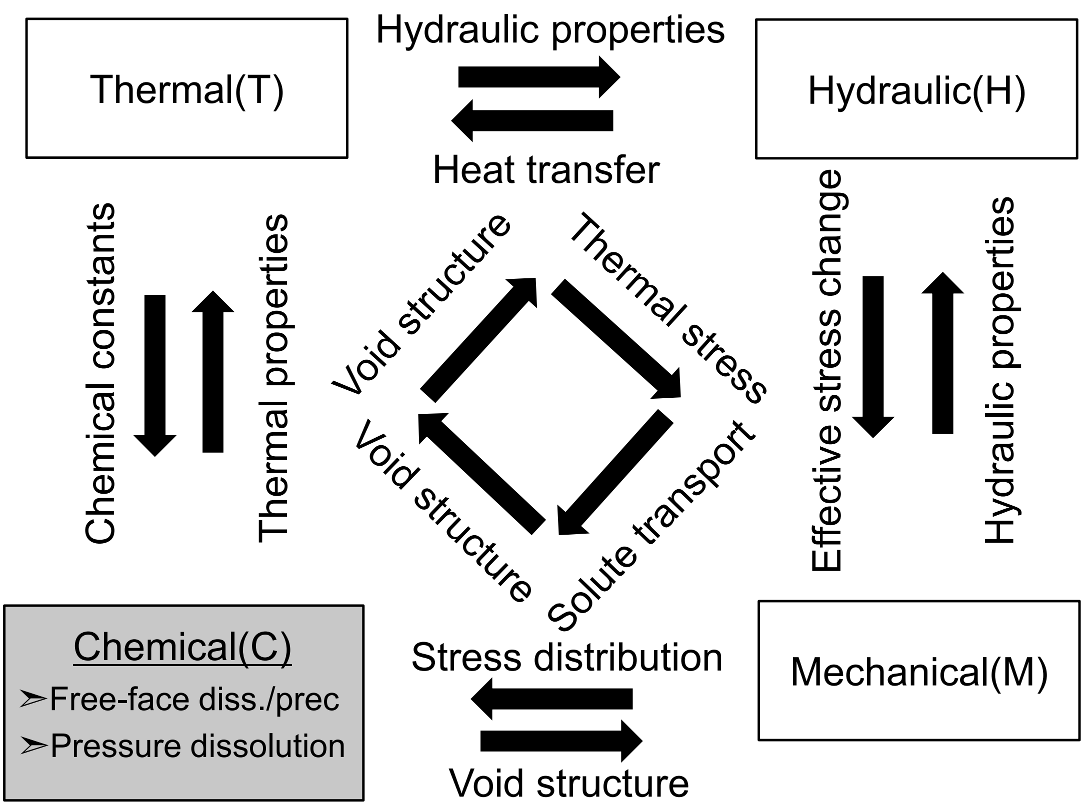

Fig. 5.1 THMC interactions considered in the developed model.

5.2.2 Governing equations

The calculation flow of the developed model is shown in **Fig. 5.2**. In this calculation, the coupled THMC behavior is described by solving the governing equations sequentially and exchanging the dependent variables (i.e., porosity, fracture aperture, permeability, flow velocity, stress, temperature, solute concentration, and dissolution/precipitation rate constants). In this chapter, the developed model is implemented and solved by COMSOL Multiphysics5.15). Details of the model will be given hereinafter.

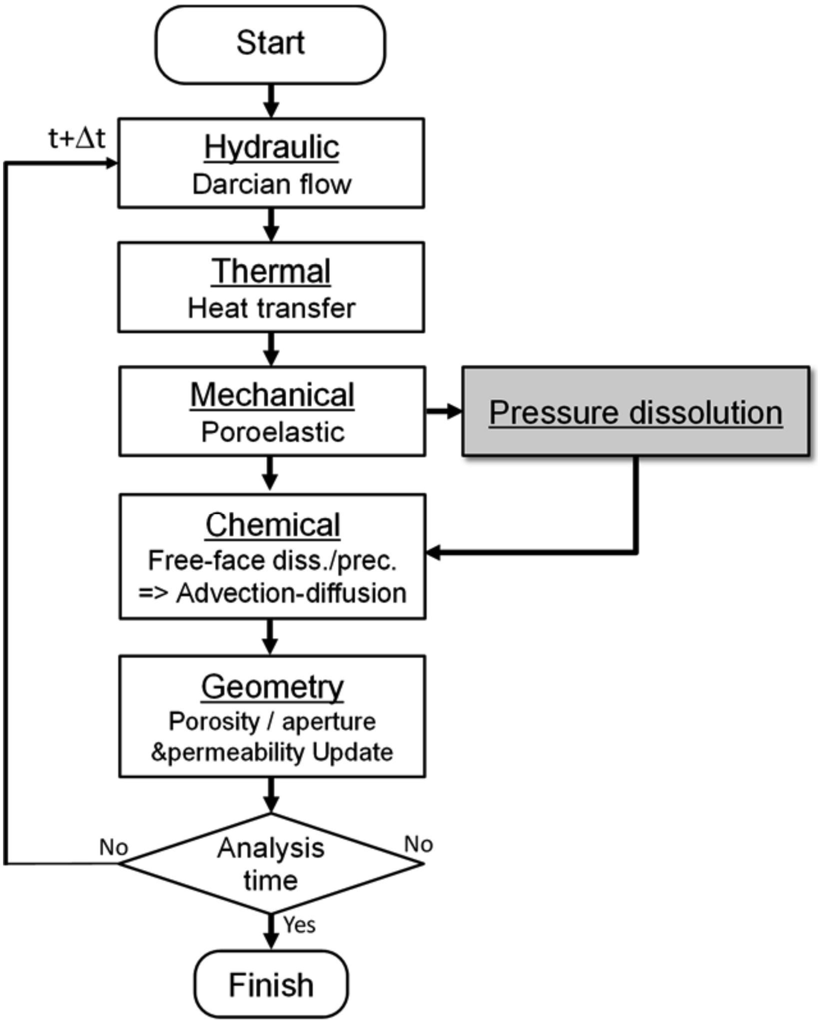

Fig. 5.2 Calculation flow.

(a) Fluid flow

The model assumes saturated porous rock indicating the behavior of the elastic body. The assumed porous rock has two different porosity systems of matrix and fractures. In order to calculate the fluid flow in this material, the dual porosity theory[5.16)] is applied. In this theory, the fluid flow in the two porosity systems is calculated by assuming virtual rock that includes the porosity of the matrix and the fractures, as shown in **Fig. 5.3**. In the proposed model, an extension of Biot's poroelastic theory to dual porosity is used. Eqs. (5.1) – (5.3) are Darcy's law and the conservation law of the water mass in the rock fractures and the rock matrix.

$$\rho_w S_f \frac{\partial p_f}{\partial t} + \nabla \cdot (\rho_w \boldsymbol{u}_f) + \rho_w \alpha_f \frac{\partial \varepsilon_v}{\partial t} = -f_w \tag{5.1}$$

$$\boldsymbol{u}_f = -\frac{\boldsymbol{k}_f}{\mu}(\nabla p_f + \rho_w g \nabla h) \tag{5.2}$$

$$\rho_w S_m \frac{\partial p_m}{\partial t} + \rho_w \alpha_m \frac{\partial \varepsilon_v}{\partial t} = f_w \tag{5.3}$$

where t [s] is time, ρ_w [kg m^{-3}] is the density of the fluid, $\boldsymbol{u}_f$ [m s^{-1}] is the fluid velocity tensor in the rock fractures, $\boldsymbol{k}_{f,m}$ [m^2] is the rock permeability tensor (indexes f and m represent the fractures and the matrix, respectively), $p_{f,m}$ [Pa] is the pore pressure for the fracture and the matrix domains, $S_{f,m}$ [Pa^{-1}] is the storage coefficient for the fracture and the matrix domains, $\alpha_{f,m}$ [-] is the Biot-Willis coefficient for the fracture and the matrix domains, μ [Pa s] is the fluid dynamic viscosity, g [m s^{-2}] is the gravity acceleration, h [m] is the potential head, ε_v [-] is volumetric strain, and f_w [kg m^{-3} s^{-1}] is the flow exchange term between the fracture and matrix.

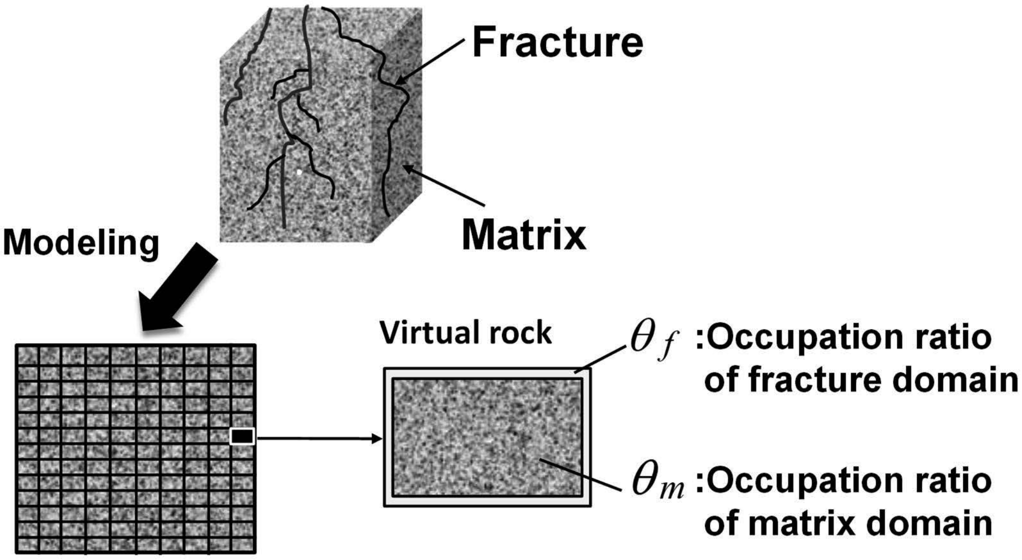

Fig. 5.3 Concept of dual porosity theory[5.16)].

The fluid velocity within porous rock that consists of the fractures and the matrix is calculated by multiplying each occupation ratio by the velocities within the fractures and the matrix, respectively.

$$\boldsymbol{u} = \theta_f \boldsymbol{u}_f + \theta_m \boldsymbol{u}_m \,, \tag{5.4}$$

where $\boldsymbol{u}$ [m s^{-1}] is fluid velocity within porous rock, and θ_f [-] and θ_m [-] are the occupation ratios of the fracture and the matrix domains, respectively.

(b) Stress analysis

In the mechanical process, the stress distribution of the rock structure is evaluated by the quasi-static equilibrium equation and the typical Hooke's law considering changes in pore pressure and thermal stress based on the poroelastic theory, given by

$$-\nabla \cdot \boldsymbol{\sigma} = \boldsymbol{F}_v \,, \tag{5.5}$$

$$\boldsymbol{\sigma} = \boldsymbol{E} : (\boldsymbol{\varepsilon} - \boldsymbol{\varepsilon}_{\boldsymbol{T}}) + \alpha p \boldsymbol{I} \,, \tag{5.6}$$

$$\alpha p = \alpha(\theta_f p_f + \theta_m p_m) \,, \tag{5.7}$$

where $\boldsymbol{\sigma}$ [Pa] is the stress tensor, $\boldsymbol{F}_v$ [Pa m^{-1}] is the body force, $\boldsymbol{E}$ [Pa] is the elasticity tensor, $\boldsymbol{\varepsilon}$ [-] is the strain tensor, $\boldsymbol{\varepsilon}_T$ [-] is the thermal strain tensor, α [-] is the Biot-Willis coefficient of porous rock, and $\boldsymbol{I}$ [-] is the identity tensor.

(c) Heat transfer

In the thermal process, the temperature of the rock is calculated by the following heat transfer equation:

$$(\rho C_p)_{eq} \frac{\partial T}{\partial t} + \rho_w C_{p,w} \boldsymbol{u} \cdot \nabla T = \nabla \cdot (\boldsymbol{\lambda}_{eq} \nabla T) + Q_h \,, \tag{5.8}$$

where T [K] is the system temperature, $(\rho C_p)_{eq}$ [J K^{-1} m^{-3}] is the equilibrium volumetric heat capacity, $C_{p,w}$ [J kg^{-1} K^{-1}] is the heat capacity of the fluid, $\boldsymbol{\lambda}_{eq}$ [W m^{-1} K^{-1}] is the equilibrium thermal conductivity tensor, and Q_h [W m^{-3}] is the heat source.

(d) Reactive transport

The reactive transport behavior is calculated by the basic advection-diffusion equation.

$$\frac{\partial(c_i \phi)}{\partial t} + \boldsymbol{u} \cdot \nabla c_i = \nabla \cdot (\boldsymbol{D}_{e,i} \nabla c_i) + r_i \,, \tag{5.9}$$

$$\boldsymbol{D}_{e,i} = \phi \tau \boldsymbol{D}_{b,i} \,, \tag{5.10}$$

$$r_i = \sum_{j}^{n} v_{i,j} R_j \,, \tag{5.11}$$

where c_i [mol m^{-3}] is the concentration of solute i in the pore water, ϕ [-] is the porosity, $\boldsymbol{D}_{e,i}$ [m^2 s^{-1}] is the effective diffusion coefficient tensor, τ [-] is the coefficient related to the tortuosity, $\boldsymbol{D}_{b,i}$ [m^2 s^{-1}] is diffusion coefficient tensor, r_i [mol m^{-3} s^{-1}] is the source term of solute i, $v_{i,j}$ [-] is the stoichiometry coefficient of solute i in reaction of mineral j, n is the number of minerals included in the targeted rock, and R_j [mol m^{-3} s^{-1}] is the rate of mineral reactions for mineral j.

(e) Mineral reactions in porous rock

In porous rock, mineral dissolution and precipitation occur at both fracture and matrix domains. Therefore, the mineral reactions of the free-face dissolution/precipitation and the pressure dissolution within both the rock fractures and the rock matrix are considered in the proposed model. Applying the dual porosity theory, the rate of the mineral reactions for mineral j, R_j, is given by considering the rates of the mineral reactions and the occupation ratios of the fracture and the matrix domains.

$$R_j = \theta_f R_{f,j} + \theta_m R_{m,j} \,, \tag{5.12}$$

where $R_{f,j}$ [mol m^{-3} s^{-1}] and $R_{m,j}$ [mol m^{-3} s^{-1}] are the rates of the mineral reactions of mineral j within the fracture and the matrix domains, respectively. The rates of the mineral reactions within the fracture and the matrix domains are defined by considering the rates of the free-face dissolution and the pressure dissolution within several domains.

$$R_{m,j} = R_{m,j}^{FF} + R_{m,j}^{PS}\,, \tag{5.13}$$

$$R_{f,j} = R_{f,j}^{FF} + R_{f,j}^{PS}\,, \tag{5.14}$$

where $R_{m,j}^{FF}$ [mol m^{-3} s^{-1}] is the rate of the free-face dissolution/precipitation of mineral *j* within the rock matrix, $R_{m,j}^{PS}$ [mol m^{-3} s^{-1}] is the rate of pressure dissolution of mineral *j* at the grain contacts within the rock matrix, $R_{f,j}^{FF}$ [mol m^{-3} s^{-1}] is the rate of the free-face dissolution/precipitation of mineral *j* within the rock fracture, and $R_{f,j}^{PS}$ [mol m^{-3} s^{-1}] is the rate of the pressure dissolution of mineral *j* at the contacting asperities within the rock fracture.

(f) Mineral reactions in rock matrix

In this chapter, the rock is assumed to be composed purely of quartz, and subscript *j* in Eqs. (5.11) - (5.14) is omitted hereinafter. The rate of the free-face dissolution/precipitation within the rock matrix is defined by[5.6)]

$$R_m^{FF} = f_r k_+ A_{geo} (a_{H^+})^q (1 - Q / K_{eq})\,, \tag{5.15}$$

where k_+ [mol m^{-2} s^{-1}] is the mineral dissolution rate constant, f_r [-] is the roughness factor, which is the ratio of the true (microscopic) surface area over the apparent (geometric) surface area, A_{geo} [m^2 m^{-3}] is the geometric specific surface area, a_{H+} [-] is the activity of H^+, q [-] is the constant, Q [-] is the ionic activity product, and K_{eq} [-] is the equilibrium constant. The rate of pressure dissolution at the grain contacts within the rock matrix is obtained by improving that of previous model[5.11)] (proposed in **Chapter 3)** to be able to consider the effective stress, given as follows:

$$R_m^{PS} = \frac{3\pi f_r V_m k_+ R_{m,c}}{4RTd} \left(\frac{\sigma'_m}{(12/\pi)(1-\phi_m) - 2} - \sigma_c \right), \tag{5.16}$$

where V_m [m^3 mol^{-1}] is the molar volume, σ_c [Pa] is the critical stress, d [m] is grain diameter, $R_{m,c}$ [-] is the contact-area ratio of the grain contacts, σ'_m [Pa] is the mean effective stress, ϕ_m [-] is the porosity of the matrix domain, and R [J mol^{-1} K^{-1}] is the gas constant.

(g) Permeability change in rock matrix

In previous model[5.11)] (proposed in **Chapter 3)**, the only influence of the mineral dissolution/precipitation is considered in the calculation of the porosity changes of the rock matrix. In the current model, however, the porosity changes are calculated by adding the influence of the mechanical elastic deformation to previous model[5.11)], given as

$$\phi_m(t) = \phi_{m,i} + \phi^M(t) + \phi^{FF}(t) + \phi^{PS}(t), \tag{5.17}$$

$$\phi^M(t_k) = \left(1 - \phi_m(t_{k-1})\right)\varepsilon_v, \tag{5.18}$$

where $\phi_m(t)$ [-] is the porosity of the matrix domain at arbitrary time t, $\phi_{m,i}$ [-] is the initial porosity of the matrix domain, ϕ^M [-] is the porosity change due to mechanical deformation at arbitrary time t , $\phi^{FF}(t)$ [-] is the porosity change due to the free-face dissolution/precipitation within the rock matrix until arbitrary time t, $\phi^{PS}(t)$ [-] is the porosity change due to the pressure dissolution/precipitation at the grain contacts within the rock matrix until arbitrary time t, and $\phi_m(t_{k-1})$ [-] is the porosity of the matrix domain at the time steps before one. The permeability changes due to the porosity changes are calculated by the Kozeny-Carman equation[5.17)] as

$$k_r = \frac{k_m(t)}{k_{m,i}} = \frac{(1-\phi_{m,i})^2}{(1-\phi_m(t))^2}\left(\frac{\phi_m(t)}{\phi_{m,i}}\right)^3, \tag{5.19}$$

where k_r [m^2] is the related permeability, $k_m(t)$ [m^2] is the permeability within the rock matrix at an arbitrary time t, and $k_{m,i}$ [m^2] is the initial permeability within the matrix.

(h) Mineral reactions in rock fractures

As shown in **Fig. 5.**4, when the geometric model obtained by idealizing the arbitrary micro-domain composed of contacting asperities and the pore space is set as the representative element of the rock fractures[5.12)], with reference to the model[5.18)] proposed in **Chapter 4**, the rate of the free-face dissolution/precipitation within the rock fracture is defined by

$$R_f^{FF} = 2 f_r k_+ (1 - Q / K_{eq}) / b , \tag{5.20}$$

where b [m] is the average mechanical fracture aperture.

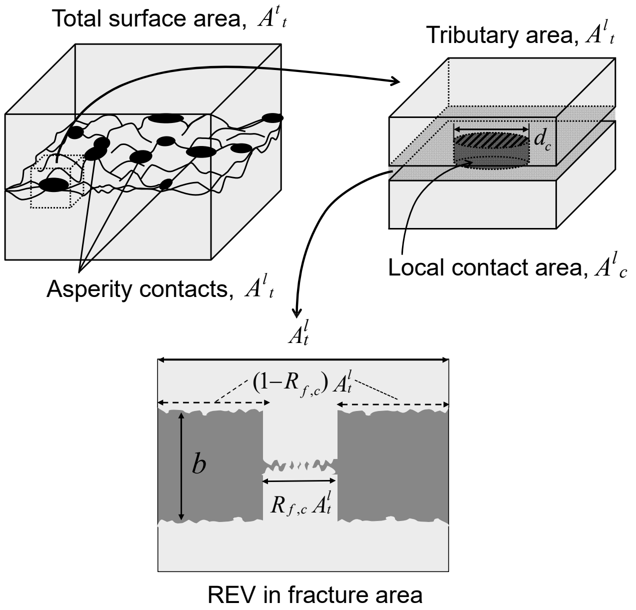

Fig. 5.4 Geometrical model that includes representative element in the rock fracture area[5.12)].

Within the rock fractures, pressure dissolution may occur at the contacting asperities (fracture contacts), as shown in **Fig. 5.4**. The way to estimate the rate of pressure dissolution at the contacts within the rock fractures is same as for the model[5.18)] introduced in **Chapter 4**; the rate of pressure dissolution at the contacting asperities within the rock fracture is defined by

$$R_f^{PS} = \frac{3 f_r V_m k_+ R_{f,c}}{RTb(1 - R_{f,c})} \left(\frac{\sigma'_m}{R_{f,c}} - \sigma_c \right) , \tag{5.21}$$

$$R_{f,c} = \frac{A_c^l}{A_t^l} , \tag{5.22}$$

where $R_{f,c}$ [-] is the contact-area ratio within the fracture, A_t^l [m^2] is the total fracture cross-sectional area in the representative element, and A_c^l [m^2] is the contact area within the fracture of the representative element $A_c^l = R_{f,c} A_t^l$.

Mineral reactions alter the fracture aperture, and the contact-area ratio within the fracture changes due to the changes in the fracture aperture. The relation between the fracture aperture and the contact-area ratio within the fracture may be given by the following simple equation$^{5.12)}$:

$$b = b_r + (b_0 - b_r)\exp(-(R_{f,c} - R_{f,c0})/a), \tag{5.23}$$

where b_r [m] is the residual fracture aperture, b_0 [m] is the initial fracture aperture, $R_{f,c0}$ [-] is the initial contact-area ratio within the fracture, and a [-] is a constant.

(i) Permeability change in rock fractures

In the proposed model, changes in the fracture aperture are only induced by the mineral reactions of both the free-face dissolution/precipitation and the pressure dissolution. The rate of aperture change due to the free-face dissolution/precipitation and the pressure dissolution in the rock fracture is defined as follows:

$$b(t) = b_0 + b^{FF}(t) + b^{PS}(t), \tag{5.24}$$

$$b^{FF}(t) = \int 2 f_r k_+ (1 - R_{f,c}) V_m (1 - Q / K_{eq}) dt, \tag{5.25}$$

$$b^{PS}(t) = \int \frac{-3 f_r V_m^2 k_+}{RT} \left(\frac{\sigma'_m}{R_{f,c}} - \sigma_c \right) dt, \tag{5.26}$$

where $b(t)$ is the average mechanical fracture aperture at an arbitrary time t, $\dot{b}^{FF}$ [m s^{-1}] is the rate of change in fracture aperture by the free-face dissolution/precipitation, and $\dot{b}^{PS}$ [m s^{-1}] is the rate of change in fracture aperture by pressure dissolution. The changes in permeability within the rock fractures are calculated by the following equation. In the proposed model, it is assumed that mechanical fracture aperture is equivalent to hydraulic fracture aperture.

$$k_f(t) = \frac{b(t)^2}{12}\,. \tag{5.27}$$

5.3 Numerical analysis

The long-term predictions of the permeability in the rock near radioactive waste within a geological disposal system of high-level radioactive waste were conducted using the developed THMC model. It should be noted that although actual data from related literature were used in the following predictions, no specific sites for high-level radioactive waste repositories were anticipated. The horizontal storage of radioactive waste, shown in the scientific and technical report summarizing HLW disposal construction in Japan[5.19)], was assumed in the modeling. As shown in **Fig. 5.5**, bedrock from the ground surface to 700 m below the surface, with a disposal cavity having a depth of 450 m, was set as the calculation domain[5.20)]. The canisters of radioactive waste were virtually installed in the cavity as a heat source . The 3D domain for the calculations was set by assuming that the diameter of the cavity, the clearances of the cavities, and the canisters would be 2.0, 12.2, and 3.13 m, respectively. The targeted rock with an initial porosity of 0.4 and a dry density 1700 kg/m^3 was assumed to be composed of purely quartz[5.21)]. The hydraulic and thermal gradients were set to be 1/1000 and 5°C/100m, respectively[5.22)]. The surface temperature was fixed at 15°C. In this calculation, the Excavation Damaged Zone (EDZ) was considered with reference to the technical report[5.19)]. The report[5.19)] indicates that micro cracks would be generated in the range of roughly 1.0 m in the radial direction from the wall of the cavity and that the rock permeability might increase to several orders of magnitude greater than that of the intact rocks. Therefore, the range of 0.8 m from the wall of the cavity was set as the EDZ, and the other domain was assumed to be intact in the calculation (**Fig. 5.5**). The initial permeability in the EDZ was set to be two orders of magnitude

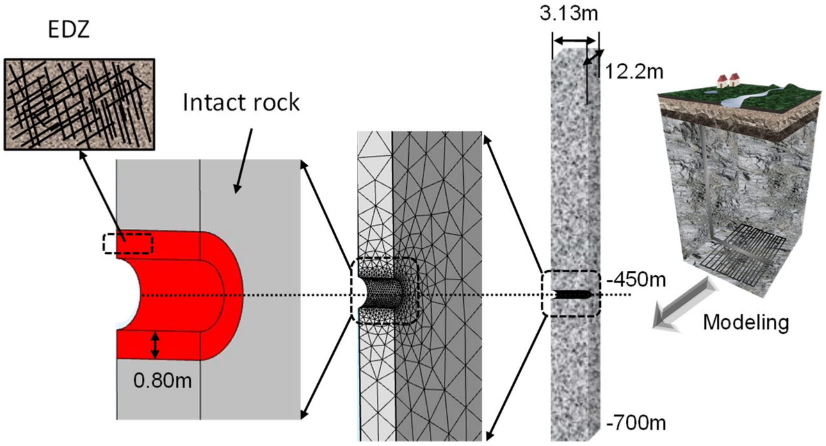

Fig. 5.5 Calculation domain.

greater than that of the intact rock. As described above, the dual porosity theory was applied to the current model and was utilized only for the EDZ because it contains both the matrix and the fractures. 1.0 and 99 vol.% of the EDZ were assumed to be fractures with an initial aperture of 11 μm and a matrix with the initial porosity of 0.4, respectively. In the intact rock zone, by assuming that few fractures exist and that the zone is only composed of the matrix, the basic single porosity theory was applied. In this analysis, as mentioned above, although the existence of fractures induced by the cavity excavation was considered implicitly, fractures that existed before the cavity excavation were not be taken into account. The prediction period was set at 10^3 years. Considering the heat radiation from the canisters containing radioactive waste, the time-dependent temperature change (same as shown in **Fig. 3.7**) outside the buffer material can be obtained from the literature[5.19)]. In this analysis, the temperature change was prescribed at the boundary of the cavity as a boundary condition. In calculating the heat transfer, the following Neumann's boundary condition is set at all the boundaries excluding the periphery of the cavity:

$$\frac{\partial T}{\partial \boldsymbol{n}} = 0 , \tag{5.28}$$

where ***n*** represents the outward normal direction to the targeted boundary. In the calculation of the reactive transport, the following Neumann's boundary condition is set at all the boundaries of the calculation domain:

$$\frac{\partial c_i}{\partial \boldsymbol{n}} = 0 . \tag{5.29}$$

In the mechanical calculation, a self-weight analysis was conducted considering the stress redistribution due to the cavity excavation. The lateral earth pressure coefficients were set to be 0.5 from the ground surface to 200 m depth and 1.0 deeper than 200 m depth[5.23)]. The parameters used in calculations are summarized in **Table 5.1**.

Table 5.1 Parameters used in calculation[5.20)~5.22)].

Parameter	EDZ	Intact rock
Young's modulus [GPa]	2.5	2.5
Poisson's ratio [-]	0.3	0.3
Initial permeability [m^2]	1.0×10^{-13}	1.0×10^{-15}
Initial porosity [-]	0.4	0.4
Initial fracture aperture [μm]	11	-
Matrix occupation ratio [%]	99	100
Fracture occupation ratio [%]	1.0	0

5.4 Analysis results

5.4.1 Long-term evolution of permeability

Changes in the distribution of the mean effective stress within 10^3 years after the cavity excavation are shown in **Fig. 5.6**. In our calculation, the mean effective stress is an important parameter because it is the driving force in the pressure dissolution. As is apparent from the figure, the mean effective stress on the cavity wall and around the cavity boundary is greater than in the other areas. Moreover, the temporal change in the mean effective stress is quite small; and thus, the influence of the thermal stress and the pore pressure changes after the cavity excavation on the mean effective stress should be small.

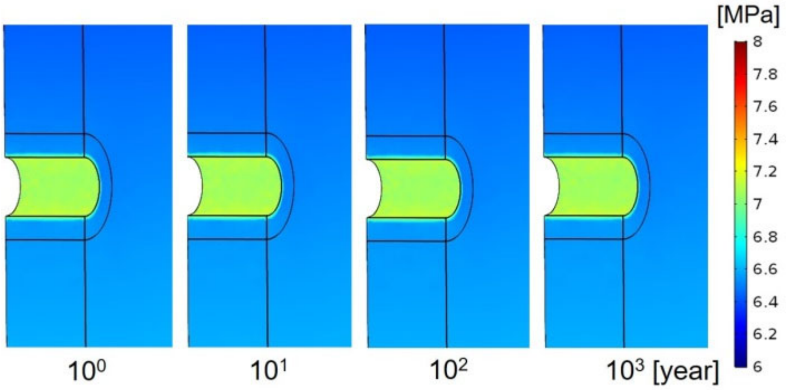

Fig. 5.6 Evolution of mean effective stress after cavity excavation.

In this section, a comparison of the predicted results for the changes in rock permeability between two different cases was conducted. One case was done by considering the full THMC processes with pressure dissolution, which is called the “PS condition” (including both pressure dissolution and free-face dissolution in the mineral reactions). The other case was done by excluding the process of pressure dissolution, which is called the “No-PS condition” (including only free-face dissolution in the mineral reactions). The changes in permeability with time around the cavity under the No PS condition and the PS condition are depicted in **Fig. 5.7**. In the figure, the permeability is shown by a log notation (i.e., $\log_{10}k$). As is apparent from the figure, it does not change with time under the No PS condition. Therefore, it is implied that the influence of the free-face dissolution on the rock permeability is negligibly small. The hydraulic gradient is assumed to be 1/1000 at a depth of 450 m and the maximum ground water velocity is less than 1.0×10^{-12} m/s. Consequently, the ground water movement becomes significantly slow, which diminishes or even invalidates the effect of the free-face dissolution/precipitation - the dissolved minerals within the pore spaces should precipitate extremely close to the locations where the minerals dissolved, and the material concentrations in the pore spaces and the porosity should be kept constant with time. In contrast, the permeability decreases with time under the PS condition. Specifically, the reduction is significant within the EDZ. This is because the pressure dissolution, resulting in a reduction in porosity and fracture aperture, is enhanced by the increase in the mean effective stress induced by the cavity excavation (see **Fig. 5.6**), and an additional reduction in porosity and aperture is caused by the precipitation at the free surface resulting from the supply of dissolved silica through the pressure dissolution. The permeability of the EDZ decreases to that of the intact rock zone in 10^2 years. As the pressure dissolution within the fractures is considered only in the EDZ, among the two types of pressure dissolution within fractures and the matrix, especially that within the fractures should have a remarkable influence on the permeability reduction.

(a) No PS condition

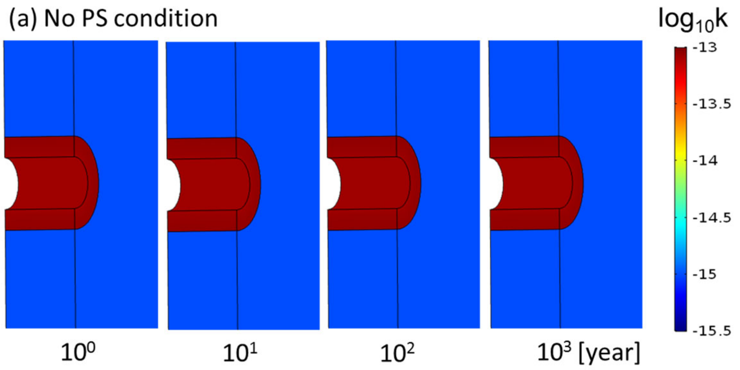

(b) PS condition

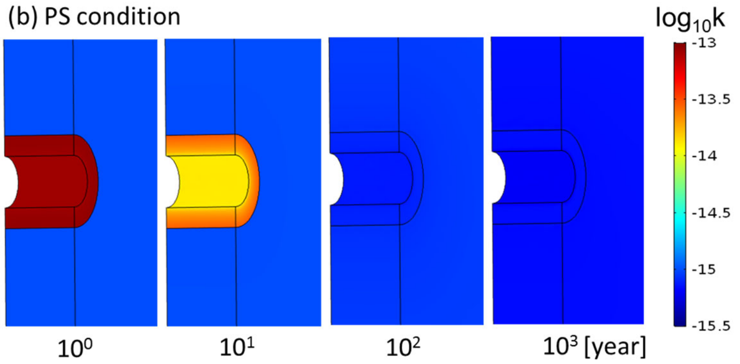

Fig. 5.7 Evolution of permeability with time under (a) the no PS condition and (b) the PS condition.

In order to further investigate the changes in permeability in the surrounding rock, the changes with time at two measurement points, shown in **Fig. 5.8**, are depicted in **Fig. 5.9**. One measurement point (Point 1) is located on the periphery of the cavity, and the other point (Point 2) is located 5.1 m away from the periphery of the cavity. In order to separately evaluate the influence of the pressure dissolution active at the contacting asperities within the fractures and that at the grain contacts within the matrix, a comparison of the permeability changes between the No-PS condition and the PS condition was conducted (**Fig. 5.9**). In the PS condition, the case that considers pressure dissolution within both the fractures and the matrix is expressed as “PS (Matrix & Fracture)” in **Fig. 5.9**. The permeability decreases by about two orders of magnitude after approximately 18 years from the initial state, and it approaches that of the intact rock zone that is similar to the permeability at Point 2 expressed as “PS (Intact rock)” in **Fig. 5.9**. After 18 years, the rate of permeability reduction drastically decreases and the permeability decreases by 4.0×10^{-16} m^2, that is 40% of the value at 18 years. In the case that considers only the pressure dissolution within the matrix, expressed as "PS (Only Matrix)" in **Fig. 5.9**, it decreases by only 4.0×10^{-14} m^2, that is 40% of the initial value at 10^3 years. These results indicate that the significant reduction in permeability within the EDZ during 18 years is attributed to the compaction of fractures resulting from the pressure dissolution at the fracture contacts, and the following gradual reduction is due to the porosity reduction induced by the pressure dissolution at the grain contacts within the matrix. The pressure dissolution at the contacting asperities within the fractures should have a significant impact on the changes in permeability within the EDZ.

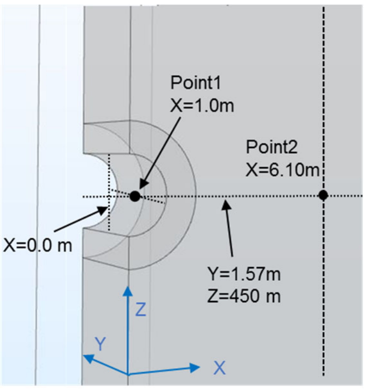

Fig. 5.8 Measurement points.

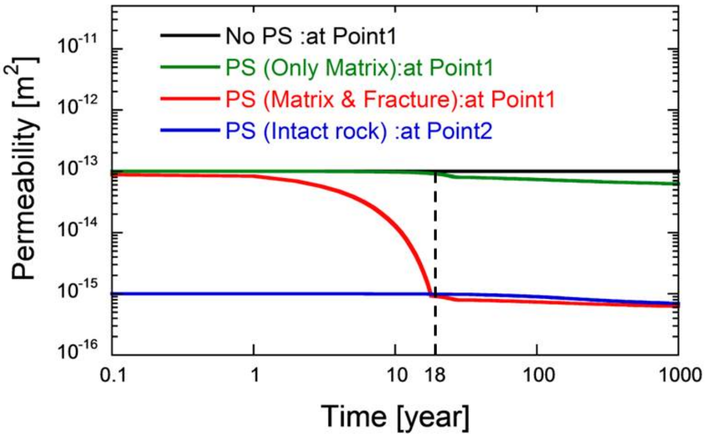

Fig. 5.9 Permeability changes with time at measurement points in No PS and various PS conditions.

5.4.2 Parametric study

As a parametric study, predictions are conducted by varying the parameters of *a* that should control the rate of pressure dissolution at the fracture contacts (see Eq. (5.23)) to investigate the influence on the changes in rock permeability. The values for parameter *a* can be obtained from the relationship between the fracture aperture and the contact area ratio that may be evaluated by utilizing the roughness measurements of the fracture surfaces. In the work of this chapter, the roughness data of the targeted rock were not measured, and parameter *a* is unknown. Therefore, calculations were conducted using three different values for *a* – one is 0.07 used in Yasuhara and Elsworth[5.12)], and the others are set to be 0.12 and 0.17. The predicted changes in permeability using the three different values for *a*, under the conditions that consider the pressure dissolution within both the fractures and the matrix, are shown in **Fig. 5.10**. Firstly, the permeability decreases by two orders of magnitude due to the pressure dissolution and, after that, it approaches a stable state. The three cases are almost equivalent for the convergence values, but it is obvious that when higher values for *a* are applied, the rate of permeability reduction is lower. A comparison between the cases of a = 0.07 and 0.17 shows that, in the case of a = 0.17, the convergence time is roughly 30 years slower than the case of a = 0.07. Therefore, the decrease in permeability induced by the pressure dissolution at the fracture contacts is greatly dependent on the relationship between the aperture and the contact-area ratio and it is apparent that the setting of parameter *a* is important to accurately predicting changes in permeability.

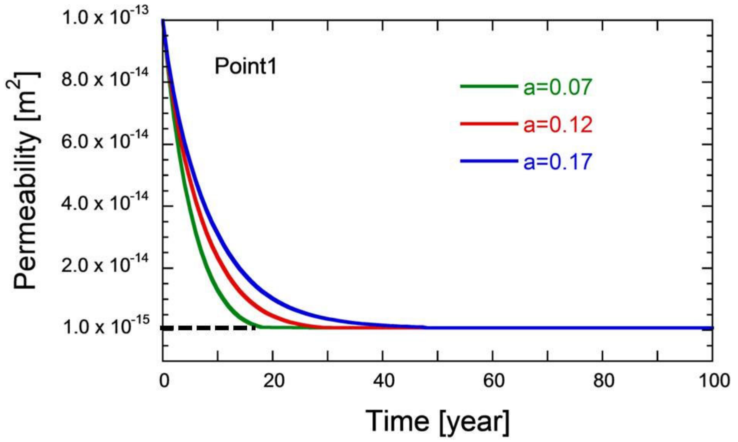

Fig. 5.10 Permeability changes with time at measurement Point 1 with different values for *a* = 0.07, 0.12, and 0.17 used in Eq. (5.23).

5.5 Summary

In this chapter, a coupled THMC model that enables the evaluation of the changes in rock permeability within both the matrix and the fracture domains, incorporating the pressure dissolution within both the grain contacts and the fracture contacts, was developed. Long-term predictions of the permeability in the rock near high-level radioactive waste were conducted by the developed model. In order to separately examine the influences of the pressure dissolution within the rock matrix and the rock fractures, a comparison was conducted of the permeability changes between the No-PS condition (not including pressure dissolution) and the PS conditions - PS (Matrix & Fracture) including pressure dissolution within matrix/fractures and PS (Only Matrix) including only pressure dissolution within matrix). Under the subsurface conditions expected in this chapter, predictions confirmed that the rock permeability of the EDZ eventually decreased to that of the intact rock during the geological disposal period due to the pressure dissolution within the rock fractures. Thus, the pressure dissolution within the fractures should have a significant impact on the changes in rock permeability of the dual porosity media of the EDZ that contains both the matrix and the fractures.

As a parametric study, predictions were made by changing parameter a that should control the relationship between the fracture aperture and the contact area ratio (see Eq. (5.23)) for evaluating the influence on evolution of the rock permeability. Consequently, it was indicated that parameter a has a significant impact on the permeability reduction in fractured rock and that its setting is of importance to accurately predicting changes in permeability.

References

5.1) Nasir, O., Fall, M. and Evgin, E.: A simulator for modeling of porosity and permeability changes in near field sedimentary host rocks for nuclear waste under climate changes influences. Tunneling and Underground Space Technology, 2014; 42: 122-135.

5.2) Fall, M., Nasir, O. and Nguyen, TS.: A coupled hydro-mechanical model for simulation of gas migration in host sedimentary rocks for waste repositories. Eng. Geol., 2014; 176: 24-44.

5.3) Zhang, R., Yin, X., Winterfeld, PH. and Wu, YS.: A fully coupled thermal-hydrological-chemical model for CO_2 geological sequestration. J. Nat. Gas Sci. Eng., 2016; 28: 280-304.

5.4) Liu, Y., Ma, L., Ke, D., Cao, S., Xie, J., Zhao, X., Chen, L. and Zhang, P.: Design and validation of the THMC China-Mock-Up test on buffer material for HLW disposal. J. Rock Mech. Geotech. Eng., 2014; 6: 119-125.

5.5) Danko, G. and Bahrami, D.: A new T-H-M-C model development for discrete-fracture EGS studies. Geothermal Resources Council Transactions, 2012; 36: 383-392.

5.6) Lasaga, AC.: Chemical kinetics of water-rock interactions. J. Geophys. Res., 1984; 89: 4009-4025.

5.7) Elias, BP. and Hajash, A.: Change in quartz solubility and porosity change due to effective stress: An experimental investigation of pressure solution. Geology, 1992; 20: 451-454.

5.8) Polak, A., Elsworth, D., Yasuhara, H., Grader, A. and Halleck, P.: Permeability reduction of a natural fracture under net dissolution by hydrothermal fluids. Geophys. Res. Lett., 2003; 30(20): 2020, doi:10.1029/2003 GL017575.

5.9) Polak, A., Elsworth, D., Yasuhara, H., Grader, AS. and Halleck, PM.: Spontaneous switching of permeability changes in a limestone fracture with net dissolution. Water Resour. Res., 2004; 40, W03502, doi:10.1029/ 2003WR002717.

5.10) Yasuhara, H., Elsworth, D. and Polak, A.: A mechanistic model for compaction of granular aggregates moderated by pressure solution. J. Geophys. Res., 2003; 108(11):2530, doi:10.1029/2003JB002536.

5.11) Yasuhara, H., Kinoshita, N., Ogata, S., Cheon, DS. and Kishida, K.: Coupled thermal-hydro-mechanical-chemical modeling by incorporating pressure solution for estimating the evolution of rock permeability. Int. J. Rock Mech. Min. Sci., 2016; 86: 104-114.

5.12) Yasuhara, H., Elsworth, D. and Polak, A.: Evolution of permeability in a natural fracture: the significant role of pressure solution, J. Geophys. Res., 2004; 109, B03204, doi:10.1029/2003JB002663.

5.13) Yasuhara, H., Kinoshita, N., Ohfuji, H., Lee, DS., Nakashima, S. and Kishida, K.: Temporal alteration of fracture permeability in granite under hydrothermal conditions and its interpretation by coupled chemo-mechanical model. Appl. Geochem., 2011; 26: 2074-2088.

5.14) Yasuhara, H. and Elsworth, D.: A numerical model simulating reactive transport and evolution of fracture permeability. Int. J. Numer. Anal. Methods Geomech., 2006; 30: 1039-1062.

5.15) COMSOL2014：COMSOL MULTIPHYSICS. Version 5.0, Available from www.comsol.com.

5.16) Barenblatt, GI., Zheltov, IP. and Kochina, IN.: Basic concepts in the theory of seepage of homogeneous liquids in fissured rocks. J. Appl. Math. Mech., 1960; 24(5): 1286-1303.

5.17) Bear, J.: Dynamics of Fluids in Porous Media. Dover Publications, 1972; 1-166.

5.18) Ogata, S., Yasuhara, H., Kinoshita, N., Cheon, DS. and Kishida, K.: Modeling of coupled thermal-hydraulic-mechanical-chemical process for predicting the evolution in permeability and reactive transport behavior within single rock fractures. , Int. J. Rock Mech. Min. Sci., 2018; 107: 271-281.

5.19) Japan Nuclear Cycle Development Institute, 2000: Second Progress Report on Research and Development for the Geological Disposal of HLW in Japan, Supporting Report 2 Repository Design and Engineering Technology, H12: Project to Establish the Scientific and Technical Basis for HLW Disposal in Japan. JNC TN1410 2000-003, IV-139-IV-160.

5.20) Suzuki, H., Nakama, S., Fujita, T., Imai, H. and Sazarshi, M.: A long-term THMC assessment on the geochemical behavior of the bentonite buffer. J. Nucl. Fuel Cycle Environ., 2012; 19:39-50.

5.21) Miyazawa, D., Sanada, H., Kiyama, T., Sugita, Y. and Ishijima, Y.: Poroelastic coefficients for siliceous rocks distributed in the Horonobe area, Hokkaido, Japan. J. MMIJ, 2011; 127:132-38.

5.22) JNC (Japan Nuclear Cycle Development Institute), 2005: Development and management of the technical knowledge base for the geological disposal of HLW, Summary of the H17 project reports, Vol. 1. Scientific research of deep underground. JNC TN1400 2005-014.

5.23) Hoek, E., Kiser., PK. and Bawden, WF.: Support underground excavation in hard rock. 1993: 1-235.

Chapter 6

Coupled Thermal-Hydraulic-Mechanical-Chemical Analyses for Fractured Rock by Incorporating Damage Theory

6.1 Overview

This chapter introduces a new coupled THMC model by adding the processes of fracture generation to predict the long-term evolution of permeability within rock fractures in more detail.

From previous works$^{6.1)\sim6.8)}$, it is well known that fracture initiation and propagation within rock masses during the excavation of a disposal cavity for radioactive waste should cause an increase in permeability and a decrease in stiffness and strength of the rock masses near the disposal cavity. The area where these changes in the mechanical and hydraulic properties occur is called the Excavation Damaged Zone (EDZ), as introduced previously in **Chapter 5**. In addition, the mineral reactions of the free-face dissolution/precipitation at the free surface and the pressure dissolution at the contacting asperities within the rock fractures occur due to the cavity excavation and they may alter the rock permeability over time$^{6.9),6.10)}$. Previous works$^{6.11)\sim6.13)}$ confirm that pressure dissolution at the contacting asperities within the fractures may change the permeability of the fractured rocks by several orders of magnitude over a long duration. Thus, developing a coupled model that can evaluate the mineral reactions within the rock fractures that may be newly generated by the cavity excavation is required for predicting the long-term evolution of the hydraulic property of the natural barrier. To date, several coupled THMC models have been developed$^{6.14)\sim6.19)}$. Recently, other coupled models have been developed that can consider the changes in the physical properties such as the mechanical and hydraulic properties of rock masses due to fracture generation [6.5),6.20)~6.25)]. For example, Wei et al.[6.20)] and Li et al.[6.21)] developed a coupled thermal-hydraulic model that can describe the fracture propagation by utilizing the damage theory, including the heterogeneity of the mechanical property of the rock and the changes in the thermal property of the rock. They then, evaluated the evolution of the EDZ and the mechanical property of the rock under high-temperature and high-confining pressure conditions. As mentioned above, although many coupled models have been developed, they cannot describe the process of the mineral dissolution/precipitation within the newly initiated and propagated fractures. Currently, therefore, it is difficult to predict the changes in rock permeability over time by the influence of the mineral reactions in detail.

In this chapter, a coupled THMC model was proposed, including the fracture initiation and propagation, by incorporating the damage theory and the process of mineral dissolution/precipitation (i.e., pressure dissolution and free-face dissolution/precipitation) within the generated fractures. Then, the developed model, incorporating the damage theory, was validated by replicating the uniaxial compression test using the granite specimen. Finally, predictions of the long-term evolution of the rock permeability in geological disposal facilities of high-level radioactive waste were made.

6.2 Numerical model

6.2.1 Model description

The coupled THMC model developed in this chapter can describe the interactions of the thermal, hydraulic, mechanical, and chemical processes (i.e., heat transfer from the waste package, the mass transport with the fluid flow, the fracture initiation/propagation within the rocks due to the stress redistribution induced by the cavity excavation for disposing radioactive waste, and the dissolution and precipitation of the rock minerals in pore water). In this model, porous rock that works as a natural barrier is set as the target of the calculation and the physical phenomena in the artificial barrier are not considered. In this model, as shown in **Fig. 6.1**, the interactions of the multi-components were considered by adding the D (damage) component to the interactions between the T, H, M, and C components. This model can describe the damage (fracture initiation/propagation) and the changes in the thermal, hydraulic, mechanical, and chemical properties of the rock due to the damage (expressed as gray arrows in **Fig. 6.1**), which were not considered in previous model[6.26)] introduced in **Chapter 5** (the interactions shown as white arrows in **Fig. 6.1** are taken into account). In particular, being able to describe the mineral reactions within the generated fractures as well as the subsequent permeability changes is the important characteristic of this model.

6.2.2 Governing equations

The calculation flow of the proposed model is shown in **Fig. 6.2**. This model considers the ground water flow, heat transfer, stress and deformation, fracture initiation/propagation, reactive transport, and mineral reactions. These phenomena are described by utilizing the governing equations, including the fluid flow equation of Darcy's law and the conservation law of water mass, the heat transfer equation, the poroelastic theory, the damage theory, the reactive transport equation, and the law of mineral reactions. In this chapter, COMSOL Multiphysics[6.27)] is utilized to solve the differential equations of the developed model. In the following, the governing equations used in the proposed model are introduced.

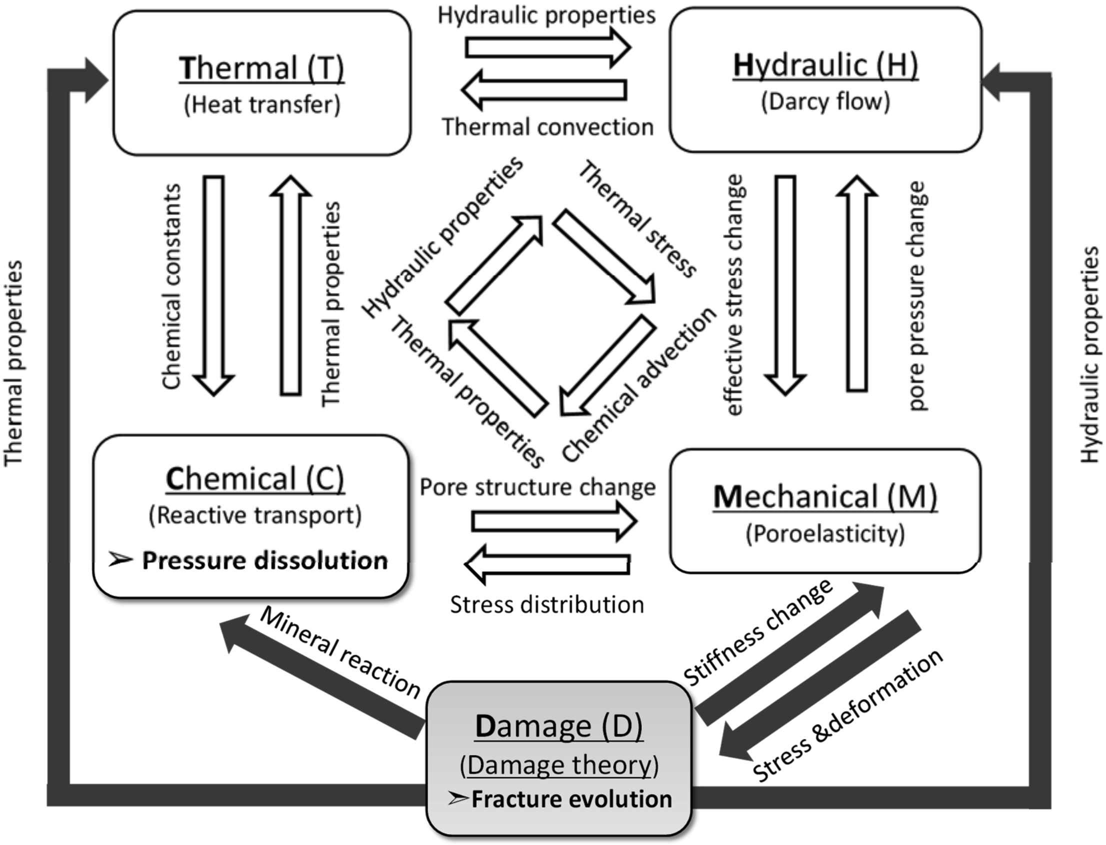

Fig. 6.1 THMC interactions considered in the developed model. The interactions expressed as gray arrows were not considered in previous model[6.26)] introduced in **Chapter 5**, while the ones expressed as white arrows were taken into account.

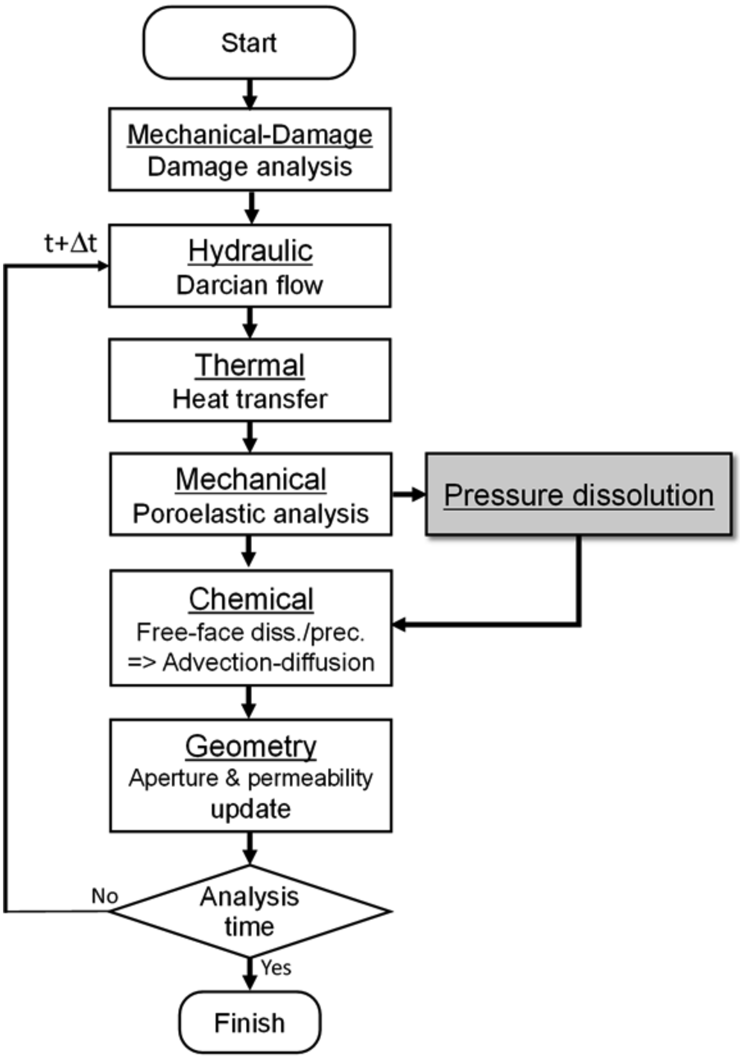

Fig. 6.2 Calculation flow.

(a) Stress analysis

In the mechanical process, assuming the plane strain condition, the stress distribution of the rock structure is evaluated by the quasi-static equilibrium equation and the typical Hooke's law considering the changes in pore pressure and thermal stress based on the poroelastic theory, given by

$$-\nabla \cdot \boldsymbol{\sigma} = \boldsymbol{F_v}\,, \tag{6.1}$$

$$\boldsymbol{\sigma} = \boldsymbol{E} : (\varepsilon - \varepsilon_T) + \alpha_B p \boldsymbol{I}\,, \tag{6.2}$$

where $\boldsymbol{\sigma}$ [Pa] is the stress tensor, $\boldsymbol{F_v}$ [Pa m^{-1}] is the body force, $\boldsymbol{E}$ [Pa] is the elasticity tensor, p

[Pa] is the pore pressure, $\boldsymbol{\varepsilon}$ [-] is the strain tensor, $\boldsymbol{\varepsilon}_T$ [-] is the thermal strain tensor, α_B [-] is the Biot-Willis coefficient, and $\boldsymbol{I}$ [-] is the identity tensor.

(b) Damage theory

The isotropic damage theory is used for calculating the behavior of the rock fracture initiation and propagation. The damage theory defines a fracture as not discontinuous deformation, but the decrease in stiffness of the continuum. As this theory can consider the fracture as a continuum, it is compatible with the FEM and has high versatility and extensibility. Thus, it has been used in a number of calculations for fracture initiation/propagation$^{6.20)\sim6.23),\ 6.28)\sim6.33)}$. In the model, tensile damage or shear damage occurs when the stress condition of the rock satisfies the following maximum tensile stress criterion or the Mohr-Coulomb criterion, respectively$^{6.20),6.22),6.28),6.30),6.31)}$. In this chapter, the tensile stress and the compressive stress are set to be negative stress and positive stress, respectively.

$$\begin{cases} F_1 \equiv -\sigma_3 - f_{t0} = 0 \\ F_2 \equiv \sigma_1 - \dfrac{1+\sin\theta}{1-\sin\theta}\sigma_3 - f_{c0} = 0 \end{cases} , \tag{6.3}$$

where F_1 and F_2 are the two damage threshold functions for tensile damage and shear damage, respectively, σ_1 [Pa] and σ_3 [Pa] are the maximum and minimum principal stresses, respectively, f_{t0} [Pa] and f_{c0} [Pa] are the uniaxial tensile strength and compressive strength, respectively, and θ [°] is the internal friction angle. In the isotropic damage theory, the elastic modulus E of the damaged rock monotonically decreases with the evolution of damage, given as

$$E = (1-D)E_0, \tag{6.4}$$

where E_0 [Pa] and E [Pa] are the elastic modulus of the rock before and after the initiation of damage, respectively, and D [-] is the scalar damage variable that varies from 0 to 1 and represents the degree of damage to the targeted material. D becomes 0 when damage does not occur and 1 when complete damage occurs. The model assumes that fracture occurs when D>0. In general, damage variable D is calculated by the induced strain[6.34)]. In the proposed model, D is evaluated by strain as follows[6.31)]. In the linear elastic law, principle stress σ_i is expressed by the principle strain and the volumetric strain, as follows:

$$\sigma_i = \frac{E}{1+v}\left[\varepsilon_i + \frac{v}{1-2v}\varepsilon_v\right], \tag{6.5}$$

where ε_i (i = 1, 2, 3) are principle strains in the first, second, and third principal stress directions, respectively, ε_v [-] is the volumetric strain, and v [-] is Poisson's ratio. Based on Eq. (6.5), the strains of ε_t and ε_c, which are used to calculate damage variable D are expressed by the following equations [6.31)]:

$$\bar{\varepsilon}_1 = \frac{1}{1+v}\left[\varepsilon_1 + \frac{v}{1-2v}\varepsilon_v\right], \tag{6.6}$$

$$\bar{\varepsilon}_3 = \frac{1}{1+v}\left[\varepsilon_3 + \frac{v}{1-2v}\varepsilon_v\right] = \varepsilon_t, \tag{6.7}$$

$$\varepsilon_c = \bar{\varepsilon}_1 - \frac{1+\sin\theta}{1-\sin\theta}\bar{\varepsilon}_3, \tag{6.8}$$

According to the failure criteria of Eq. (6.3) and the constitutive law shown in **Fig. 6.3**, damage variable D is calculated. [6.20) ,6.22),6.28),6.30),6.31)]

$$D = \begin{cases} 0 & F_1 < 0 \text{ and } F_2 < 0 \\ 1 - \left|\dfrac{\varepsilon_{t0}}{\varepsilon_t}\right|^{\eta} & F_1 = 0 \quad \text{and} \quad \Delta F_1 > 0 \\ 1 - \left|\dfrac{\varepsilon_{c0}}{\varepsilon_c}\right|^{\eta} & F_2 = 0 \quad \text{and} \quad \Delta F_2 > 0 \end{cases}, \tag{6.9}$$

where ε_{t0} [-] and ε_{c0} [-] are the limit tensile and compressive strain, respectively, and η [-] is the constant ($\eta = 2$). In Eq. (6.9), $F_1 = 0$ and $\Delta F_1 > 0$ represent the rock damage in the tensile mode when its stress state satisfies the maximum stress criterion and the rock is still under a loading condition. Similarly, $F_2 = 0$ and $\Delta F_2 > 0$ represent the damage in the shear mode when its stress state satisfies the Mohr-Coulomb criterion and the rock is still under a loading condition. Damage variable D is an important parameter for calculating the changes in the physical properties of the rock. In the proposed model, the recovery of the damage is not considered.

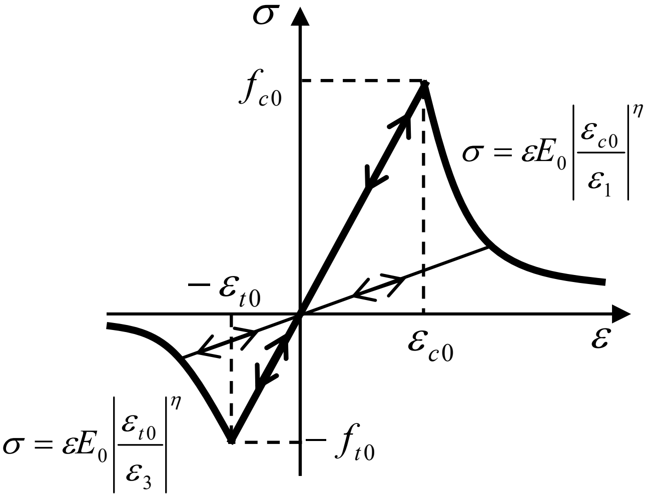

Fig. 6.3 Constitutive law of elastic damage theory under uniaxial tensile stress and uniaxial compressive stress[6.20),6.22),6.29)] .

(c) Heterogeneity of mechanical properties

In the proposed model, in order to describe the heterogeneity of the rock, the local mechanical properties within the rock mass are set by statistical dispersion. As the failure of ductile material generally conforms to the weakest-link theory[6.35)], extreme value distribution (i.e., distribution of a minimum value) should be used as the statistical dispersion. Therefore, in proposed model, the Weibull distribution that considers the extreme value distribution based on the weakest-link theory was applied. The mechanical properties of all the elements in the calculation domains are assumed to follow a given Weibull distribution that is defined by the following probability density function[6.20)~6.23),6.28)~6.33)]. Among the mechanical properties, although Poisson's ratio, whose heterogeneity is low, is set homogeneously, the elastic modulus, uniaxial tensile strength, and uniaxial compressive strength are defined by the following Weibull distribution:

$$\varphi(u) = \frac{m}{u^s}\left(\frac{u}{u^s}\right)^{m-1}\exp\left[-\left(\frac{u}{u^s}\right)^m\right], \tag{6.10}$$

where u is the mechanical parameter of each element in the calculation domain such as strength and the elastic modulus (i.e., $u = E_0, f_{t0}$, and f_{c0}), u^s is the scale parameter which defines the characteristic value of the distribution of mechanical parameter u (i.e., $u^s = E_0^s$, f_{t0}^s, and f_{c0}^s), and m [-] is the shape parameter which reflects the degree of material homogeneity and is denoted as a homogeneity index. The statistical density distribution curves for the uniaxial compressive strength of elements with a given characteristic value f_{c0}^s of 200 MPa at various homogeneity indices (m = 5.0, 4.0, 3.0, 2.0, and 1.5) is showed in **Fig. 6.4**. This figure indicates that an increase in the homogeneity index results in more homogeneous material. In **Fig. 6.4**, the distribution of uniaxial compressive strength is introduced as an example, but the distributions of all the other mechanical parameters (uniaxial tensile strength and elastic modulus) also have the same tendency. **Fig. 6.5** shows three numerical domains that are all composed of 200×100 elements and have a distribution of uniaxial compressive strength created randomly by the Weibull distribution with a given characteristic value f_{c0}^s of 200 MPa at different homogeneity indices (m = 5.0, 3.0, and 1.5). This figure expresses that different strength values are assigned to each element and that the number of elements whose strength is similar to characteristic value f_{c0}^s increases with the increase in homogeneity index m. Although the statistical approach using Eq. (6.10) is simple, such a heterogeneous distribution of mechanical properties based on the Weibull distribution may replicate real rock that contains heterogeneity induced by the inherent distribution of minerals and micro-cracks.

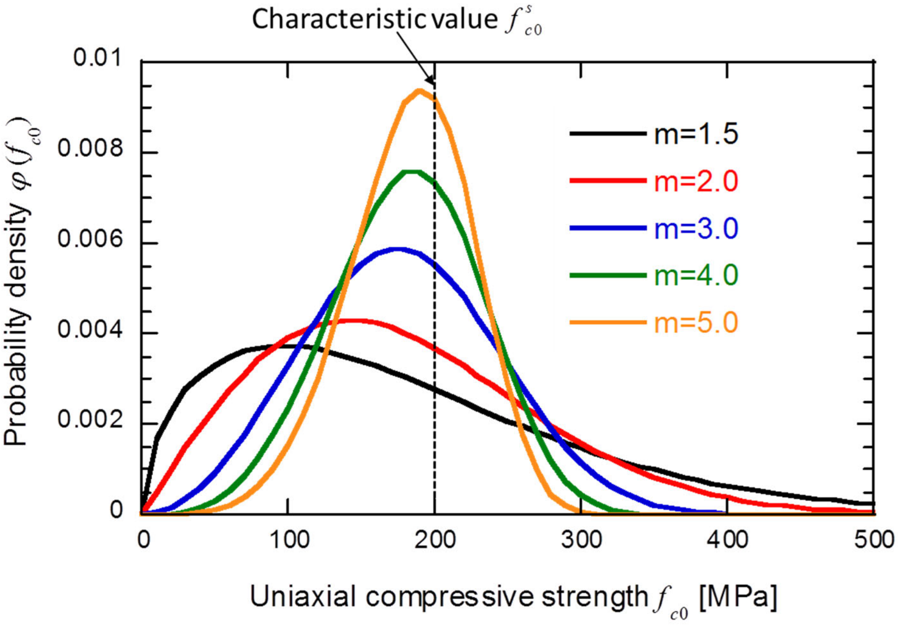

Fig. 6.4 Statistical distribution of probability density function for uniaxial compressive strength with different homogeneity indices (m = 5.0, 4.0, 3.0, 2.0, and 1.5) and characteristic value of $f_{c0}{}^{s}$ = 200 MPa.

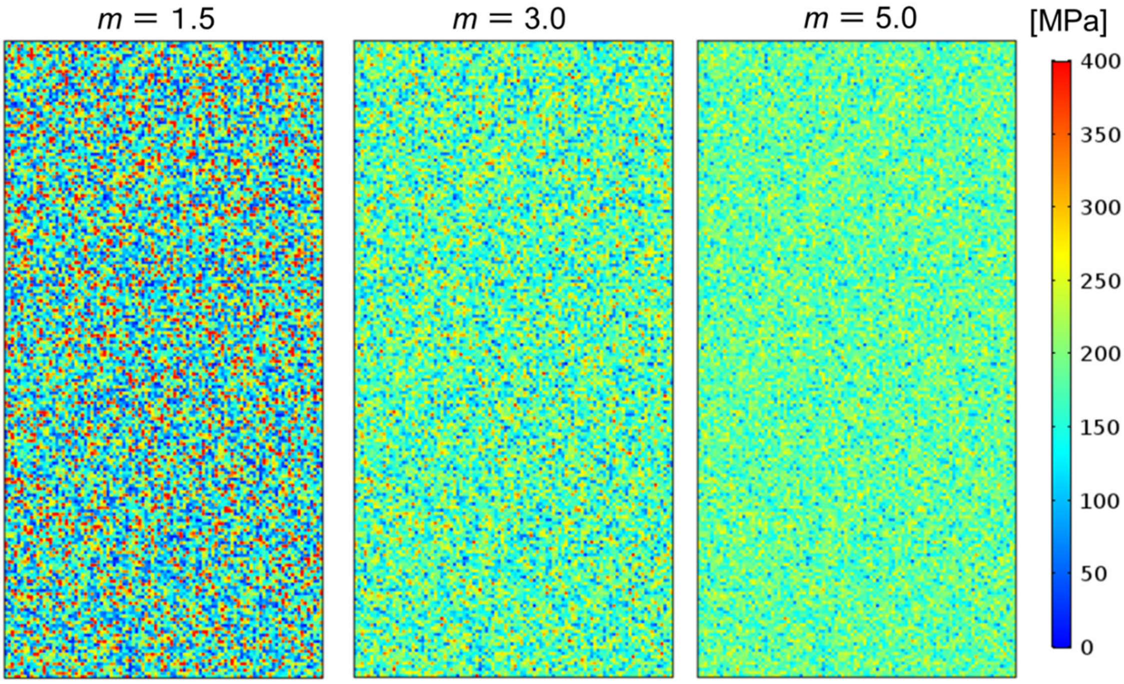

Fig. 6.5 Distribution of uniaxial compressive strength within numerical domains with different homogeneity indices (m = 5.0, 3.0, and 1.5) and characteristic value that $f_{c0}{}^{s}$ = 200 MPa.

(d) Fluid flow

The groundwater flow in the rock is calculated by the conservation of water mass based on the poroelastic theory and by assuming the Darcian flow, as

$$\rho_w S \frac{\partial p}{\partial t} + \nabla \cdot (\rho_w \boldsymbol{u}) + \rho_w \alpha_B \frac{\partial \varepsilon_v}{\partial t} = f_m , \tag{6.11}$$

$$\boldsymbol{u} = -\frac{\boldsymbol{k}}{\mu} (\nabla p + \rho_w g \nabla h) , \tag{6.12}$$

where ρ_w [kg m^{-3}] is the density of the fluid, S [Pa^{-1}] is the storage coefficient, $\boldsymbol{u}$ [m s^{-1}] is the fluid velocity tensor, f_m [kg m^{-3} s^{-1}] is the source term for the flow, $\boldsymbol{k}$ [m^2] is the rock permeability tensor, μ [Pa s] is the fluid dynamic viscosity, g [m s^{-2}] is the gravity acceleration, and h [m] is the potential head. The permeability within the undamaged and the damaged zones is expressed as

$$k = \begin{cases} k_0 & D = 0 \\ \dfrac{b^2}{12} & D > 0 \end{cases} , \tag{6.13}$$

where k_0 [m^2] is the permeability of the undamaged rock and b [m] is the average mechanical fracture aperture. In the proposed model, it is assumed that mechanical fracture aperture is equivalent to hydraulic fracture aperture. The changes in rock permeability and fracture aperture due to the evolution of damage is represented as$^{6.36)}$

$$k_D = k_0 \exp(\alpha_k D) , \tag{6.14}$$

$$b_D = \sqrt{12 k_D} = \sqrt{12 k_0 \exp(\alpha_k D)} , \tag{6.15}$$

where k_D [m^2] is the permeability of the damaged rock, α_k [-] is the coefficient that represents the damage-permeability effect, and b_D [m] is the fracture aperture of the damaged rock.

(e) Heat transfer

In the thermal process, the temperature of the rock is calculated by the following heat transfer equation:

$$(\rho C_p)_{eq}\frac{\partial T}{\partial t} + \rho_w C_{p,w}\boldsymbol{u}\cdot\nabla T = \nabla\cdot(\boldsymbol{\lambda}_{eq}\nabla T) + Q_h\,, \tag{6.16}$$

$$(\rho C_p)_{eq} = (1-\phi)\,\rho_m C_{p,m} + \phi\,\rho_w C_{p,w}\,, \tag{6.17}$$

$$\boldsymbol{\lambda}_{eq} = (1-\phi)\,\boldsymbol{\lambda}_m + \phi\,\boldsymbol{\lambda}_w\,, \tag{6.18}$$

where T [K] is the system temperature, $(\rho C_p)_{eq}$ [J K^{-1} m^{-3}] is the equilibrium volumetric heat capacity, $C_{p,w}$ [J kg^{-1} K^{-1}] is the heat capacity of the fluid, $\boldsymbol{\lambda}_{eq}$ [W m^{-1} K^{-1}] is the equilibrium thermal conductivity tensor, Q_h [W m^{-3}] is the heat source, ρ_m [kg m^{-3}] is the density of the solid, $C_{p,m}$ [J kg^{-1} K^{-1}] is the heat capacity of the solid, $\boldsymbol{\lambda}_m$ and $\boldsymbol{\lambda}_w$ [W m^{-1} K^{-1}] are the thermal conductivity tensors of the solid and the fluid, respectively. The change in thermal conductivity due to the evolution of damage is expressed as$^{21)}$

$$\lambda_m = \lambda_{m0}\exp(\alpha_\lambda D) \tag{6.19}$$

where λ_{m0} [W m^{-1} K^{-1}] is the thermal conductivity of the undamaged rock and α_λ [-] is the coefficient representing the effect of the damage on the thermal conductivity.

(f) Reactive transport

The solute transport behavior in the pore water is calculated by the basic advection-diffusion equation. In the proposed model, the mechanical dispersion and the retardation due to the sorption processes are not considered.

$$\frac{\partial(c_i\phi)}{\partial t} + \boldsymbol{u}\cdot\nabla c_i = \nabla\cdot(\boldsymbol{D}_{e,i}\nabla c_i) + r_i\,, \tag{6.20}$$

$$\boldsymbol{D}_{e,i} = \phi\tau\,\boldsymbol{D}_{b,i}\,, \tag{6.21}$$

$$r_i = \sum_j^n v_{i,j} R_j , \tag{6.22}$$

where c_i [mol m^{-3}] is the concentration of solute i in the pore water, $\boldsymbol{D}_{e,i}$ [m^2 s^{-1}] is the effective diffusion coefficient tensor, $\boldsymbol{D}_{b,i}$ [m^2 s^{-1}] is the diffusion coefficient tensor, τ [-] is the coefficient related to tortuosity, r_i [mol m^{-3} s^{-1}] is the source term of solute i, where $v_{i,j}$ [-] is the stoichiometry coefficient of solute i in reaction of mineral j, n is the number of minerals composing the targeted rock, and R_j [mol m^{-3} s^{-1}] is the rate of the mineral reactions for mineral j. The diffusion coefficient is temperature-dependent and can be defined by an Arrhenius-type equation$^{6.37)}$.

$$D_{b,i} = D_{b,i}^0 \exp(-E_{D,i} / RT) , \tag{6.23}$$

where $D_{b,i}^0$ [m^2 s^{-1}] and $E_{D,i}$ [J mol $^{-1}$] are the pre-exponential factor and the activation energy of the diffusion of solute i, respectively, and R [J mol $^{-1}$K^{-1}] is the gas constant.

(g) Pressure dissolution within fractures

In the current work, the mineral reactions include the mineral dissolution/precipitation on the free-surface within the rock fractures and the mineral dissolution at the contacting asperities within the rock fractures (pressure dissolution). Thus, the rate of the mineral reactions for mineral j, R_j, is expressed by

$$R_j = R_{f,j}^{FF} + R_{f,j}^{PS} , \tag{6.24}$$

where $R_{f,j}^{FF}$ [mol m^{-3} s^{-1}] is the rate of the free-face dissolution/precipitation of mineral j within the rock fracture, and $R_{f,j}^{PS}$ [mol m^{-3} s^{-1}] is the rate of the pressure dissolution of mineral j at the contacting asperities within the rock fracture.

In this chapter, the target rock in coupled THMC analysis is assumed to be composed purely of quartz, and subscript j in Eqs. (6.22) and (6.24) is omitted hereinafter. Within rock fractures, pressure dissolution may occur at the contacting asperities (fracture contacts), as shown in **Fig. 6.6**. When pressure dissolution occurs continuously at the fracture contacts, fracture aperture *b* decreases and the fracture contact area increases with time. As shown in **Fig. 6.7**, when the geometric model obtained by idealizing the arbitrary micro-domain, composed of contacting asperities and pore space, is set as the representative element of the rock fractures[6.11),6.38)], the rate of pressure dissolution at the contacting asperities within the rock fracture is defined by Ogata et.al[6.38)] (introduced in **Chapter 4**) and given as follows:

$$R_f^{PS} = \frac{3 f_r R_{f,c} V_m k_+}{RTb(1-R_{f,c})}\left(\frac{\sigma'_m}{R_{f,c}} - \sigma_c\right), \tag{6.25}$$

$$R_{f,c} = \frac{A_t^c}{A_t^l}, \tag{6.26}$$

where k_+ [mol m^{-2} s^{-1}] is the mineral dissolution rate constant, $R_{f,c}$ [-] is the contact-area ratio within the fracture, V_m [m^3 mol^{-1}] is the molar volume, f_r [-] is the roughness factor, which is the ratio of the true (microscopic) surface area over the apparent (geometric) surface area, σ'_m [Pa] is the mean effective stress, σ_c [pa] is the critical stress, A_t^l [m^2] is the total fracture cross-sectional area in the representative element, and A_c^l [m^2] is the contact area within the fracture of the representative element, $A_c^l = R_{f,c} A_t^l$. The mineral dissolution rate constants are defined by the Arrhenius expression, given as

$$k_+ = k_+^0 \exp(-E_{k_+}/RT), \tag{6.27}$$

where k_+^0 [mol m^{-2} s^{-1}] is the pre-exponential factor and E_{k_+} [J mol $^{-1}$] is the activation energy of the mineral dissolution.

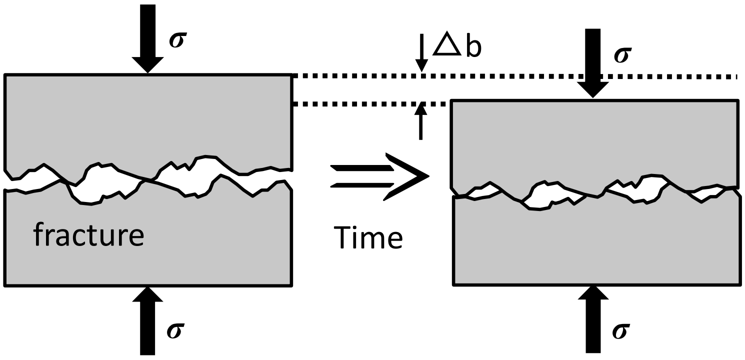

Fig. 6.6 Schematic of pressure dissolution at contacting asperities within the fracture$^{6.11)}$.

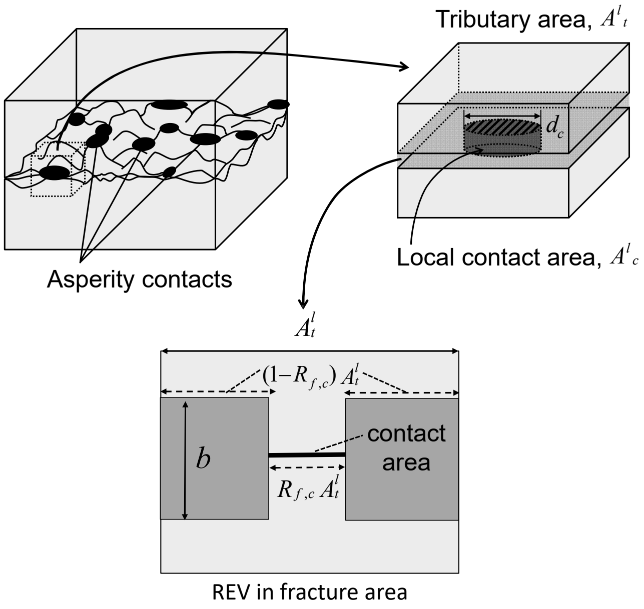

Fig. 6.7 Geometrical model that includes representative element in rock fracture area$^{6.11),6.38)}$.

The occurrence of pressure dissolution induced by the generated fractures is formulated based on Eq. (6.25). In the proposed model, fracture is generated when $D>0$. Therefore, the free-face dissolution and pressure dissolution within fractures occur only in the damaged zone where $D>0$. In addition, Eq. (6.25) can be extended by considering the failure mode of fractures. As shown in **Fig. 6.6**, the driving force of pressure dissolution σ is a stress component that acts on the direction for fracture compaction. In the damage theory used here, the components of the principle stresses that work as the driving force of failure exist for the individual failure modes of tensile and shear (**Fig. 6.8**). The components of principle stresses can be assumed as the driving force of the pressure dissolution at the contacting asperities within the fracture after any damage has been generated. Thus, as shown in **Fig. 6.8**, pressure dissolution does not occur within the fracture when $\sigma_3 < 0$, but it should occur when the stress state moves to a compressive state (i.e., $\sigma_3 > 0$).

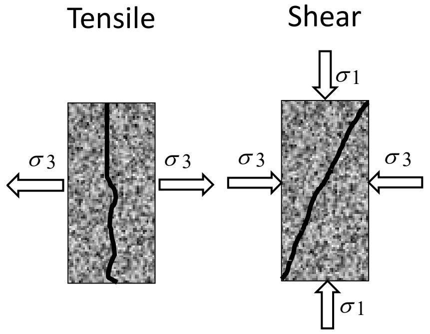

Fig. 6.8 Driving forces for generating fractures in two failure modes.

Consequently, the rate of pressure dissolution is expressed by considering damage variable *D* and the failure modes of the fracture, F_1 and F_2 (Eq. (6.3)), given as follows:

$$\begin{cases} R_f^{PS} = 0 & D = 0 \\ R_f^{PS} = \dfrac{3 R_{f,c} f_r V_m k_+}{RTb(1 - R_{f,c})} \left(\dfrac{\langle \sigma_3 \rangle}{R_{f,c}} - \sigma_c \right) & D > 0, F_1 = 0 \\ R_f^{PS} = \dfrac{3 R_{f,c} f_r V_m k_+}{RTb(1 - R_{f,c})} \left(\dfrac{\langle \sigma_1 \rangle + \langle \sigma_3 \rangle}{R_{f,c}} - \sigma_c \right) & D > 0, F_2 = 0 \end{cases}, \tag{6.28}$$

where <> represents the following function:

$$\langle x \rangle = \begin{cases} x & x \geq 0 \\ 0 & x < 0 \end{cases}. \tag{6.29}$$

The developed model assumes that the directions of principle stress do not change with time after the termination of the fracture initiation/propagation. Thus, the influence of the change in the directions of principle stress after the fracture initiation/propagation on the pressure dissolution is not considered.

(h) Free-face dissolution/precipitation within fractures

The rate of the free-face dissolution within the rock fracture has been defined by Ogata et al.[6.38] (introduced in **Chapter 4**), as follows:

$$R_f^{FF} = 2 f_r k_+ (1 - Q / K_{eq}) / b \,, \tag{6.30}$$

where Q [-] is the ionic activity product and K_{eq} [-] is the equilibrium constant. When Q / K_{eq} <1, free-face dissolution occurs, and when Q / K_{eq}>1, free-face precipitation occurs. As fracture is generated when D>0 in the proposed model, the rate of the free-face dissolution/precipitation is defined as

$$\begin{cases} R_f^{FF} = 0 & D = 0 \\ R_f^{FF} = 2 f_r k_+ (1 - Q / K_{eq}) / b & D > 0 \end{cases} . \tag{6.31}$$

(i) Fracture aperture change

In the proposed model, only the change in the fracture aperture is considered in the calculation; the change in the porosity within the rock matrix is not considered. The change in the fracture aperture is induced by the fracture initiation/propagation and mineral dissolution/precipitation. Thus, the fracture aperture at arbitrary time t is defined by considering the aperture generated by the fracture initiation/propagation and temporal alternation of the aperture due to the free-face dissolution/precipitation and pressure dissolution, as

$$b(t) = b_D + b^{FF}(t) + b^{PS}(t)\,, \tag{6.32}$$

$$b^{FF}(t) = \int 2 f_r k_+ (1 - R_{f,c}) V_m (1 - Q / K_{eq}) dt\,, \tag{6.33}$$

$$\begin{cases} b^{PS}(t) = \int \dfrac{-3 f_r V_m^2 k_+}{RT} \left(\dfrac{\langle \sigma_3 \rangle}{R_{f,c}} - \sigma_c \right) dt & D > 0, F_1 = 0 \\ b^{PS}(t) = \int \dfrac{-3 f_r V_m^2 k_+}{RT} \left(\dfrac{\langle \sigma_1 \rangle + \langle \sigma_3 \rangle}{R_{f,c}} - \sigma_c \right) dt & D > 0, F_2 = 0 \end{cases}\,, \tag{6.34}$$

where $b^{FF}(t)$ [m s^{-1}] is the change in fracture aperture by the free-face dissolution/precipitation at arbitrary time t and $b^{PS}(t)$ [m s^{-1}] is the change in fracture aperture by the pressure dissolution at arbitrary time t. Mineral reactions alter the fracture aperture, and the contact-area ratio within the fractures changes due to the change in the fracture aperture. The relation between the fracture aperture and the contact-area ratio within the fractures may be given by the following simple equation[6.12)]:

$$b(t) = b_r + (b_D - b_r)\exp(-(R_{f,c}(t) - R_{f,cD}) / a)\,, \tag{6.35}$$

where b_r [m] is the residual fracture aperture, $R_{f,c}(t)$ [-] is the contact-area ratio within the fracture at arbitrary time t, $R_{f,cD}$ [-] is the contact-area ratio within the fracture when fracture is generated, and a [-] is a constant.

(j) Relation between fracture initiation/propagation and contact area ratio with change in fracture aperture

The contact-area ratio within the fracture when fracture is generated, in Eq. (6.35), is explained in detail. Based on the continuum damage theory, damage variable D is defined as the ratio of the arbitrary cross-sectional area of the representative element over the pore space of the representative element[6.39)]. In the proposed model, the arbitrary domain composed of contacting asperities and pore space, is assumed as the representative element of the rock fractures. Therefore, the contact- area ratio within the fracture when fracture is generated, $R_{f,cD}$, is represented using damage variable D of the representative element of the rock fractures, given as

$$D = \frac{A_t^l (1 - R_{f,cD})}{A_t^l}, \tag{6.36}$$

$$R_{f,cD} = 1 - D. \tag{6.37}$$

In the current work, after the fracture initiation/propagation, changes in damage variable D are not considered.

6.3 Numerical simulation

In this section, two numerical simulations are shown. Firstly, calculations of the fracture initiation/propagation by the damage theory incorporated in the developed model are explained. Subsequently, long-term predictions of the permeability in the rock near the radioactive waste within a geological disposal system of high-level radioactive waste are conducted using the coupled THMC model proposed in this chapter.

6.3.1 Verification of fracture initiation/propagation

In order to predict the changes in the physical properties of rock masses due to fracture generation, it is necessary to reproduce the behavior of the fracture initiation/propagation within the rock observed in mechanical experiments. Then, uniaxial compression experiments are conducted with the granite specimen and the validity of the numerical analysis is confirmed by calculating the fracture initiation/propagation utilizing the damage theory for the experiment. The granite specimen (50 mm in diameter ×100 mm in length) is used in the experiment which is the target for calculations. In the numerical analyses, as shown in **Fig. 6.9**, the calculation domain was set to be a 2D rectangle with a width of 50 mm and a length of 100 mm, simulating the real specimen used in the experiments, and a vertical displacement v of 0.01 mm/step was applied on the top boundary of the calculation domain. The numerical calculation was conducted with the finite element method. In the damage theory incorporated into proposed model, because failure is evaluated in each calculation element, the damage size is dependent on the element size (i.e., the application of a larger-size element results in a larger damaged area). It was reported that when a smaller-size element is applied, the accuracy of the simulating fracture is higher[6.22),6.30)]. Therefore, a sufficiently small mesh size (the total number of element is 20000 with the mesh size of 0.5 mm) was applied in the current calculations. The parameters used in the calculations are summarized in **Table 6.1**.

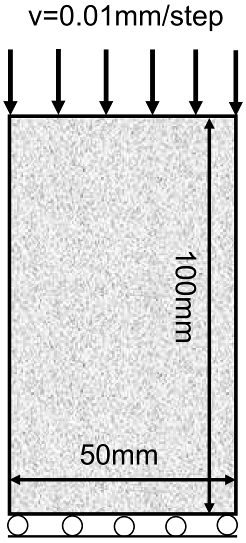

Fig. 6.9 Calculation domain and boundary conditions for simulation of uniaxial compression test using granite.

Table 6.1 Parameters used in simulation of uniaxial compression test.

Parameter	Value
Homogeneity index of material properties [-] m	3.5
Characteristic value of elastic modulus [GPa] $E_0{}^s$	70.0
Characteristic value of uniaxial tensile strength [MPa] $f_{t0}{}^s$	42.4
Characteristic value of uniaxial compressive strength [MPa] $f_{c0}{}^s$	811.8
Internal friction angle [°] θ	62.0
Poisson's ratio [-] v	0.25

Among the mechanical properties within the calculation domain, the uniaxial tensile strength, uniaxial compressive strength, and elastic modulus are set heterogeneously, while Poisson's ratio and the internal friction angle are set homogeneously. The elastic modulus of 58.7 MPa, uniaxial compressive strength of 147.6 MPa, and Poisson's ratio of 0.25 were obtained from the uniaxial compression experiments. The tensile strength obtained from the Brazilian experiments, using the rock specimen taken from same site, was 7.7 MPa. Previous researches[6.21),6.30),6.31)] confirmed that it is necessary to set the characteristic value of each strength (uniaxial tensile strength and uniaxial compressive strength), u^{s} (see Eq. (6.10)), to be higher than the experimental values in order to reproduce the measured uniaxial compressive strength accurately when the calculation of the fracture evolution is conducted by incorporating the heterogeneity of the mechanical properties of the rock masses. In addition, based on the previous studies[6.30),6.32)], homogeneity index m (see Eq. (6.10)) was suggested to be in the range of 1.2 ~ 5.0 for accurately simulating the fracture process within the rock. With reference to these literary references, the characteristic values of the mechanical properties and homogeneity index m were set so that the predicted results would be equivalent to the experimental data. The internal friction angle was set to be the value evaluated by the uniaxial compressive strength and the tensile strength. A comparison of the predicted and experimental results for the relation between the vertical stress and strain is shown in **Fig. 6.10**. As it is difficult to measure the data after the failure in uniaxial compression experiments, when using hard, brittle rocks such as granite, the comparison was conducted in the current work only for measured data until the failure point. During the experiment, micro cracks were generated within the specimen before the failure. As is apparent from the figure, the prediction shows a good agreement with experimental data.

The evolution of damage variable D ($0 \leq D \leq 1$) is shown in **Fig. 6.11(a)**. The distributions of the damage variable depicted in **Fig. 6.11(a)** represent the behavior of the fracture initiation/propagation from Point A (corresponding to Point A in **Fig. 6.10**) to Point B (corresponding to Point B in **Fig. 6.10**). A comparison between the predicted fracture distribution and the fracture distribution observed from the experiment in **Fig. 6.11(b)** shows that the predictions reproduce the experimental results relatively well. From these results, the calculation of the fracture initiation/propagation using the damage theory incorporated into the proposed model was validated for predicting the process of the evolution of rock fractures in the actual field.

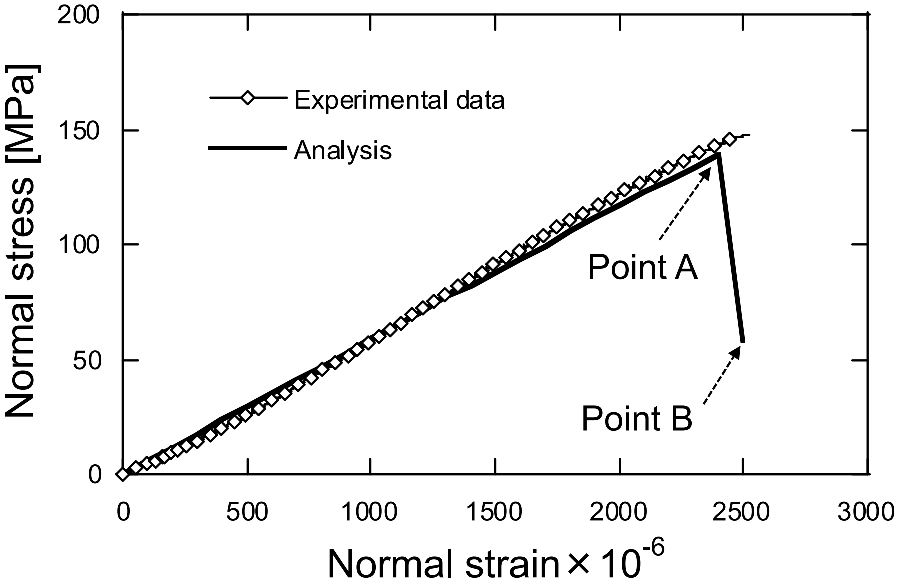

Fig. 6.10 Comparison of relationship between vertical stress and strain between experimental result and prediction.

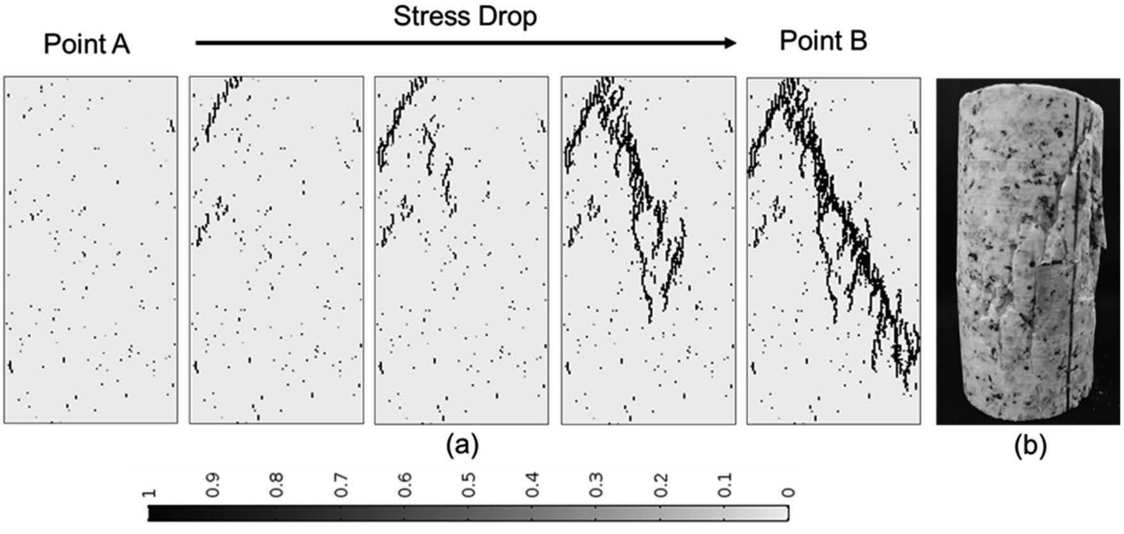

Fig. 6.11 (a) Evolution of damage variable *D* obtained from simulation of uniaxial compression test using granite (Point A and Point B correspond to Point A and Point B shown in **Fig. 6.10**, respectively) and (b) fracture distribution obtained from the experiment.

6.3.2 Numerical analysis related to high-level radioactive geological disposal

The proposed model was also applied to predict the long-term evolution of the permeability in the rock near the radioactive waste within a geological disposal system of high-level radioactive waste. In the analysis, the horizontal storage of radioactive waste, as shown in the scientific and technical report summarizing the HLW disposal construction in Japan 6.40), was assumed. As shown in **Fig. 6.12**, bedrock from the depth 400 m to 500 m from the ground surface, with a disposal cavity at a depth of 450 m, was set as the calculation domain6.15). The canisters of radioactive waste were virtually installed in the cavity as a heat source. The 2D domain for the calculations was set by assuming that the diameter of the cavity, and the horizontal length in right and left directions around the cavity, would be 2.0 and 6.1 m, respectively. In this analysis, at first, a simulation of the cavity excavation was conducted. Secondly, by setting the initial stress condition obtained from the excavation analysis as the initial condition, the long-term prediction of the changes in permeability was conducted. The target for the calculation was assumed to be porous rock with a density 1800 kg/m^3, which does not include any fractures and is composed purely of quartz. The initial porosity, which is a parameter controlling the thermal conductivity (see Eq. (6.18)) and diffusivity of the chemical solute in the pore water (see Eq. (6.21)), was set to be 40%. With regard to the mechanical properties, the elastic modulus and each strength (uniaxial tensile strength and uniaxial compressive strength) were distributed within the domain by the Weibull distribution and the other properties were set homogeneously. The hydraulic and thermal gradients were set to be 1/1000 and 5°C/100m, respectively. The surface temperature was fixed at 15°C.

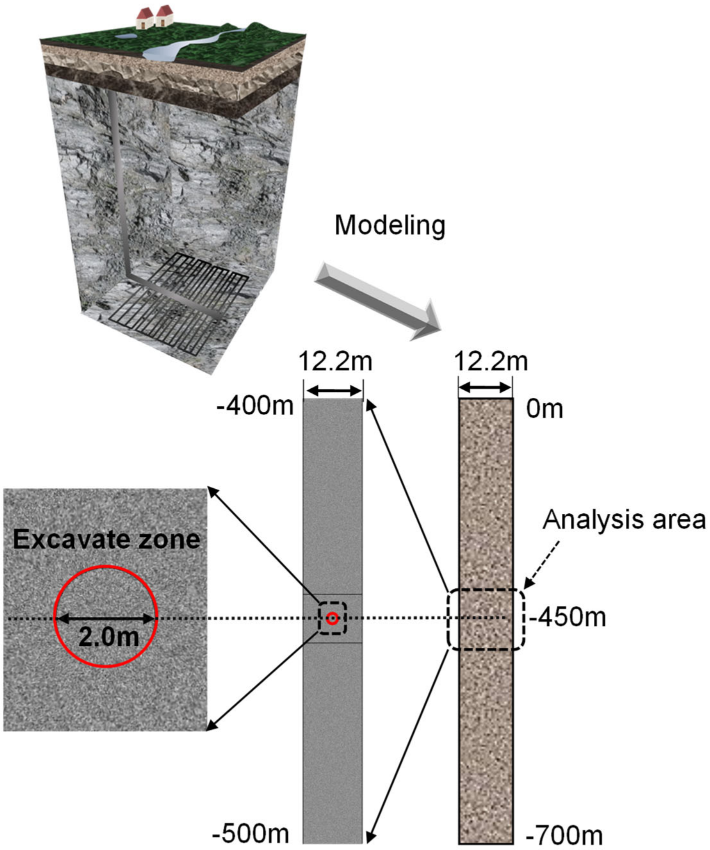

Fig. 6.12 Calculation domain of simulation for predicting changes in rock permeability.

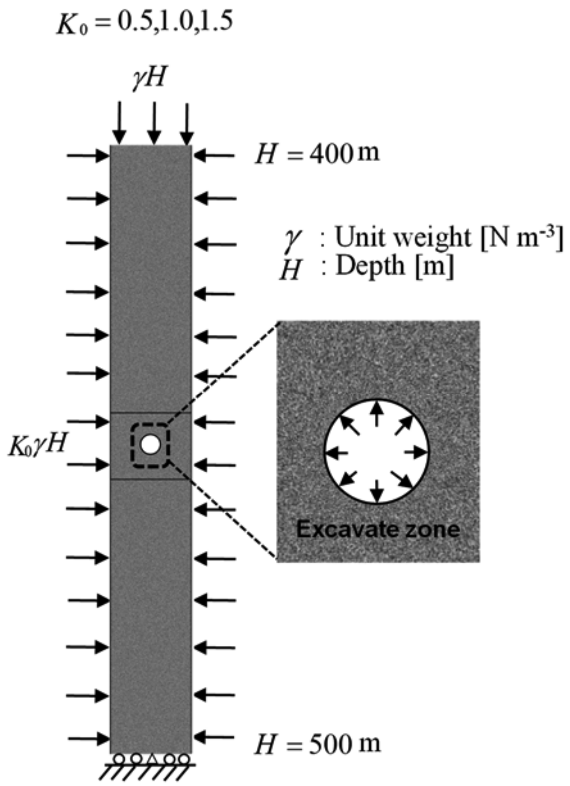

Fig. 6.13 Description of excavation analysis.

(a) Analysis of cavity excavation

In the analysis of the cavity excavation, as shown in **Fig. 6.12**, the mechanical behavior of the rock was evaluated, including the fracture evolution during the excavation of the disposal cavity with a diameter of 2.0 m and a depth of 450 m. The characteristic values for the distributions of the mechanical properties that conform the Weibull distribution (uniaxial tensile strength, uniaxial compressive strength, and elastic modulus) were set to be 2.2 MPa, 22.0 MPa, and 3.0 GPa, respectively. Homogeneity index *m* was set to be 4.0. Poisson's ratio and the internal friction angle were set to be 0.3 and 30°, respectively. In the excavation analysis, firstly, the internal outward radial pressure applied to the cavity boundary to replace the in situ stress condition is evaluated, and then it decreases monotonically by 1% per step for 100 steps (**Fig. 6.13**). The calculation domain is discretized into 62636 triangle elements, and in the area where the fracture initiation/propagation is expected (i.e., the calculation domain from the depth of 445 to 455 m from the ground surface), a smaller mesh size than the other areas is applied. The representative mesh size of the elements located extremely close to the cavity and those in the other areas are set to be 0.08 and 0.5 m, respectively. In the current work, calculations of the cavity excavation are conducted using three different values of lateral pressure coefficients K_0 ($K_0 = 0.5$, 1.0, and 1.5) to investigate the influence of the in-situ stress state. The evolution of the fracture initiation/propagation (change in distribution of damage variable D) around the cavity during the excavation is shown in **Figs. 6.14 (a)-(c)**. In these figures, in order to distinctly display the two kinds of damage modes (i.e., tensile damage and shear damage), the sign of the damage variable D values in the shear damage is changed to negative (i.e., $0 \leq D \leq 1 \Rightarrow -1 \leq D \leq 0$). Therefore, the shear damage (red-color area) is represented with negative numbers ($-1 \leq D < 0$), while the tensile damage (blue-colored area) is represented with positive ones ($0 < D \leq 1$). As is apparent from the figures, in all three cases, the shear damage is more remarkable than the tensile one, while the distribution of damage is different due to the K_0 values. The tensile damage occurs near the shear one. This is likely to be because the compressive deformation is enhanced by the decrease in the elastic modulus due to evolution of shear damage, and tensile stress occurs within the surrounding rock (rock near the shear damage zone), which may result in the pulling of the neighboring shear damage zone.

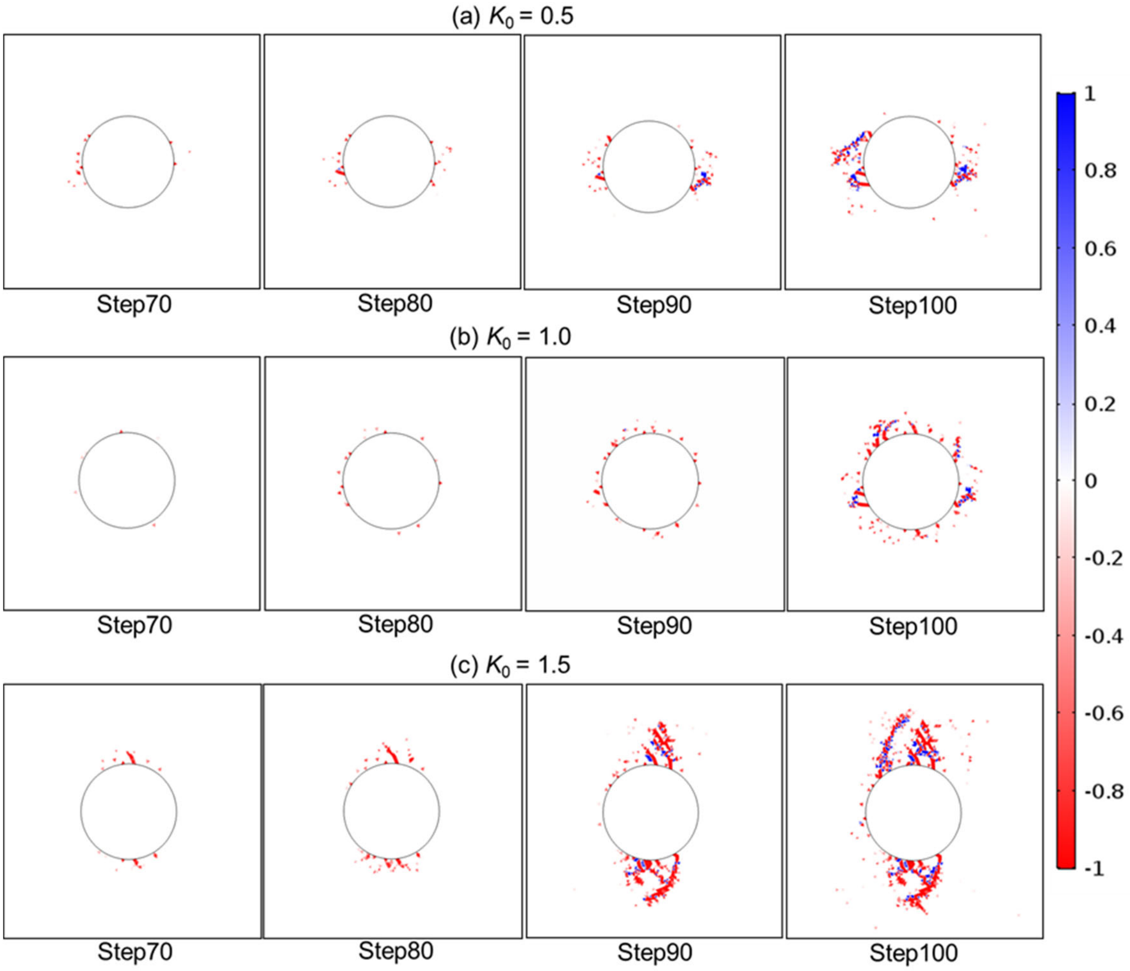

Fig. 6.14 Evolution of damage variable D with different values for lateral pressure coefficient K_0: (a) $K_0 = 0.5$, (b) $K_0 = 1.0$, and (c) $K_0 = 1.5$.

A comparison among the three cases shows that a number of fractures were generated horizontally around the walls of the cavity in the case of $K_0 = 0.5$. In the case of $K_0 = 1.0$, it is confirmed that many fractures were generated around the periphery of the cavity. Generally, when the mechanical properties of rock masses are set to be homogeneous, shear damage rarely occurs under the condition of $K_0 = 1.0$. However, this analysis considers the heterogeneity of the mechanical properties (elastic modulus and strength) and shear damage occurs due to the influence of the heterogeneity of the elastic modulus. In the case of $K_0 = 1.5$, fractures grow vertically around the crown and the invert. When this case is compared with the other cases ($K_0 = 0.5$ and $K_0 = 1.0$), the generated fracture zone is the most extensive. This is because the high compressive stress is concentrated around the crown and the invert of the cavity due to the excavation.

(b) Long-term coupled THMC analysis

By setting the physical properties of the rock (elastic modulus, thermal conductivity, fracture aperture, and contact-area ratio) obtained from the excavation analysis as the initial conditions, the coupled THMC numerical analysis was conducted. The analysis period was set to be 10^2 years after disposing the waste package in the excavated cavity. The heat source from the radioactive waste was considered by setting the time-dependent temperature change outside the buffer material obtained from the literature[6.40)] (**Fig. 6.15**) at the periphery of the cavity as boundary conditions. In the calculation of the heat transfer, the following Neumann boundary condition is set at all the boundaries excluding the periphery of the cavity:

$$\frac{\partial T}{\partial \boldsymbol{n}} = 0 , \tag{6.38}$$

where ***n*** represents the outward normal direction to the targeted boundary. In the calculation of the reactive transport, the following Neumann boundary condition is set at all the boundaries of the calculation domain.

$$\frac{\partial c_i}{\partial \boldsymbol{n}} = 0 . \tag{6.39}$$

In the current work, the fracture initiation/propagation is considered only in the process of the cavity excavation and the new generation of fractures after the excavation is not considered. The parameters utilized in the calculation are summarized in **Table 6.2**.

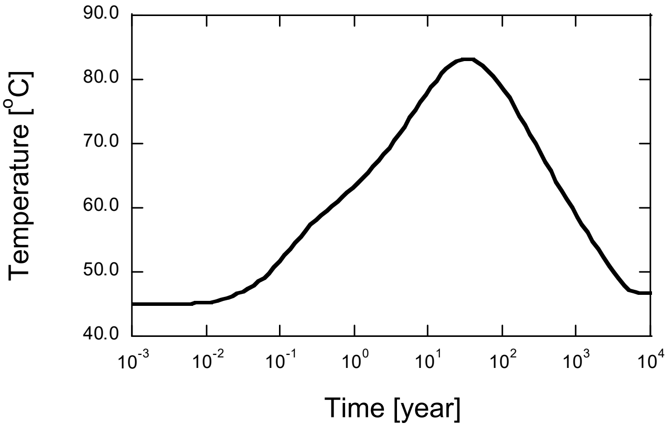

Fig. 6.15 Temperature change with time used as boundary condition applied on periphery of cavity[6.40)].

Table 6.2 Parameters used in simulation for predicting changes in rock permeability.

Parameter	Value
Homogeneity index of material properties [-] m	4.0
Characteristic value of elastic modulus [GPa] $E_0{}^s$	3.0
Characteristic value of uniaxial tensile strength [MPa] $f_{t0}{}^s$	2.2
Characteristic value of uniaxial compressive strength [MPa] $f_{c0}{}^s$	22.0
Internal friction angle [°] θ	30.0
Poisson's ratio [-] ν	0.3
Initial permeability [m^2] k_0	1.0×10^{-15}
Porosity [-] ϕ	0.4
Initial thermal conductivity of solid [w m^{-1} K^{-1}] λ_{m0}	1.6
Heat capacity of solid [kJ kg^{-1} K^{-1}] $C_{p,m}$	1.9
Roughness factor [-] f_r	10.0
Critical stress [MPa] σ_c	15.0

In the current work, a comparison of the calculation results between two different cases was conducted. One case was done by considering the THMC processes with pressure dissolution, called the "PS condition" (including both pressure dissolution and free-face dissolution in the mineral reactions). The other case was done by excluding the process of pressure dissolution, called the "no-PS condition" (including only free-face dissolution in the mineral reactions). The changes in permeability with time around the cavity under the no-PS and PS conditions under three initial ground pressure conditions (K_0 = 0.5, 1.0, and 1.5) are compared in **Figs. 6.16** and 6.**17**. In the figures, permeability is shown by log notation (i.e., $\log_{10}k$). The initial distribution of permeability depicted in the figures shows that the permeability in the damaged zone generated by the cavity excavation increases to about two orders of magnitude greater than the intact rock zone at the maximum. As is apparent from the figures, the permeability does not change with time under the no-PS condition, while the permeability in the damaged zone decreases with time under all the initial ground pressure conditions under the PS condition. The permeability in almost all the damaged zone decreases to the that of the intact rock zone. This is because of the occurrence of the pressure dissolution at the contacting asperities within the rock fractures in the damaged zone.

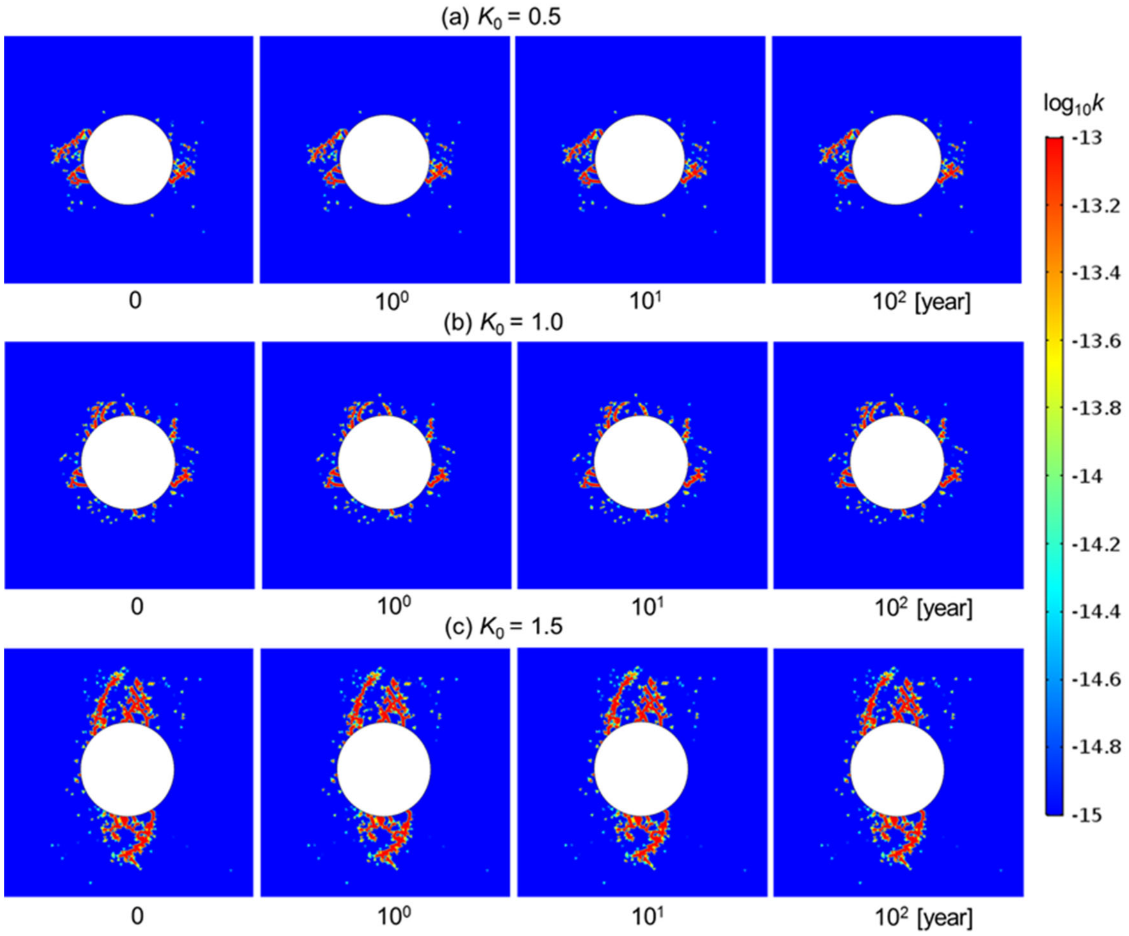

Fig. 6.16 Evolution of permeability with different values for lateral pressure coefficient under no-PS condition: (a) $K_0 = 0.5$, (b) $K_0 = 1.0$, and (c) $K_0 = 1.5$.

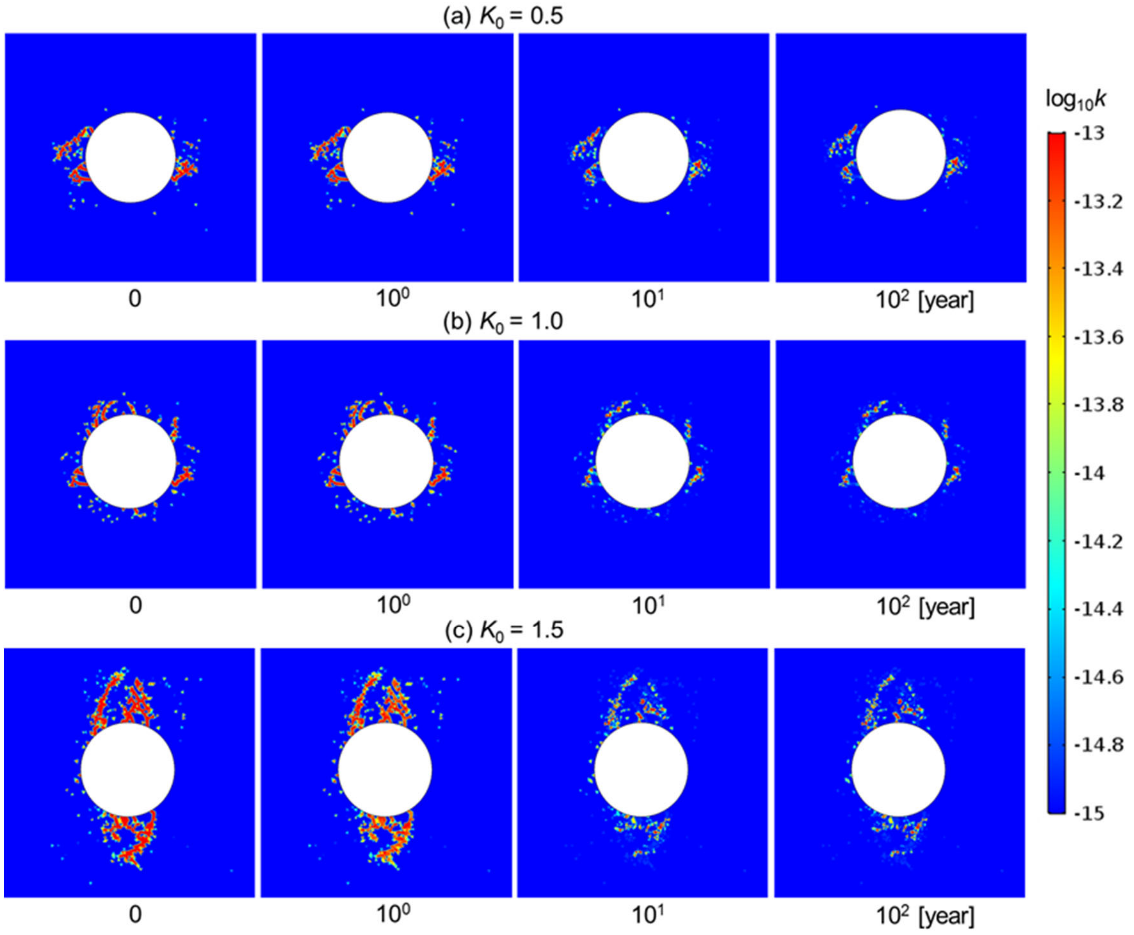

Fig. 6.17 Evolution of permeability with different values for lateral pressure coefficient under PS condition: (a) K_0 = 0.5, (b) K_0 = 1.0, and (c) K_0 = 1.5.

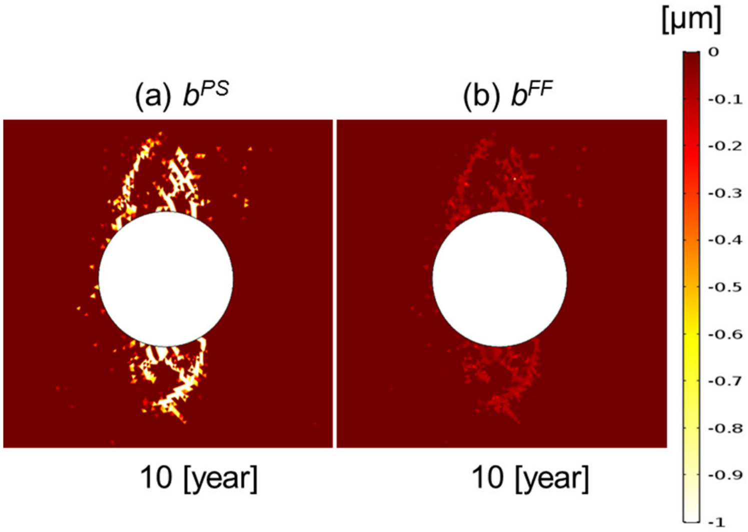

Fig. 6.18 Quantity of fracture aperture change due to pressure dissolution and free-face dissolution/precipitation: (a) b^{PS} (quantity of fracture aperture change due to pressure dissolution used in Eq. (6.34)) and (b) b^{FF} (quantity of fracture aperture change due to free-face dissolution/precipitation used in Eq. (6.33)).

Subsequently, the influence of the pressure dissolution on the permeability reduction is further investigated. In this analysis, the fracture aperture change with time resulting from the pressure dissolution and the free-face dissolution/precipitation should be able to alter the rock permeability with time. The quantity of fracture aperture change due to the pressure dissolution and free-face dissolution/precipitation in 10 years after disposing the radioactive material under the PS condition in the case of $K_0 = 1.5$ is depicted in **Fig. 6.18**. The figure shows that the quantity of the fracture aperture change due to the free-face dissolution/precipitation is also a negative number as well as that due to the pressure dissolution, and it is apparent that the reduction in the fracture aperture is caused not only by the pressure dissolution, but also by the free-face dissolution/precipitation. By Eq. (6.33), when the mineral precipitation is more remarkable than the mineral dissolution at the free-surface of the rock fractures, the quantity of fracture aperture change b^{FF} is a negative number. Thus, it is confirmed that the precipitation of the mineral is more dominant than the free-face dissolution within the fractures under the PS condition. This is attributed to the sequential occurrence of precipitation within the fractures resulting from the supply of dissolved silica due to the pressure dissolution. A comparison of fracture aperture changes between pressure dissolution and free-face dissolution/precipitation shows that the quantity of fracture aperture change due to pressure dissolution increases to roughly one order of magnitude greater than that due to free-face dissolution/precipitation. When this difference in aperture change is converted to permeability, it becomes roughly two orders of magnitude greater. Consequently, the impact of pressure dissolution on the permeability change in rock fractures is more prominent than free-face dissolution/precipitation.

Although the permeability decreases with time in almost all the damaged zone due to the influence of the pressure dissolution, the permeability in the tensile damage zone changes little with time, as shown in **Fig. 6.19**. A comparison of **Figs. 6.14** and **6.17** indicates that under the PS condition, the domain where the permeability changes little within the damaged zone almost corresponds to the tensile damage zone. This is because the pressure dissolution induced by the compressive stress does not occur under the tensile stress condition. In particular, in the case of $K_0 = 1.5$, the tensile damage zone where permeability does not change is the most extensive. Thus, it is also important to understand the in-situ stress condition in order to precisely predict the evolution of rock permeability after disposing of radioactive waste. In addition, an increase in the contact-area ratio of the rock fractures due to the pressure dissolution at the fracture contacts may result in the recovery of the elastic modulus, while it is not considered in the current model. Therefore, when a tensile damage zone is generated near a shear damage zone, as with the results of the excavation analysis in the current work, the stress state within the tensile damage zone may change by the healing of the rock stiffness due to the pressure dissolution; and consequently, the pressure dissolution within the tensile fractures may resume. Further investigation of this phenomenon is required in future work.

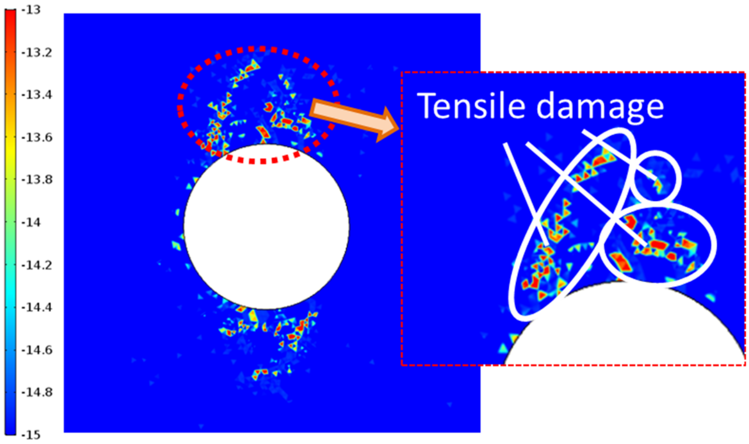

Fig. 6.19 Distribution of permeability in tensile damage zone.

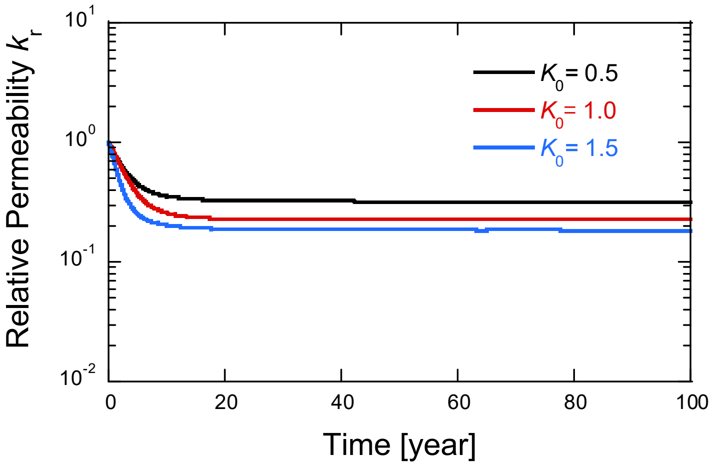

Fig. 6.20 Evolution of normalized mean permeability with different values for lateral pressure coefficient.

In order to more quantitatively evaluate the changes in permeability with time in the damaged zone ($D > 0$), due to the pressure dissolution, the evolution of the mean permeability was observed. The evolution of the normalized permeability given by the following equation, k_r, under the three initial ground pressure conditions ($K_0 = 0.5$, 1.0, and 1.5) is depicted in **Fig. 6.20**.

$$k_r = \frac{k_a(t)}{k_{a,i}}, \tag{6.40}$$

where $k_a(t)$ [m^2] is the mean permeability of the damaged zone at arbitrary time t, and $k_{a,i}$ [m^2] is the mean permeability of the damaged zone at the initial condition in this analysis. When the calculation domain and the total area of the damaged zone are set to be Ω and *S*, respectively, the mean permeability within the damaged zone is evaluated by the following functions that give 0 at the non-damaged zone:

$$k_f = \begin{cases} 0 & D = 0 \\ k & D > 0 \end{cases}, \tag{6.41}$$

$$\Psi_f = \begin{cases} 0 & D = 0 \\ 1 & D > 0 \end{cases}, \tag{6.42}$$

$$S = \int_{\Omega} \Psi_f (x, y) dxdy , \tag{6.43}$$

$$k_a = \int_{\Omega} k_f (x, y) dxdy / S . \tag{6.44}$$

As is apparent from **Fig. 6.20**, when a higher value of K_0 is applied, the rate of the permeability reduction becomes lower. This is because when a higher value of K_0 is applied, the compressive stress acting on the rock around the cavity becomes higher. However, the difference in the permeability reduction due to the influence of K_0 is relatively small - the changes in mean permeability of the damaged zone show that the mean permeability decreases by about one order of magnitude from the initial state (decreases to 20 % of the initial state at the maximum) and after that, it approaches the convergence value.

6.4 Summary

In this chapter, a coupled THMC model was developed that can describe the fracture evolution by incorporating the damage theory and the process of the mineral dissolution/precipitation (i.e., pressure dissolution and free-face dissolution/precipitation) within the generated fractures. The simulation of the uniaxial compression experiments on the granite specimen, using the developed model, can reproduce the behavior of the fracture initiation/propagation observed in the experiments. Subsequently, the long-term evolution of the permeability in the porous rock within the geological disposal system of high-level radioactive waste was predicted by the current model. The numerical analyses were conducted by varying the initial ground pressure condition ($K_0 = 0.5$, 1.0, and 1.5). The predictions for the excavation of the disposal cavity confirmed that the permeability within the damaged zone generated near the cavity during the excavation increased to about two orders magnitude greater than that of the intact rock zone. The range in generated fractures depended on the initial ground pressure condition and it was the most extensive under the condition of $K_0 = 1.5$. The long-term coupled analyses after the disposal of the radioactive waste showed that the permeability in almost all the damaged zones, induced by the shear mode, decreased to that of the intact rock zone due to the pressure dissolution at the contacting asperities within the fractures. However, the permeability in the tensile damage zone changed little from the initial state; and thus, it was obvious that understanding the in-situ stress condition is necessary for accurately predicting the changes in rock permeability with time.

This chapter focuses on the process of the fracture initiation/propagation and the long-term changes in permeability in the rock due to the mineral reactions. Therefore, the fracture initiation/propagation is considered only in the process of the cavity excavation. Consequently, the fracture initiation/propagation due to the time-dependent deformation and the alternation of the stress state, such as thermal stress and creep after disposing of the radioactive material, is not considered and the actual fracture distribution within the rock may not be predicted precisely. Thus, conducting numerical analyses that consider the time-dependent facture evolution is required. Moreover, the proposed model only considers the geochemical effect due to the mineral dissolution/precipitation for calculating the changes in rock permeability with time; and therefore, it is necessary to consider the mechanical effects, such as the collapse of the grains and the elastic deformation, in order to predict the changes in permeability more exactly. The proposed model assumes that the rock stiffness does not recover with time after the fracture initiation/propagation, but the healing of the rock stiffness may occur by the increase in the contact area within the fractures when the pressure dissolution is enhanced at the fracture contacts. Thus, updating the current model by taking into account not only the fracture initiation/propagation, but also the recovery of the rock stiffness caused by the mineral reactions is required. In addition, calculations were conducted by assuming that rock that is composed of only quartz; namely, our model, needs to be improved so that it can consider the mineral reactions in the multi-mineral compositions equivalent to the actual rock.

References

6.1) Aoyagi, K. and Ishii, E.: A method for Estimating the Highest Potential Hydraulic Conductivity in the Excavation Damaged Zone in Mudstone. Rock Mech. Rock Eng., 2019; 52: 385-401.

6.2) Zhang, C-H.: The stress-strain-permeability behaviour of clay rock during damage and recompaction. J. Rock Mech. Geotech. Eng., 2016; 8: 16-26.

6.3) Tsang, C-F., Jing, L., Stephansson, O. and Kautsky, F.: The DECOVALEX III project: A summary of activities and-lessons learned. Int. J. Rock Mech. Min. Sci., 2005; 42: 593-610.

6.4) Homand-Etienne, F. and Sebaibi, A.: Study of microcracking of the Lac du Bonnet granite. Eurock-ISRM Int. Symp., 1996; 2: 1353-1362.

6.5) Souley, M., Homand, F., Peda, S. and Hoxha, D.: Damaged-induced permeability changes in granite: a case example at the URL in Canada. Int. J. Rock Mech. Min. Sci., 2001; 38: 297-310.

6.6) Carlsson, SR. and Young, RP.: Acoustic emission and ultrasonic velocity study of excavated-induced microcrack damage at the underground research laboratory. Int. J. Rock Mech. Min. Sci., 1993; 30: 901-907.

6.7) Kelsall, PC., Case, JB. and Chabanne, CR.: Evaluation of excavation induced changes in permeability. Int. J. Rock Mech. Min. Sci., 1984; 21: 121-135.

6.8) Bauer, C., Homand, F. and Henry, JP.: In situ low permeability pulse test measurements. Int. J. Rock Mech. Min. Sci., 1995; 32: 357-63.

6.9) Polak, A., Elsworth, D., Yasuhara, H., Grader, A. and Halleck, P.: Permeability reduction of a natural fracture under net dissolution by hydrothermal fluids. Geophys. Res. Lett., 2003; 30(20): 2020, doi:10.1029/2003 GL017575.

6.10) Polak, A., Elsworth, D., Yasuhara, H., Grader, AS. and Halleck, PM.: Spontaneous switching of permeability changes in a limestone fracture with net dissolution. Water Resour. Res., 2004; 40, W03502, doi:10.1029/ 2003WR002717.

6.11) Yasuhara, H., Elsworth, D. and Polak, A.: Evolution of permeability in a natural fracture: the significant role of pressure solution. J. Geophys. Res., 2004; 109, B03204, doi:10.1029/2003JB002663.

6.12) Yasuhara, H., Kinoshita, N., Ohfuji, H., Lee, DS., Nakashima, S. and Kishida, K.: Temporal alteration of fracture permeability in granite under hydrothermal conditions and its interpretation by coupled chemo-mechanical model. Appl. Geochem., 2011; 26: 2074-2088.

6.13) Yasuhara, H. and Elsworth, D.: A numerical model simulating reactive transport and evolution of fracture permeability. Int. J. Numer. Anal. Methods Geomech., 2006; 30: 1039-1062.

6.14) Rutqvist, J., Wu, Y-S., Tsang, C-F. and Bodvasson, G.: A modeling approach for analysis of coupled multiphase fluid flow, heat transfer, and deformation in fractured porous rock. Int. J. Rock Mech. Min. Sci., 2002; 39: 429-442.

6.15) Suzuki, H., Nakama, S., Fujita, T., Imai, H. and Sazarshi, M.: A long-term THMC assessment on the geochemical behavior of the bentonite buffer. J. Nucl Fuel Cycle. Environ, 2012; 19: 39-50.

6.16) Nasir, O., Fall, M. and Evgin, E.: A simulator for modeling of porosity and permeability changes in near field sedimentary host rocks for nuclear waste under climate changes influences. Tunneling and Underground Space Technology, 2014; 42: 122-135.

6.17) Fall, M., Nasir, O. and Nguyen, T. S.: A coupled hydro-mechanical model for simulation of gas migration in host sedimentary rocks for waste repositories. Eng. Geol., 2014; 176: 24-44, 2014.

6.18) Zhang, R., Yin, X., Winterfeld, P. H. and Wu, Y.-S.: A fully coupled thermal-hydrological-chemical model for CO_2 geological sequestration. J. Nat. Gas Sci. Eng., 2016: 28: 280-304.

6.19) Danko, G. and Bahrami, D.: A new T-H-M-C model development for discrete-fracture EGS studies, Geothermal Resources Council Transactions. 2012; 36: 383-392.

6.20) Wei, CH., Zhu, WC. Chen, S. and Ranjith, PG.: A coupled thermal-hydrological-mechanical damage model and its numerical simulations of damage evolution in APSE. Materials, 2016; 9: 841, doi: 10.3390/ma9110841.

6.21) Li, LC., Tang, CA., Wang, SY. and Yu, J.: A coupled thermo-hydrologic-mechanical damage model and associated application in a stability analysis on a rock pillar. Tunneling and Underground Space Technology, 2013; 34: 38-53.

6.22) Wei, CH., Zhu, WC., Yu, QL., Xu, T. and Jeon, S.: Numerical simulation of excavation damaged zone under coupled thermal-mechanical conditions with varying mechanical parameters. Int. J. Rock Mech. Min. Sci., 2015; 75: 169-181.

6.23) Xu, T., Zhou, GL., Heap, J-M., Zhu, WC., Chen, CF. and Boud, P.: The influence of temperature on time-dependent deformation and failure in granite: a mesoscale modeling approach. Rock Mech. Rock Eng., 2017; doi: 10.1107/ s00603-0.17-1228-9.

6.24) Poulet, T., Karrech, A., Lieb, RK., Fisher, L. and Schaubs, P.: Thermal-hydraulic-mechanical-chemical coupling with damage mechanics using ESCRIPTRT and ABAQUAS. Tectonophysics, 2013: 124-132.

6.25) Marschall, P., Giger, S., Vassiere, DLR., Shao, H., Leung, H., Nussbaum, C., Trick, T., Lanyon, B., Senger, R., Lisjak, A. and Alcolea, A.: Hydro-mechanical evolution of the EDZ as transport path for radionuclides and gas: insights from the Mont Terri rock laboratory (Switzerland). Swiss J. Geosci., 2017; 110: 173-194.

6.26) Ogata, S.,Yasuhara, H. and Kishida, K. : Coupled THMC simulator incorporating pressure solution with dual porosity model and its application to long-term flow simulation of fractured rocks. Journal of the Society of Materials Science, 2018; 67: 310-317.

6.27) COMSOL2014：COMSOL MULTIPHYSICS. Version 5.0, Available from www.comsol.com.

6.28) Tang, CA.: Numerical simulation on progressive failure leading to collapse and associated seismicity. Int. J. Rock Mech. Min. Sci., 1997; 34: 249-262.

6.29) Tang, CA., Liu, H., Lee, KKP., Tsui, Y. and Tham, LG.: Numerical studies of the influence of microstructure on rock failure in uniaxial compression- Part I : effect of heterogeneity. Int. J. Rock Mech. Min. Sci., 2000; 37: 555-569.

6.30) Zhu, WC. and Tang, CA.: Micromechanical model for simulating the fracture process of rock. Rock Mech. Rock Eng., 2004; 37: 25-56.

6.31) Li, G. and Tang, CA.: A statistical meso-damage mechanical method for modeling trans-scale progressive failure process of rock. Int. J. Rock Mech. Min. Sci., 2015; 74: 133-150.

6.32) Liu, HY., Roquete, M., Kou, SQ. and Lindqvist, PA.: Characterization of rock heterogeneity and numerical verification. Eng. Geol., 2004; 72: 89-119.

6.33) Wang, SY., Sloan, SW., Scheng, DC., Yang, SQ. and Tang, CA.: Numerical study of failure behavior of pre-cracked rock specimens under conventional triaxial compression. Int. J. Solids Struct., 2014; 51: 1132-1148.

6.34) Lemaitre, J.: Evaluation of dissipation and damage in metals subjected to dynamic loading. Proceedings of the International Conference on Mechanical, 1971; 1: 15-20.

6.35) Zok, F. W.: On weakest link theory and Weibull statistics. J. Am. Ceram. Soc., 2017; 100: 1265-1268.

6.36) Zhu, WC., Weu, C., Li, S., Wei, J. and Zhang, M.: Numerical modeling on destress blasting in coal seam for enhancing gas drainage, Int. J. Rock Mech. Min. Sci., 2013; 59: 179-190.

6.37) Revil, A.: Pervasive pressure-solution transfer: a poro-visco-plastic model. Geophys. Res. Lett., 1999; 26: 255-258.

6.38) Ogata, S., Yasuhara, H., Kinoshita, N., Cheon, DS. and Kishida, K.: Modeling of coupled thermal-hydraulic-mechanical-chemical process for predicting the evolution in permeability and reactive transport behavior within single rock fractures., Int. J. Rock Mech. Min. Sci., 2018; 107: 271-281.

6.39) Cocks, A. and Ashby, M.: Intergranular fracture during power-law creep under multiaxial stresses. Metal Science, 1980; 14: 395-402.

6.40) Japan Nuclear Cycle Development Institute, 2000: Second Progress Report on Research and Development for the Geological Disposal of HLW in Japan, Supporting Report 2 Repository Design and Engineering Technology, H12: Project to Establish the Scientific and Technical Basis for HLW Disposal in Japan. JNC TN1410 2000-003, IV-139-IV-160.

Chapter 7

Conclusions and Future Studies

In this study, coupled THMC numerical models that can quantitatively predict the long-term evolution of the rock permeability at the actual field scale were newly developed. The models can describe the extremely complex interactions of the thermal, hydraulic, mechanical, and chemical processes potentially occurring within the rock near the radioactive waste in geological disposal systems. In particular, being able to describe the changes in rock permeability with time due to the geochemical effects by incorporating the mineral dissolution/precipitation, such as pressure dissolution, into the THMC coupled processes is a remarkable characteristic of these models. Additionally, the long-term evolution of the permeability of the rock that works as a natural barrier was predicted using the developed models, and scenarios related to the performance of the natural barrier during the period of geological disposal were proposed. The conclusions obtained from each chapter are described below.

In **Chapter 3**, a coupled THMC numerical model, incorporating the pressure dissolution at the grain contacts, was developed to investigate the long-term evolution of the permeability in porous rock. The model can describe the changes in porosity/permeability due to the mineral reactions within the matrix of the porous rock. It should be noted that one achievement of this work was the ability to fit the chemo-mechanical conceptual model of the pressure dissolution at the grain contacts into the coupled numerical model and to conduct numerical simulations at the field scale instead of at the representative element scale. In order to validate the proposed model, model predictions were compared with laboratory experiments[7.1)]. In the experiments, the compaction of quartz sand was conducted under the constant effective stresses of 69.0, 34.5, and 17.2 MPa at 150°C and the evolution of the porosity and the silica concentration in the pore water over time were measured in order to examine the influences related to the pressure dissolution at the grain contacts. The decrease in porosity and the evolution of the silica concentration in the pore water were predicted. All the simulated decreases in porosity with time were sufficiently congruent with the experimental measurements. The predicted silica concentrations followed the tendency observed in the experiments well. Thus, a comparison of the results between the simulations and the experimental measurements indicted that the model developed here is valid for predicting the long-term porosity/permeability changes in porous media induced by pressure dissolution and free-face dissolution/precipitation. Subsequently, the validated model was applied to investigate the influence of the pressure dissolution on the evolution of the permeability in the porous rock near radioactive materials within a geological disposal system under the expected subsurface conditions. The predicted results showed that the permeability especially close to the excavated cavity decreased to one order of magnitude smaller than the initial state in 10^4 years due to the influence of the pressure dissolution at the grain contacts within the matrix of the porous rock.

In **Chapter 4**, a multi-physics numerical model was developed to predict the evolution of permeability and the reactive transport behavior in rock fractures in the field scale under coupled THMC conditions. In particular, the model was employed for the purpose of describing the evolution of permeability and the reactive transport behavior within rock fractures by taking into account the mineral reactions of free-face dissolution and pressure dissolution. In order to examine the capability of the developed model, the model was applied to replicate the experimental measurements of the evolution of hydraulic aperture, permeability, and element concentrations obtained from flow-through experiments using single granite and mudstone fractures7.2). The model predictions for the granite experiments were able to follow the actual data for the evolution of the hydraulic aperture and the effluent element concentrations without adopting any fitting parameters, which is often a necessary step in other simulations using coupled THMC models, as shown in the literature. Furthermore, the model was successful in replicating the actual changes in fracture permeability and effluent element concentrations within the mudstone fractures. Although mismatches between the experiments and the model predictions, such as changes in the concentrations of several elements (i.e., Na and K concentrations in the granite fracture and Al in the mudstone fracture) still remain at this stage, the developed model should be valid for evaluating the evolution of permeability and the mass transport behavior within rock fractures induced by mineral reactions under stress- and temperature-controlled conditions.

In **Chapter 5**, a coupled THMC numerical model was developed that can evaluate the changes in rock permeability within both matrix and fracture domains incorporating pressure dissolution within both the grain contacts and the fracture contacts. This model can calculate the fully coupled THMC processes incorporating the two-way interactions between the H (hydraulic) and M (mechanical) components, and the T (thermal) and M (mechanical) components, which are not considered in the model7.3) introduced in **Chapter 3**. Evaluating the permeability evolution within not only the rock matrix, but also the rock fractures, due to the mineral reactions is the remarkable originality of the proposed model. In the developed model, the mineral reactions within the rock matrix and the rock fractures were described by incorporating the dual porosity theory and formulations of the processes of the pressure dissolution proposed in **Chapter 3** and **Chapter 4**. The proposed model was applied to predict the long-term evolution of the permeability in fractured rock near radioactive waste and the influence of the pressure dissolution on the permeability change was closely examined. In order to separately investigate the impacts of the pressure dissolution within the rock fractures and the rock matrix, a comparison was conducted of the changes in permeability between the No-PS condition (not including pressure dissolution) and the PS conditions - PS (Matrix & Fractures) including pressure dissolution within both fractures and matrix and PS (Only Matrix) including only the pressure dissolution within the matrix. The predicted results showed that the rock permeability of the EDZ eventually decreased to that of the intact rock due to the pressure dissolution at the contacting asperities within the rock fractures. Moreover, predictions were conducted by varying the parameters of a that should control the relation between the fracture aperture and the contact-area ratio. The predictions confirmed that parameter a has a great impact on the decrease in permeability in fractured rock and that the setting of the parameter is important to being able to precisely evaluate the changes in permeability. Overall, it can be concluded that the pressure dissolution within the rock fractures should have a significant influence on the evolution of the rock permeability of dual porosity media in the EDZ.

In **Chapter 6,** a coupled THMC model was developed, including fracture initiation/propagation, by incorporating the damage theory and the process of mineral dissolution/precipitation (i.e., pressure dissolution and free-face dissolution/precipitation) within the generated fractures. With this model, the damage evolution (fracture initiation/propagation) and the changes in the thermal, hydraulic, mechanical, and chemical properties of the rock due to the damage can be calculated. In particular, the ability to describe the mineral reactions within the rock fractures predicted by the damage theory and the subsequent permeability changes is the important originality of the model. The numerical simulations for the uniaxial compression experiments on the granite specimen were able to follow the fracture evolution observed in the experiments and the validity of the developed model was confirmed. Subsequently, the proposed model was applied to predictions of the long-term permeability changes in the rock near high-level radioactive waste. The numerical simulations were performed under three initial ground pressure conditions (lateral pressure coefficient K_0 = 0.5, 1.0, and 1.5). The predicted results for the excavation of a disposal cavity revealed that several fractures were generated near the disposal cavity and that the permeability of the damaged zone increased to about two orders of magnitude greater than that of the intact rock during the excavation. The initial ground pressure condition affects the fracture evolution and fractures were generated within the most extensive range under the condition of K_0 = 1.5. Long-term coupled THMC simulations during the first 10^2 years after disposing the radioactive waste indicated that the permeability in almost the entire damaged zone generated by shear failure decreased to that of the intact rock due to the pressure dissolution at the contacting asperities within the rock fractures. However, the permeability within the tensile damage zone changed little from the initial state; and therefore, it was apparent that evaluating the in-situ stress condition is required in order to precisely examine the evolution of rock permeability. Overall, it was obvious that the proposed model can predict the processes from the fracture formation to the fracture sealing within the rocks at the actual field scale; and thus, it should provide confidence for using the proposed model to examine the long-term performance of natural barriers for delaying the transport of radionuclides.

Finally, recommendations for future studies are described below.

In this study, long-term coupled simulations were performed by assuming that the rock was composed only of quartz. Therefore, long-term THMC calculations describing the mineral reactions for multi-mineral compositions, equivalent to the actual rock, should be conducted at the field scale.

Additionally, the influence of the fractures that existed in the original state before the cavity excavation was not considered in this study. Thus, updating the model by explicitly incorporating the pre-existing fracture network is necessary for describing the complex behavior of the fluid flow within actual rock more precisely.

For the coupled THMC numerical model explained in **Chapter 6**, focus was placed on the process of fracture initiation/propagation and the long-term permeability changes in the rock due to the mineral reactions. The fracture initiation/propagation was assumed only in the process of the cavity excavation. In other words, the time-dependent fracture initiation/propagation due to changes in the stress distribution, such as thermal stress and creep after disposing the radioactive waste, was not considered. Thus, performing numerical simulations that incorporate the time-dependent fracture evolution is required.

The proposed model in **Chapter 6** assumed that the rock stiffness does not change with time after the fracture initiation/propagation, but increases in the contact area of the fractures due to pressure dissolution at the fracture contacts and may result in the recovery of the rock stiffness. Therefore, updating the current model by considering not only the fracture evolution, but also the increase in rock stiffness caused by the mineral reactions is necessary.

Moreover, most of the proposed models in this study only considered the geochemical effect due to mineral dissolution/precipitation for calculating the changes in rock permeability with time. Thus, it will be required in future studies to consider the mechanical effects, such as the collapse of the grains and viscoplastic deformation, in order to evaluate the changes in permeability more accurately.

References

7.1) Elias, BP. and Hajash, A.: Change in quartz solubility and porosity change due to effective stress: An experimental investigation of pressure solution. Geology, 1992; 20:451-54.

7.2) Yasuhara, H., Kinoshita, N., Ohfuji, H., Lee, DS., Nakashima, S. and Kishida, K.: Temporal alteration of fracture permeability in granite under hydrothermal conditions and its interpretation by coupled chemo-mechanical model. Appl. Geochem., 2011; 26:2074-88.

7.3) Yasuhara, H., Kinoshita, N., Ogata, S., Cheon, DS. and Kishida, K.: Coupled thermal-hydro-mechanical-chemical modeling by incorporating pressure solution for estimating the evolution of rock permeability. Int. J. Rock Mech. Min. Sci., 2016; 86: 104-114.